KU LEUVEN

FACULTEIT INDUSTRIËLE
INGENIEURSWETENSCHAPPEN

CAMPUS DE NAYER SINT-KATELIJNE-WAVER

Extrusion printing of a hydrogel material for bone tissue engineering

Ikram Mohout

Promotor: Prof. dr. E. Ferraris

Co-promotor: Prof. dr. V. Bloemen

Masterproef ingediend tot het behalen van de
graad van Master of Science in de industriële
wetenschappen: *elektromechanica,*
manufacturing engineering

Academiejaar 2017-2018

Preface

A Master’s thesis is the last fundamental chapter before graduating. I am grateful for being able to explore the field of tissue engineering, as it is an exciting domain and slightly out of the ordinary for the average manufacturing engineering student. I would like to thank several people who have helped me during the course of my thesis.

First of all, I would like to thank my promotor Prof. E. Ferraris and co-promotor Prof V. Bloemen for the continuous guidance and feedback. I would also like to thank my supervisor Rory Gibney for the guidance and clarifying different aspects of the tissue engineering field, which helped to overcome my lack of background knowledge of the domain.

A special thanks to Paulo Alexandre Amorim for carrying out the rheological experiments and for providing me more insight in the basic rheology concepts. Furthermore I would like to thank Danny Winant for carrying out the DSC tests, Julien Debontridder for examining the hydroxyapatite samples with the SEM, Ing. Chris Peeters for his help and advice with regarding to the SEM and the Hirox KH-8700 microscope and Dr. Ing. M. Faes for introducing me to the basics of the thermal camera. I would also like to thank Prof. D. Pauwels for helping me with the electrical scheme of the cooling plate and providing feedback when needed.

Last but not least, I would like to thank my family, friends and loved ones for showing me continuous support along the way. Additionally I would like to thank the student-colleagues who worked alongside me in the additive manufacturing lab for always helping out when a problem occurred and creating an pleasant working atmosphere.

Samenvatting

Jaarlijks vinden er wereldwijd meer dan 2.2 miljoen bottransplantaties plaats. Ondanks de aanzienlijke vraag zijn er heel wat complicaties die bij dergelijke ingreep komen kijken, zoals infecties, niet uniforme hechtingen en nog talrijke andere complicaties. *Bone tissue engineering* probeert hierop in te spelen en tracht bijkomend een antwoord te geven aan het tekort aan donorweefsels. In essentie is *bone tissue engineering* een combinatie van hoofdzakelijk cellen die zich in een omgeving bevinden, vaak biomaterialen, dat potentieel heeft om botregeneratie te stimuleren. De focus binnen het domein ligt op additieve technieken om zulke constructies te kunnen 3D printen, meer specifiek extrusie gebaseerde technieken. De printer die gebruikt wordt voor de testen in deze thesis is de *Inkredible+ Bioprinter*, een extrusie gebaseerde bioprinter die pneumatisch te werk gaat.

Gekoppeld aan het printen van constructies zijn een aantal randvoorwaarden. In eerste instantie moet de cel omgeving biocompatibel zijn en eveneens de levensvatbaarheid en de groei van cellen stimuleren. Een tweede belangrijke vereiste is een zekere mechanische stijfheid en sterkte van de constructie voornamelijk omdat het om botregeneratie gaat. Vaak is er een tweestrijd tussen wat gunstig is voor het een ongunstig is voor het ander. De grootste uitdaging is om een balans te zoeken tussen deze twee factoren. De belangrijkst factoren die een invloed hebben op de mechanische en biologische eigenschappen van een constructie, in het geval van additieve technieken, zijn de print parameters en de materiaaleigenschappen van het biomateriaal. Deze vaststelling ligt aan de basis van de opbouw van de thesis.

Op vlak van biomaterialen ligt de focus uitsluitend op het gebruik van hydrogels. Dit zijn gehydrateerde driedimensionale netwerken van gecrosslinkte polymeren die een ideale omgeving blijken te zijn voor cellen. In eerste instantie zal er afgetast worden welke hydrogels er beschikbaar zijn en welke in aanmerkingen komen. Vervolgens wordt er een studie uitgevoerd naar de eigenschappen van de materialen, de klemtoon ligt hier vooral op de reologische eigenschappen. Op basis van deze resultaten wordt er inzicht verkregen in hoe het materiaal zich gedraagt.

Het biomateriaal dient verder gecrosslinkt te worden om stabiliteit te introduceren. In dit geval wordt er geopteerd om thermisch te crosslinken, door een temperatuurverschil te induceren tussen de spuitkop en het printplatform. Op deze manier kan er tijdens het printproces zelf gecrosslinkt worden. Echter is deze vorm van crosslinken reversibel en zwak, het is dan ook een eerste stap die genomen wordt naar het crosslinken van dergelijke materialen. Helaas beschikt de *Inkredible+* niet over een koelplatform. Een van de doelen van deze thesis is dan ook heb ontwerpen en ontwikkelen van een koelsysteem dat tot 10 °C kan koelen ten opzichte van de kamertemperatuur (21 °C). Er wordt niet onder de 10°C gekoeld vermits lage temperaturen niet de ideale cel omgeving zijn.

In de laatste fase van de thesis wordt er op zoek gegaan naar de ideale parameters voor het printen met de gekozen hydrogels. Hier komt het voorgaande werk samen, de kennis van de materiaal eigenschappen en de analyse van de bioprinter vormt een sterke basis in deze fase. De parameters waarop er gefocust wordt zijn de printsnelheid, de druk en de diameter van de printkop. Er worden zowel conische als naaldvormige printkoppen geïmplementeerd.

Het zoeken van de print parameters gebeurt in eerste instantie via een trial en error methode. De nadruk wordt gelegd op het consistent zijn van de geprinte banen en bij uitbreiding wordt er gezocht naar een zo fijn mogelijk bandbreedte zonder toe te geven aan inconsistenties, de beoordeling gebeurt visueel. Eens gunstige parameters gevonden zijn wordt een *design of experiments* uitgevoerd. De validatie van de respons, de baanbreedte, gebeurt microscopisch. De significante parameters worden uit de ANOVA analyse gehaald en een vergelijking wordt opgesteld om de response te beschrijven aan de hand van de input van de *design of experiments*. Indien het proces onder controle is worden er rasterstructuren geprint, hier ligt de focus op de afstand tussen de geprinte banen. Er wordt onderzocht hoe diffusie evolueert met de afstand tussen de banen. Als laatste stap wordt er een 3D structuur geprint waar er gezocht wordt naar een toepasselijk *layer height* zodat er hechting tussen de verschillende lagen plaats kan vinden.

Abstract

Bone is one of the most transplanted tissue worldwide with more than 2.2 million bone grafts taking place each year. Despite this high demand there are still a lot of complications in the field, such as infections, no uniform union, shortage of donor material. Bone tissue engineering can be viewed as an answer to these problems. In essence engineered tissue is a combination of cells, scaffold materials and possibly some other growth factors. This thesis focusses on taking the first minor steps towards printing a construct that is capable of enhancing bone regeneration.

In this thesis the focus lies on additive manufacturing techniques, mainly extrusion printing. Extrusion printing is favorable because it is able to work with materials with a wide variety of viscosity and is able to print structures with a significant high cell density (up to the point of cell spheroids). The bioprinter being used is the *Inkredible*+ from the *Cellink* company, this is a pneumatically operated extrusion bioprinter.

The scaffold material, often a biomaterial, has a number of specific requirements. The biomaterial, in this case a hydrogel, has to provide an ideal environment that promotes cell viability and attachment and growth. On the other hand the printing fidelity is of importance. In the light of bone tissue engineering the construct is required to have a certain degree of stiffness. It is a challenge to find the balance between creating an ideal environment for the cells and providing mechanical stability. The mechanical and physiological aspects are mainly tuned by the bioink properties in combination with the printing parameters. Unfortunately conflict between the parameters that have a positive effect on the fidelity and the parameters that have a positive effect on cell viability.

In this thesis the hydrogel of choice is gelatin. Further *Cellink start* material is used, one of the company's own ink, this serves as a reference material as it has suitable printing properties. The hydrogels properties are examined through a series of conducted experiments, the highlight of the results are the examined rheological properties.

To create instant stability during the printing process, thermal crosslinking is applied by inducing a temperature difference between the syringe and the printbed. As the bioprinter does not include cooling of the bed, such bed is manufactured. The aim is to cool a controlled cooling system that is able to cool down to about 10°C at room temperature (21 °C). Low temperatures in general are not ideal for the cell viability, this is why such threshold is applied.

The last phase of this thesis is the experimental phase, the focus lies on finding suitable parameters for the printing process for *Cellink start* and gelatin. The main parameters that are examined are the printing pressure, the feed rate and the nozzle inner diameter. Conical nozzles as well as blunt nozzles are implemented. The first approach is a trial and error approach, based on visual examination printed tracks are evaluated by their consistency. The idea is to work towards a fine print (small track width) without losing the consistency of the printed track. Once a range of suitable parameters is found a full factorial design of experiments is conducted. The results from the ANOVA, if the printing process is under control, show the parameters that have a significant effect on the response, i.e. the track width measured microscopically. Furthermore a regression equation is presented based on the inputs from the design of experiments, where the relationship is mathematically presented between the input variables and the response. If the process is under control, a lattice pattern is printed with chosen suitable parameters. Here the infill is of importance, this is the factor that is sets the distance between lines. Different percentages of infill are examined and the diffusion rate is calculated to gain understanding on how diffusion is influenced by the distance between tracks. The final stage is printing of a 3D structure, the main challenge here is to unravel a suitable layer height to ensure there is bonding between layers, this is done with trial and error.

Key words: bone tissue engineering, hydrogels, gelatin, additive manufacturing, extrusion bioprinting, printing fidelity, cell viability, thermal crosslinking, printing parameters

Table of contents

List of Symbols

A_e	Experimental capacity	[mm^2]
A_{th}	Theoretical area cavity lattice structure	[mm^2]
C	Capacitance	[F]
COP	Coefficient of performance	[%]
f_c	Cutoff frequency	[Hz]
G'	Shear storage modulus	[Pa]
G''	Shear loss modulus	[Pa]
G^*	Complex shear modulus	[Pa]
I	Current	[A]
i	Imaginary unit	[/]
K	Power law constant	[$Pa.s^n$]
n	Exponential power law constant	[/]
P	Electrical power	[W]
Q_c	Cooling power	[W]
Q_h	Total dissipated power	[W]
R	Electrical resistance	[Ω]
R_{Th}	Thermal resistance	[$°C.W^{-1}$]
U	Voltage	[V]
γ	Shear strain	[/]
$\dot{\gamma}$	Shear rate	[s^{-1}]
ΔT_{HS}	Temperature difference between heatsink and environment	[°C]
δ	Phase angle	[°]
η	Dynamic viscosity	[Pa.s]
η^*	Complex viscosity	[Pa.s]
τ	Shear stress	[Pa]
φ	Diffusion rate	[%]
ω	Angular velocity	[$rad.s^{-1}$]

Abbreviations

AM	Additive Manufacturing
AMF	Additive manufacturing file format
ANOVA	Analyses of variance
BPM	Bitmap
BTE	Bone Tissue Engineering
CAD	Computer Aided Design
COP	Coefficient of performance
CT	Computed Tomography
DOE	Design of experiments
DSC	Differential Scanning Calorimetry
ECM	Extracellular Matrix
EDS	energy-dispersive X-ray spectroscopy
FOV	Field Of View
FS	Factor Sensitivity
GelMa	Gelatin Methacrylamide
HA	Hydroxyapatite
JPEG	Joint Photographic Experts Group
LA	Laser assisted
LCD	Liquid crystal display
LVE	linear viscoelastic range
MA	Methacrylate
MRI	Magnetic Resonance Imaging
MSC	Mesenchymal Stem Cells
OBT	Object file
PEGDA	Polyethylene glycol diacrylate
PEGMA	Polyethylene methacrylate
PID	proportional integral derivative
PLGA	Polylactic-co-glycolic acid
PWM	Pulse With Modulation
RGD	Arginine-glycine-aspartic acid

RPM	rates per minute
SAOS	small amplitude oscillatory shear
SEM	Scanning electron microscope
SLA	Stereolithography
STL	Stereolithography
TE	tissue engineering
UV	Ultraviolet

Table of Figures

Table of tables

1 INTRODUCTION

Hydrogel materials are extrusion printed pneumatically for bone tissue engineering. **This project is taking the first steps towards 3D printing of a construct that has the potential of enhancing bone regeneration.**

A **maximum of three different materials** are used. The base material is a hydrogel, optional as a mixture with other biomaterials. The printed material is **crosslinked**. The first objective is to determine suitable biomaterial and crosslinking methods. This also includes a **properties study** of the chosen material through **a series of conducted experiments**.

In order to 3D print and crosslink the selected materials as desired, adjustments can be made to the printing process. Therefore the second objective is to **improve the post-process crosslinking** by making technical adjustments to the 3D printer. The third objective is to find the **optimal printing parameters**. The last important objective is validation. The outcome of the printing process will be **evaluated in term of printability**. The outcome of these validations will be expressed in terms of dimensional accuracy, microscopically and visually.

The duration of the project is one academic year, consisting of two semesters. The focus of the first semester lies on literature study and the properties of the printing material. The second semester will have a more experimental approach, concentrating on the extrusion printing itself. The hydrogels used are fabricated in a standard chemistry lab, however attention should be paid to the safety regulations of the used materials.

2 LITERATURE STUDY

2.1 Bone regeneration

2.1.1 Bone repair by means of grafts

Bone is one of the most transplanted tissue with more than 2.2 million bone grafts taking place each year worldwide. Bone injuries or defects could be (among other things) a consequence of an infection, aging, trauma or neoplasm (an abnormal growth of tissue). [1]

There are four traditional ways bone grafting is practiced. Allogenous (using tissue from the same species), Autogenous (using tissue from the organism itself), Xenogenous (using tissue from a different species) and prosthetic grafting. A distinction can be made between cancellous and cortical grafts. The first one is mainly used to fill small defects, whereas the second is mostly used as supportive rods. Autogenous cancellous bone is favorable for its osteogenic potential (viable progenitor cells are present within the tissue), absence of immunologic rejection and no disease can be further transmitted. On the other hand acquiring autogenous bone tissue can be quite a challenge knowing that harvesting such tissue could cause infections and blood loss. In addition, the tissue supply is scarce as it is taken from the rib, fibula, tibia or iliac crest. This last problem can be overcome by allogenous bone, but this tissue can be immunologic rejected and there is no osteogenic potential. For additional background information on bone structure and physiology, appendix A.1 can be consulted. [2], [3]

2.1.2 Clinical needs for tissue engineering

To the present day allo- , xeno- and prosthetic-grafts are used for bone repair. Nevertheless there are possible complications such as infections, limited tissue supplies, non-union and fatigue failures, foreign tissue might be rejected or another surgery is necessary. As mentioned before, one way to overcome immunologic rejection is using autografts, furthermore osteoconduction (bone growth on a surface), osteoinduction and osteogenesis can be attained. Yet this strategy does have its limitations and 10-30% experience complications. Furthermore another downside is the cost and requirement of material, in the case of autogenous material this means another surgical procedure to obtain the bone tissue, the weakening of the donor bone areas and the possibility of additional complications during the process. Prosthetic-grafts seem to offer a solution to these last set of problems, however, knowing that incorporation of the material into the skeleton is not possible, wear and tear can take the upper hand.[1], [3], [4]

Bone tissue engineering (BTE) is a promising approach to overcome the complications and limitations discussed in previous paragraphs. Findings indicate that tissue engineering is a method capable to stimulate bone repair, shorten healing time, decrease the amount of pain and complications and the need for additional surgery becomes unnecessary. Moreover the scaffolds used in tissue engineering are in general biodegradable allowing more space for new forming bone tissue, the scaffold also supports viability by creating a cell environment that mimics its natural milieu.[2]

2.2 Bone tissue engineering

2.2.1 **Introduction to bone tissue engineering [5] [6]**

It is clear that BTE can be viewed as an answer to complications experienced in the bone regeneration field and has numerous advantages. This evolving domain has to offer a lot of potential and has gained a huge amount of popularity.

In essence engineered tissue is a composition of scaffold material, cells and possibly other growth/soluble factors. The scaffold provides support for 3D tissue formation. In combination with the carefully chosen material it mimics the ECM of the bone to provide the ideal environment for the present cells and stimulate the bone growth. BTE commences *ex vivo* and works towards *in vivo* applications in the long term.

Because BTE has to meet a series of requirements (such as maintaining/improving cell viability, vascularization, host integration and osteogenic potential), it is necessary to control the factors that influence the characteristics of the engineered bone tissue. They can be categorized into structural and biological factors, composition of the biomaterial and fabrication process. This introduction chapter emphasizes the fabrication process. There are two major categories, conventional techniques and additive manufacturing (AM) techniques.

Conventional techniques are the first techniques to emerge in the tissue engineering field. In general they are based on subtractive methods that aim to generate highly porous solids. Widespread techniques are among others freeze-drying, powder-forming, gas foaming/solvent casting particle leaching techniques, sol-gel, electrospinning. A disadvantage of these type of methods is the poor control over the shape and geometries of the construct. Moreover it can be challenging to implement the desired pore size and attain a consequent pore shape. Additionally the cell viability might be effected by the use of organic solvents implemented in multiple of the mentioned techniques. AM techniques try to eliminate these limitations. The concept of this process is to create a 3D construct/structure through deposition of layers. AM technology allows better control of porosity as well as mechanical and chemical properties, it augments biocompatibility, avoids toxic material and has a possibilities to implementing multiple cell types. There is no need to implement abrasive techniques and can undermine the amount of waste that subtractive methods might require.

However there are other reasons for tissue engineering to evolve towards AM applications. Commercialization is a major factor in the industry. With AM techniques mass customization is possible. The fabrication of the engineered tissue can be based on computed tomography (CT) scans and processed with computer aided design. In combination with the ability to reach a certain complexity regarding the geometry and a high throughput, this is a very interesting approach for commercializing. These factors also play an important role on the perspective of patience and doctors and their expectations of tissue engineering (TE).

For these reasons the focus of this study will be AM based. However there are different strategies within the AM approach, each with specific advantages and disadvantages.

2.2.2 Strategies for AM tissue engineering

In general there are two strategies to embody living cells into an additive manufactured scaffold. The first being *Cell seeding post-printing (post-seeding)*, this strategy puts emphasis on the fabrication of a scaffold and does so by printing cell-free material. Only after posttreatment will the scaffold be seeded with cells. The second approach is *3D bioprinting*. Here a mixture of scaffold material (often hydrogels) and cells, called bioink, are printed.

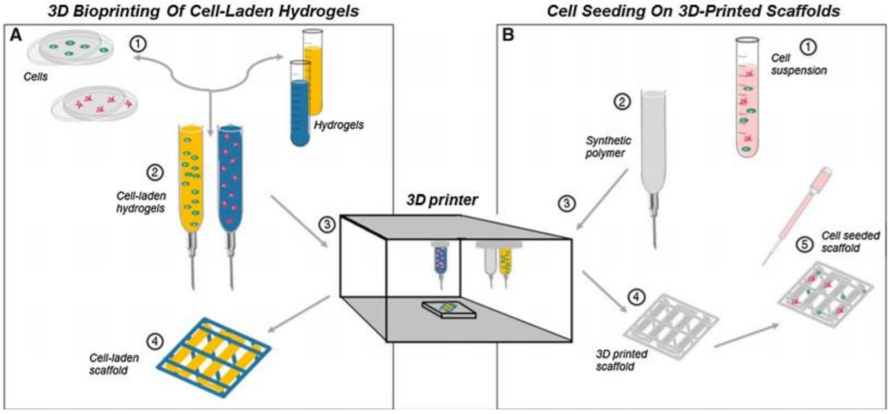

Figure 2.2-1 Strategies for AM tissue engineering. Left, bioprinting, right, cell seeding on scaffolds [1]

Both strategies have their own advantages and limitations. For instance, bioprinting allows more than one cell type to be used at once because of the incorporation of cells in the printed material, the cell density and distribution can be controlled and a high seeding density, compared to post-seeding, is possible. Cell migration is harder to induce in the case of post-seeding, it must rely on alternatives such as surface modification. On the other hand cell seeding on scaffolds has a higher accuracy regarding the global shape of the scaffold and pore size. Furthermore the compressive modulus has a range between 4 MPa and 77.2 MPa, thus providing a mechanical strength that is in the range of cancellous bone (4 MPa is acquired with direct writing preosteoblast cells in gelatin/hydroxyapatite and the 77.2 MPa is required with 3D plotting human fetal osteoblast cells in PLGA.). Bioprinting has a compressive modulus in the range of kPa (As tested with inkjet printing and bioplotting MSCs in -among other options- PEGMA, gelatin, GelMA, alginate), yet over time, due to differentiation and mineralization of the extracellular matrix (ECM), the cells may increase the modulus up to 100%. [1]

Bioprinting is the focus of this thesis and is discussed in more details to emphasize the whole process of bioprinting and how different techniques have a slightly different approach at implementing this strategy.

2.3 3D Bioprinting

2.3.1 Bioprinting process

The bigger picture of the bioprinting process can be divided into three main parts being: pre-processing, processing and post-processing.

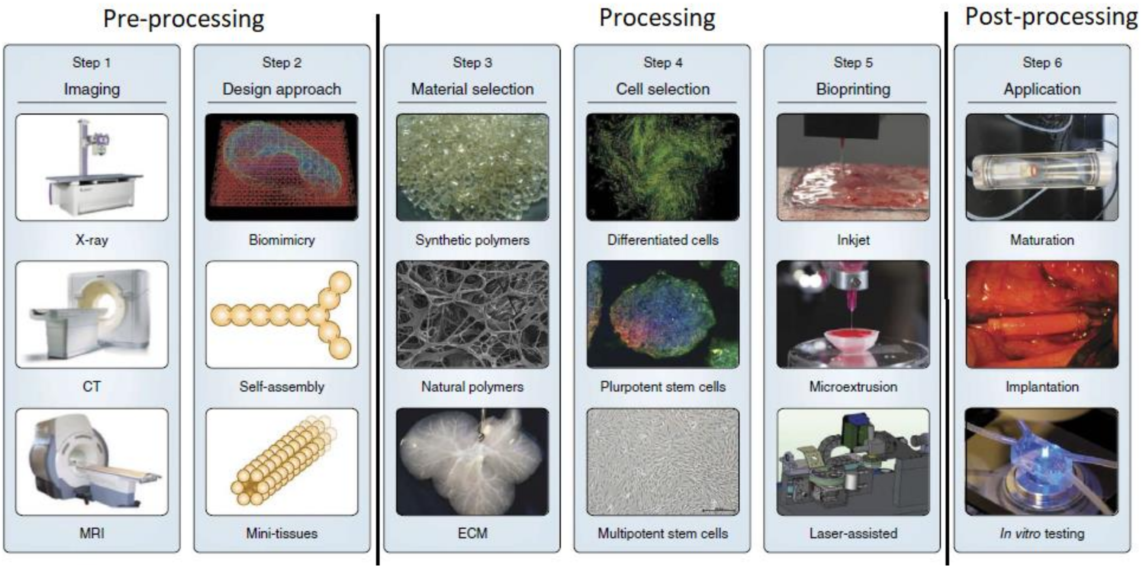

Figure 2.3-1 Step by step representation of the three phases of a bioprinting process, pre-processing, processing and post processing [7]

2.3.1.1 *Pre-processing*

The pre-processing phase allows insight in the composition and architecture of the involved tissue. Through medical imaging technology information about 3D structure and function at cellular up to organism level can be provided. The most common forms are computed tomography (CT) and magnetic resonance imaging (MRI). CT is based on X-rays which penetrate the tissue, by measuring the intensity and angle of the transmitted rays a (small) volume of tissue can be pixelated with high spatial resolution. MRI functions through a strong magnetic fields exerted onto the body. The magnetic vector is deflected by adding energy coming from radio waves. By removing (the source of) the radio waves the magnetic vectors fall back into their rest position, producing a signal which is used to create the desired image. The technique is able to provide the same information as CT, in addition MRI has a higher contrast resolution which is interesting for soft tissue. [4], [7], [8]

To collect and digitize the information (provided by CT and MRI scans) computer-aided design and computer-aided manufacturing CAD-CAM tools are used. In addition these tools can predict properties of the printed structure and improve the design. They are necessary throughout all of the three phases. A bio-CAD system can create a 3D anatomic presentation for any extra modification or analysis, to create the desired tissue models. A bio-CAM system can then focus on the fabrication process and predict the feasibility. Furthermore the parameters for the printing process should also be determined in this stage. [4], [7]

2.3.1.2 Processing

As soon as the printing process is determined, an appropriate bioink is chosen, this step is crucial and will be discussed in chapter 2.4. Once the parameters chosen during pre-processing are set, printing can commence. [4]

2.3.1.3 Post-processing

Before implanting bioprinted tissue, in case of *in vivo*, the tissue should be allowed to mature. A bioreactor mimics the *in vivo* environment suited for the specific tissue through parameters such as pH, temperature, gas and nutrition concentration and possibly mechanical stimulation. The reactor also maintains the viability and provides more time for tissue fusion in the postprocessing phase. A challenge that still remains is the search of suitable coating materials for the reactor, so there is no harm brought to the tissue. [4], [7]

2.3.2 Bioprinting techniques

As discussed previously, in the pre-processing phase, a printing process is selected. There are four major bioprinting techniques: Inkjet, laser-assisted (LA), stereolithography (SLA) and extrusion. [9] Each has their own physical process resulting in certain advantages and disadvantages. There is no one superior bioprinting technique, different parameters must be taken into consideration when choosing a specific technique. Table 2.3-1 shows a comparison of the four techniques presented by *Mandrycky e.a (2016)*. [10]

Table 2.3-1 Comparison of the four major printing techniques [10]

Parameters	Inkjet	Laser-assisted	Extrusion	Stereolithography
Cost	Low	high	moderate	low
Cell viability	> 85%	> 95%	40%–80%	> 85%
Print speed	Fast	Medium	Slow	Fast
Supported viscosities	3.5 to 12 mPa/s	1 to 300 mPa/s	30 mPa/s to above 6×10^7 mPa/s	No limitation
Resolution	High	High	Moderate	High
Quality of vertical structure	Poor	Fair	Good	Good
Cell density	Low < 10^6 cells/mL	Medium < 10^8 cells/mL	High (cell spheroids)	Medium < 10^8 cells/mL
Representative materials for bioinks	Alginate, PEGDMA, Collagen	Collagen, Matrigel	Alginate, GelMA, Collagen	GelMA, GelMA-PEGDA hybrid hydrogel

Bioprinting deposits living cells (with or without bioink) in a layer-by-layer fashion that allows the spatial positioning (of the cells) to be determined by the user. The specific technique implemented in this study to practice bioprinting is extrusion based. For more information regarding the other techniques appendix A.2 can be consulted. [11]

2.3.2.1 (Micro-) Extrusion bioprinting [11], [12]

This bioprinting technique will be the main focus of this study as it is also the most common and affordable. It can be considered a modified version of inkjet printing, however extrusion printing is able to process materials with a high viscosity (above 6×10^7 mPa/s). The process is either pneumatic, mechanic or solenoid-based and extrudes a cell-laden hydrogel filament through a micronozzle or needle. A pneumatic printing process can be based on a valve-free or valve system, the first being a basic and simple system, yet the second provides a higher accuracy through a controlled frequency of the pressure. 2D patterns are created with the solidified hydrogel and 3D structures are created by stacking 2D layers on top of each other.

This technique provides the freedom to apply multiple cells and material, through ink-cartridges that are connected to a nozzle. Bioinks with high viscosity as well as high cell density can be printed with a good quality of the vertical structure. Additionally extrusion based bioprinting is capable of printing an anatomically conformed porous construct. The downside of extrusion printing is that the resolution is lower (> 100 µm) compared to the alternatives. Another disadvantage is that the bioink is required to have a shear thinning property (this is discussed in chapter 2.6.1), to avoid droplet formation induced by surface tension.

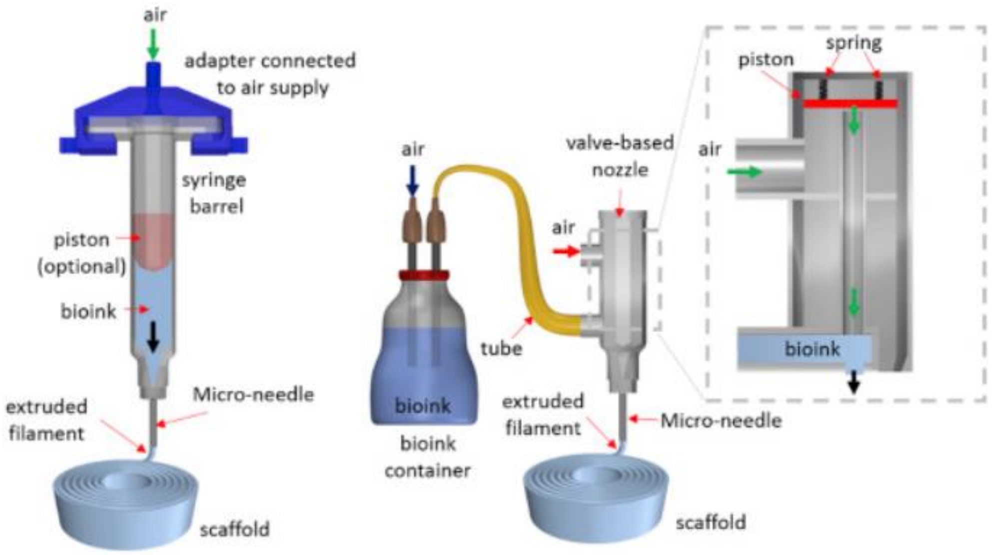

Figure 2.3-2 Pneumatic extrusion bioprinting: valve free (left) and valve-based [12]

2.4 Bioink for micro-extrusion bioprinting

Once a printing technique is defined, in this case extrusion bioprinting, the possibilities of different bioinks is further explored. Bioinks consist of a biomaterial solution containing living cells and/or biochemical molecules (e.g. ECM components). The recent developments on bioprinting technology comes with a need for suitable bioink. This ink has mainly two goals, to support cells of their growth and function as well as minimizing the effect of bioprinting (such as stress) on the viability of the cell without downgrading the stability and resolution of the construct. Hydrogels, microcarriers, cell aggregates (with subdivision of tissue spheroids, cell pellets and tissue strands) and decellularized matrix components are the four most commonly used materials in bioinks. Hydrogels are more appealing for bioprinting techniques because of their relatively easy implementation. [11], [13]–[15]

The printability of a bioink can be expressed in terms of how fluent it prints, the quality of the resolution and preservation of its structure after printing. Extrusion bioprinting demands viscoelastic characteristics such as shear thinning (viscosity decreases under shear strain), to protect the cells from stressors. In addition the bioink should be capable of self-healing in order to keep the printed structure intact and specific crosslinking mechanisms may be necessary. The ink should harden immediately after printing providing stability, the scaffold structure should also be bio- degradable and -compatible for *in vivo* applications and noncytotoxic. Moreover cell migration, adhesion, maturation and viability should be stimulated. [11], [14]

However there is always a tradeoff between stimulating cell migration and structural/mechanical properties (including the resolution). The first demands low viscosity, stiffness and crosslinking, while the second demands high viscosity, stiffness and crosslinking. This complicates the process of selecting a suitable bioink. In this thesis hydrogel will serve as the base material for a potential bioink. [16]

2.5 Hydrogels for extrusion bioprinting

Hydrogels are hydrated three-dimensional networks of crosslinked synthetic or natural polymers. When the hydrogel experiences gelation, cells are encapsulated in the 3D structure which aims to mimics the native ECM environment. Natural hydrogels are biodegradable, biocompatible and hydrophobic. The downside of these materials is that they do not maintain the initial shape of the design. Synthetic hydrogels can be designed with a specific set of properties and their mechanical properties are robust. In the case of bioprinting, injectable and shear-thinning properties are in particular interesting. However, in contrast with natural polymers, they are poorly biocompatible and excrete non-natural degradation products. Commonly hydrogel inks are polymer solutions, which are crosslinked directly after the printing process. Crosslinking can be done, among other methods, chemically (stimulated by ion concentrations) or physically (stimulated photosynthetic or by heat). [11], [13]

2.5.1 Natural and natural derived bioinks

Some of the typical natural polymers are gelatin, collagen, alginate, chitosan and agarose. In this study the focus will lie on alginate and gelatin natural polymers. [4]

2.5.1.1 Alginate

This widely natural derived polymer is an anionic polysaccharide and is harvested from the wall of brown algae and seaweeds. Calcium ions trigger the polymer to instantly form a tough hydrogel, this is to improve its shape stability as alginate on its own forms a soft gel. The advantages of this hydrogel include a fast gelation rate, a reasonably price and its biocompatibility. On the other hand interaction between cells is mainly blocked due to the hydrophilic property of alginate which hinder the cell receptors. To overcome this problem the alginate can modified with arginine-glycine-aspartic acid (RGD), which is a peptide that stimulates cell adhesion, or mixed with other hydrogels. *Jia e.a.* used RGD modified and oxidized alginate to, among other objectives, enhance cell viability. The experiments show a cell viability of over 90% with a viscosity range between 400 and 3,000 mm²/s. [14], [12], [17]

2.5.1.2 Gelatin and GelMa based hydrogel

Gelatin is a hydrolyzed collagen, it's either obtained through acid-based hydrolysis (type A) or base-based hydrolysis (type B). Apart from supporting cell growth, it is able to crosslink at low temperatures. A mixture of pure gelatin and water results in a thermosensitive hydrogel, gelatin additionally possesses better soluble than pure collagen. At the critical temperature, somewhere between 25 and 35°C, the liquid gelatin forms a sol-gel. One major drawback is that above the critical temperature the gelatin has a low viscosity which makes it challenging to bioprint. Blending gelatin with an additional, more viscous, polymer can overcome this problem. [14], [18]

A widely used gelatin blend is GelMa (gelatin methacrylamide). This hydrogel is fabricated by reacting gelatin with methacrylic anhydride as shown in Figure 2.5-1. Apart from being biocompatible it is also low-cost and allows easy processing. Moreover this modification of gelatin enhances the threshold of liquification above 35°C. *Billiet e.a.* and *kolesky e.a.* have experimented with gelMA, the results indicate cell viability over 95 %. The methacrylate (MA) is photopolymerizable, therefore it can be crosslinked by UV light. The elastic modulus can be modified by changing the concentration of methacrylation, pure gelatin and the temperature. [11], [19]

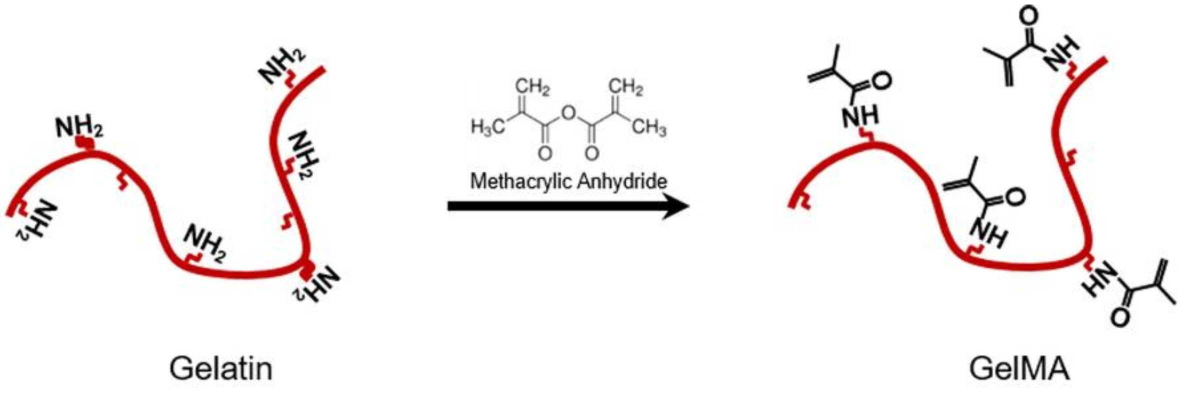

Figure 2.5-1 The fabrication process of gelMA through methacrylic anhydride [22]

2.5.2 **Crosslinking hydrogels**

The discussed hydrogels can be crosslinked according to their own capabilities. There are different types of crosslinking techniques, chemical, physical and enzymatic crosslinking. In this paragraph the focus lies on physical and chemical crosslinking, in the context of hydrogels such as gelatin, gelMA and alginate. The first can be divided into thermal crosslinking and photoinduced crosslinking. The second can crosslink based on pH properties or ionic compounds. [12], [20], [21]

2.5.2.1 Physical crosslinking

Physical crosslinking can be achieved by ionic or hydrophobic interactions, entanglement of polymer chains and hydrogen bridges. The major advantage is the lack of crosslinking agents, these may have a toxic effect on the cells in the bioink. Physical crosslinking, in the form of thermal crosslinking, has poor mechanical properties, and is held together by weak, reversible, interactions (as shown in Figure 2.5-2). Thermal crosslinking can however provide instant stability when printing hydrogels, therefore they are implemented and further stabilized post-printing, often by chemical crosslinking. [21]

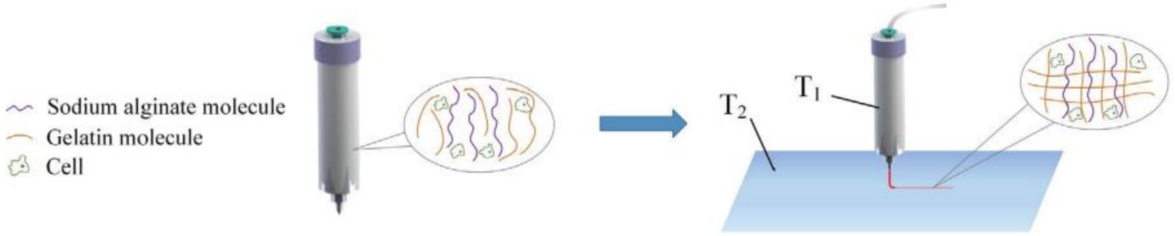

Figure 2.5-2 Thermal crosslinking of sodium alginate and gelatin bioink [30]

Another type of physical crosslinking is photo crosslinking. Because of the methacryloyl substituent groups in gelMA this hydrogels has the potential to be photo crosslinked. When gelMA is mixed with a photo initiator, for example Irgacure 2959 or riboflavin, chain polymerization is initiated once the mixture is exposed to UV light (with suitable wavelength). The process allows mild conditions such as room temperature and neutral pH. It is an advantageous method for crosslinking because it is nontoxic and provides stable bonds, however the amount of desired crosslinking is difficult to obtain. [18], [22], [23]

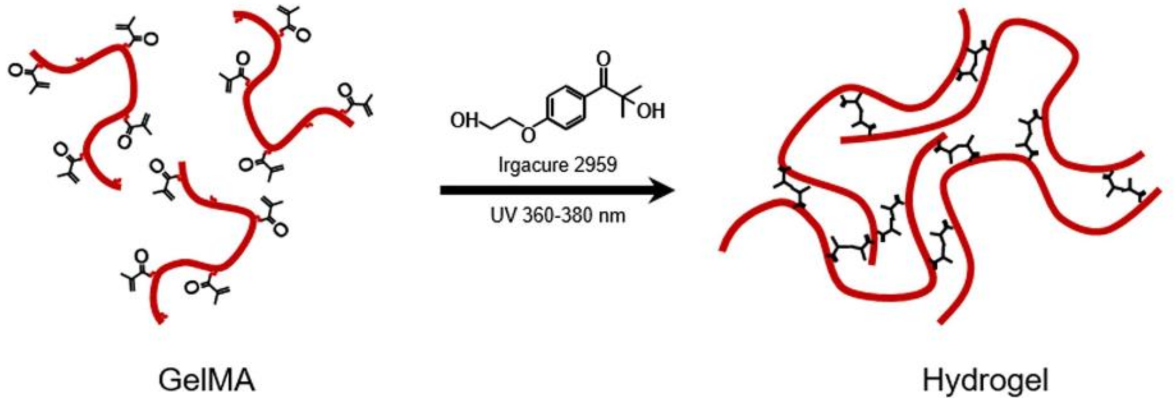

Figure 2.5-3 Photo crosslinking gelMA under UV irradiation [22]

2.5.2.2 Chemical crosslinking

Covalent bonds as a result of chemical crosslinking post-processing provide a stable construct and high mechanical strength. During crosslinking the functional groups of amino acids are bonded. Some examples of crosslinkers are carbodiimides, formaldehyde and tannic acid.

These chemical crosslinkers generally increases the toxicity within the material, which can have devastating effects on the cell viability. The crosslinker genipin is natural and low-toxic, which is interesting for bioprinting applications. However it could have immunogenic effects when crosslinking. [13], [23]

2.5.3 Hydrogel blend with hydroxyapatite

As discussed, crosslinking hydrogels can augment the stability and mechanical properties of hydrogels. Nevertheless there are alternatives to compensate for this disadvantage, such as using hydroxyapatite (HA). HA is a natural mineral that occurs in bone tissue, thus is specifically used for bone tissue engineering applications. It has the potential to enhance cell attachment and osteogenic differentiation. To illustrate the impact of HA on the structural stability, e.g. stiffness, figure 2-10 shows the Young’s modulus as a function of the HA (in this case nanopowder). The experiment is conducted by *Chen e.a.* who used a mixture of gelMA and HA nanopowder to compose microgels. [24], [25]

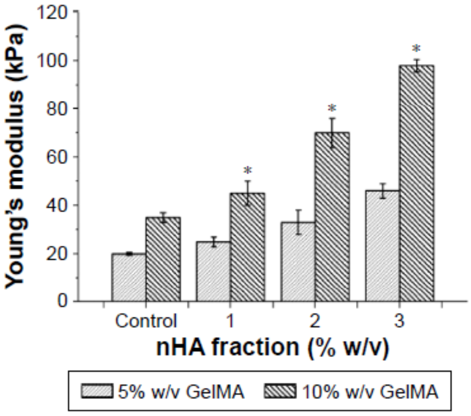

Figure 2.5-4 Young's modulus as a function of the HA concentration used in microgels with inkjet printing (*P 0.05) [24]

2.6 Hydrogel parameters for extrusion bioprinting [26]

The major advantages of using hydrogels for 3D bioprinting applications and the most common hydrogels have been discussed in previous paragraphs. The next step is to investigate how different properties have different outcome on the printing fidelity and cell viability and how these properties can be controlled. The properties are physicochemical, with the two most important parameters being the rheology of the material and the crosslinking method. Together with the printing parameters such as nozzle diameter, fabrication time and shear stress (with respect to the boundary conditions of the chosen printing technique) they influence the printing fidelity and cell viability, proliferation and differentiation as shown in Figure 2.6-1. The biggest challenge that still remains is finetuning the parameters in such a way that they satisfy both the printing fidelity and the cell viability simultaneously.

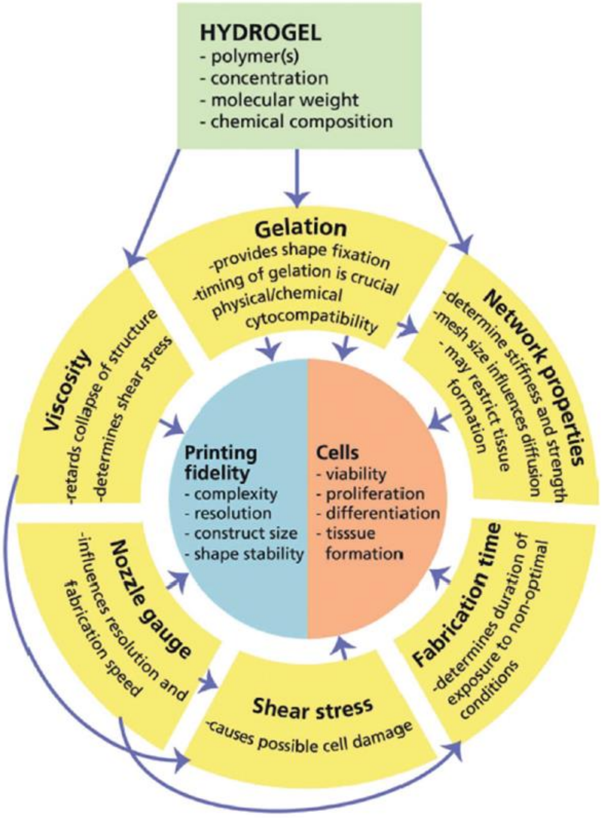

Figure 2.6-1 Influential factors on printing fidelity and cells [11]

2.6.1 Viscosity and shear thinning of thermos-responsive hydrogels

The viscosity of a thermo-responsive hydrogel, such as gelatin and gelMA, is dependent on the temperature, its molecular weight and the concentration of the polymer. Adjusting the temperature allows tuning of the sol-gel state. Below a critical temperature the hydrogel undergoes a sol-gel transition. High viscosity of a bioink results in extrusion printing under increased shear stress, the most important consequence is damaging of cells. On the other hand viscosity also has a significant influence on the shape fidelity, higher viscosity forms filaments on the substrate during printing as to spreading strands with lower viscosity. [11], [14], [27] *Billiet e.a.* conducted rotational viscosimetry measurements with gelatin methacrylamide to plot the viscosity as a function of the temperature and concentration. The concentration of the hydrogels ranges from 5 w/v% up to 20 w/v% as shown in Figure 2.6-2. It is clear that the viscosity decreases with increasing temperature and decreasing concentration. Furthermore the influence of the cell density (HepG2 cells were used) on the viscosity was tested. The results show that the presence of the cells lower the viscosity of the ink. [17]

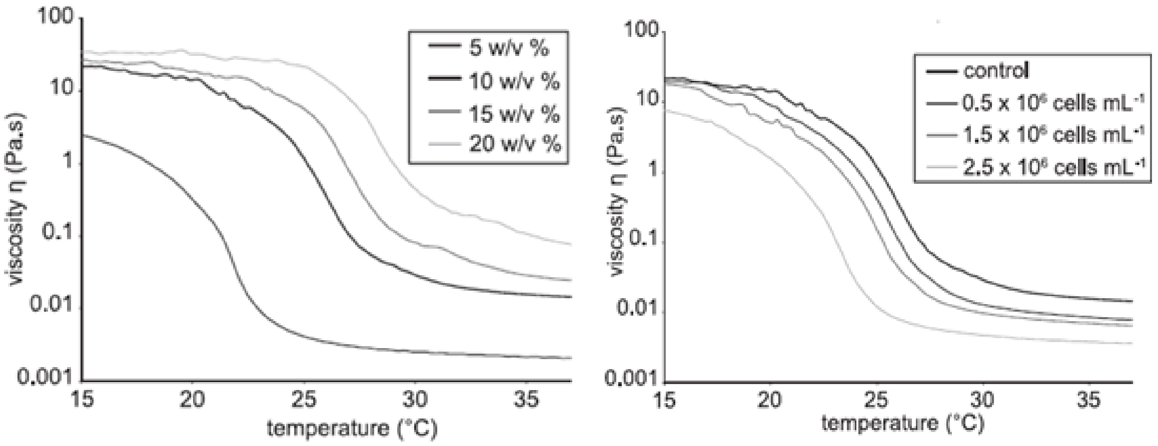

Figure 2.6-2 Rotational viscometry measurements on gelatin methacrylamide as a function of temperature, concentration and cell density [28]

A hydrogel, being a non-Newtonian fluid, exhibits viscoelastic properties, meaning there is a partially elastic as well as a viscous behavior of the material when deformed. This causes a phase shift (δ) between the stress (τ_0) and strain (γ_0) response. This is mathematically expressed through the shear moduli (G) by the following formula [28], [29]:

$$G' = \frac{\tau_0}{\gamma_0}\cos\delta$$

2.6-1

$$G'' = \frac{\tau_0}{\gamma_0}\sin\delta$$

2.6-2

$$G^* = G' + iG''$$

2.6-3

The complex shear is consequently:

With G*: complex modulus
G’: storage modulus
G”: loss modulus
δ : phase shift
γ_0 : shear strain
τ_0 : shear stress
i : imaginary unit

The nozzle plays a significant role as well in determining the strain rate, therefore its size, shape and temperature must be taken into account. The mechanism of shear thinning at molecular level allows polymer chains to slide over one another instead of getting tangled, this allows smooth extrusion through the nozzle of the printer. A phenomenon that occurs when polymers in general are pushed through a nozzle, is die swell. Due to the transition between high stress exerted inside the nozzle and low stress once the fluid is pushed out, the polymer tends to swell. [14], [29]

Given that hydrogels are non-Newtonian materials, gives them the rheological property of shear thinning. This means that the viscosity decreases when the strain rate increases, this last one is controlled by increasing the pressure of the bioprinter. Shear thinning, when increasing the strain rate, can be a powerful tool to protect cells from damage and improve the resolution by providing a smooth flow throughout the nozzle. Additionally it can overcome blockage of bioink in the nozzle during printing. Figure 2.6-3 illustrated that cells undergo an increased amount of stress towards the inner wall of the nozzle and cartridge which can eventually lead to cell death. This occurs frequently at the walls where shear stress is at its highest point. [14], [29]

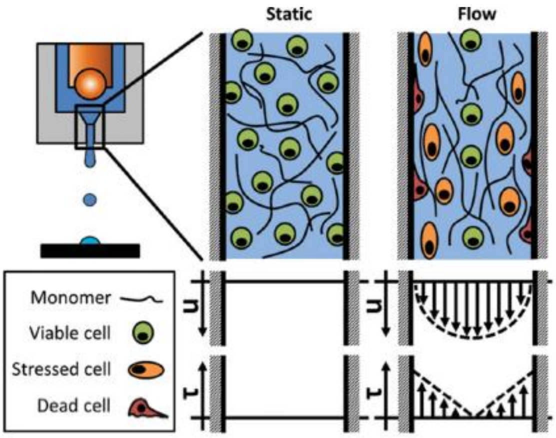

Figure 2.6-3 The effect of stress on cell viability inside the nozzle with distribution of shear stress (τ) and velocity (u) [29]

To highlight the shear thinning behavior of hydrogels. Figure 2.6-4 shows the shear rate as a function of the shear stress. The experiment is conducted by *Billiet e.a,* the same conditions apply as figure 2-12. It is clear that the slope of the shear stress decreases with increasing shear rate, in contrary to Newtonian fluid where there is a linear relationship between the shear stress and shear rate. Once again the data shows how increased cell density drops the viscosity. [28]

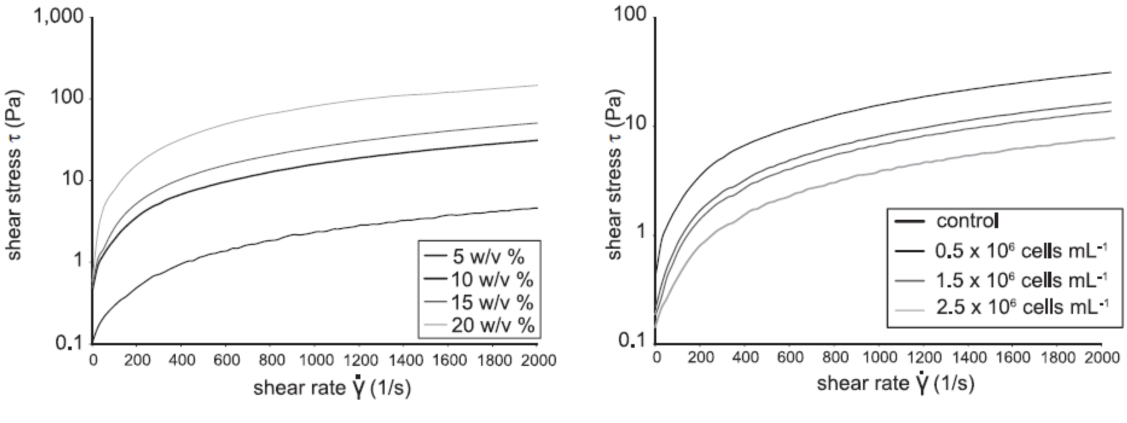

Figure 2.6-4 Rotational viscosimetry measurements on gelatin methacrylamide as a function of concentration and cell density [28]

2.7 Process parameters for micro-extrusion bioprinting

2.7.1 Printing parameters that influence the fidelity of the construct

As discussed hydrogel properties have a major impact on the outcome of the printing process, however as briefly mentioned, the printing parameters of the process also have a significant influence. A series of parameters need to be determined before printing, such as the air pressure, speed, nozzle-substrate height and nozzle temperature as shown in Figure 2.7-1. These parameters depend for the most part on the bioink properties. Nonetheless the resolution of the printed tissue is closely related to the nozzle diameter (usually in the ranges of 0.10 and 0.50 mm), printing speed and applied air pressure. Whether the tissue is stable and preserves its shape depends mostly on the viscosity of the ink. The viscoelasticity and shear thinning properties of the ink also have a significant influence. A major challenge is increasing the print resolution and speed. A resolution of 5 μm and 200 μm has been achieved with a feed rate between 10-50 μm/s, however this specific case applies for extrusion printing with nonbiological material. [14], [28], [7], [30]

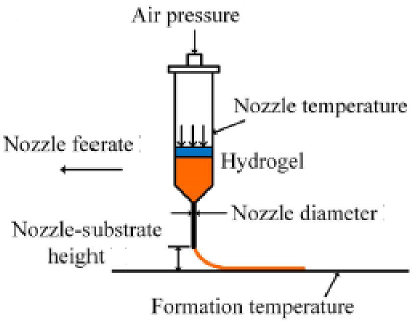

Figure 2.7-1 Printing parameters for extrusion printing [30]

The applied pressure is seen as the most important parameter as it is directly in relation with the printed line width. It is required to be over a threshold pressure, in order to overcome the surface tension. However if the pressure is too high, extrusion happens at a quick pace and jetting might occur, which means there is little to no control over the extrusion process. *He e.a.* conducted experiments in order to explore the suitable pressure range for their specific hydrogel composition, which is a mixture of 8% gelatin and 2.5% sodium alginate. They did this by measuring the distance from the separating location of the hydrogel to the nozzle as a function of temperature (viscosity) and pressure. The two most important thresholds are the pressure where the material starts to flow and where the material causes jetting, this is an uncontrolled flow. So from the deducted experiment the boundaries of applied pressure was attained, in this case between 15 – 30 kPa for a 0.4 mm nozzle.

An additional parameter that has a significant influence on the line with is the speed/federate of the nozzle. *Billiet e.a.* plotted the strut diameter as a function of the printing speed and pressure using a 200 μm cylindrical needle. The hydrogel used is 10 w/v% GelMA printed at 27.5°C. It is clear, by examining Figure 2.7-2, that increasing the printing speed and decreasing the printing pressure will aim for a better resolution of the structure with a smaller strut diameter. [28], [30]

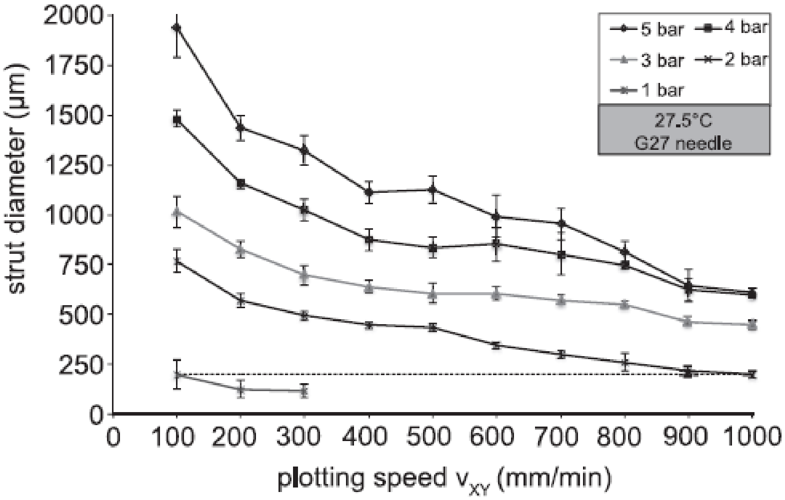

Figure 2.7-2 Strut diameter as a function of printing speed and pressure [28]

As shown by Figure 2.7-1, the distance of the printbed to the nozzle is another parameter. Changing this distance will change the response lag and line width with respect to the printing speed. Again, *He e.a.* illustrated this by observing the effect of the printing height when printing lines with 90° angles, using a nozzle diameter of 0.5 mm. Increasing the height with a millimeter (from 0.1 to 1.1 mm), lead to an increase in the line width (the range varied from about 0.95 mm up to 1.30 mm). Another interesting phenomenon observed was the effect of the response lag. When the printing height is under a certain threshold the 90° angles were clearly recognizable, whereas above a stated limit the angles were curved and no sharp corners were detected. Moreover the printing angle is a delicate parameter by itself, using a smaller acute angle could possible cause an overlap, therefore the amount of hydrogel distributed is no longer uniform over the whole structure, this error accumulates with each printed layer. The problem can be avoided by simply excluding acute angles from the printing process, or the printing speed can be increased in the areas affected (this is double the speed in general since the areas of overlap holds twice the amount of extruded hydrogel). [30]

A common approach to 3D bioprinting is the printing of lattices. However an undesirable phenomenon occurs, namely diffusion, which is influenced by the distance between two printed lined. The most critical area is the intersection of the printed lines where diffusion takes place as a consequence of gravity. Due to the diffusion rate the theoretical line width does not comply with the experimental line width. The influence of the line distance (D_L) is illustrated in Figure 2.7-3. [30]

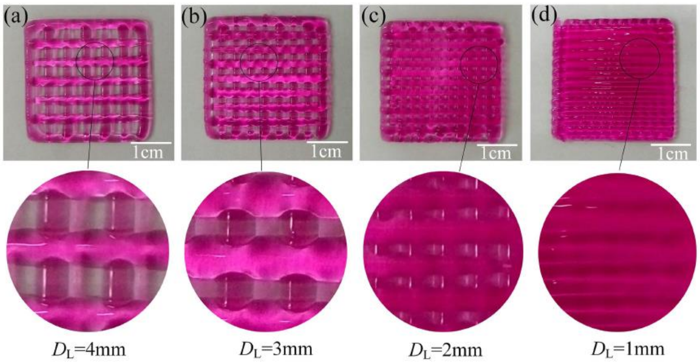

Figure 2.7-3 The diffusion of the hydrogel as a function of the line distance (DL) [30]

Apart from the discussed diffusion, when working towards a 3D structure or construct, fusion and collapses can also have a devastating effect on the resolution of the structure. Figure 2.7-4 shows ΔH when printing one or two layers, this is the effect of collapses and diffusion. Δh effects 3D structures, here two layers undergo a fusion, decreasing the total height. This last effect is more pronounced in 3D structures than the effect of ΔH, and is influenced by the printing time and the temperature of the platform. Keep in mind that the discussed factors (Δh and ΔH) also depend on the viscosity of the hydrogel (a low viscosity has a negative impact on the resolution). [30]

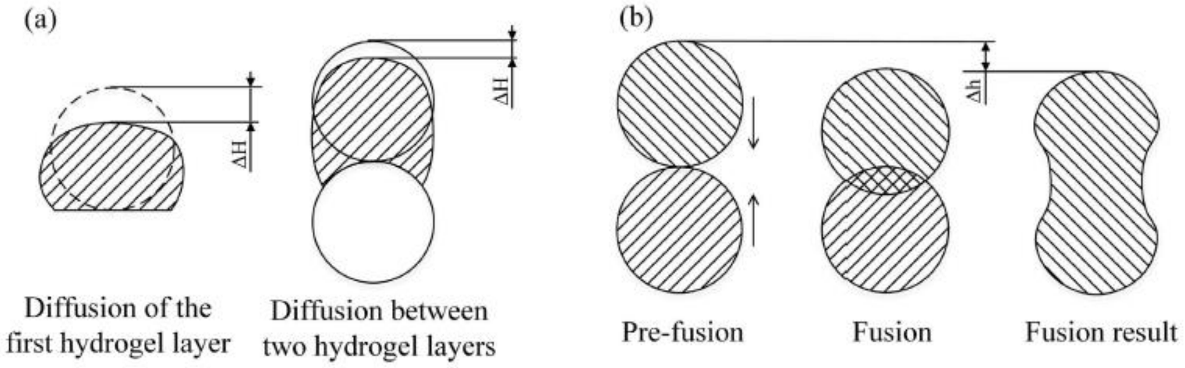

Figure 2.7-4 Deformation of the hydrogel a) diffusion of one and two hydrogel layers b) fusion of layers in a 3D structure [30]

2.7.2 Printing parameters that influence the cell Viability

One of the highest priorities is cell viability. This can all be influenced by, among other thing, the amount of printed layers, the resolution, the printing time, the dimensions of the to be printed tissue and not to forget the nozzle temperature. [4] The threshold temperature for the nozzle as well as the chamber is 37°C (the gelation temperature of the bioink should be brought into consideration). Cell viability in relation to the bioink itself depends mostly on the cell concentration, the cell type, the temperature of the bioink as well as the network properties and the crosslinking process.

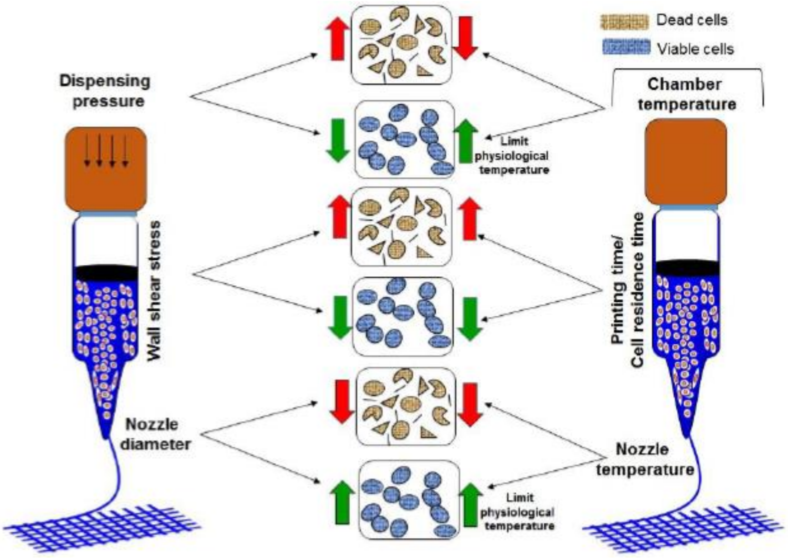

Figure 2.7-5 Effect of printing parameters on cell viability [14]

Figure 2.7-5 shows the printing parameters that have an effect on the cell viability. Increase the dispensing pressure would decrease the cell viability because of the increasing shear stress. Decreasing the nozzle diameter would decrease cell viability. The wall shear stress is dependent on the nozzle diameter as well as the dispensing pressure and the concentration of bioink, it decreases cell viability. Up to 37°C the viability increases with increasing temperature of nozzle and chamber. Increasing printing time would decrease cell viability, as they have been exposed longer to the printing environment. [14]

Blaeser e.a. inkjet printed LP2P mouse fibroblasts in a series of 44 experiments. Cell viability was tested on the day the construct was printed. According to the applied shear stress three groeps were divided, their average and standerd deviation is presented on the graph below.

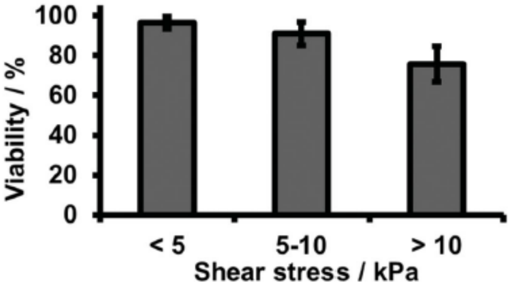

Figure 2.7-6 Cell viability as a function of shear stress [29]

Although the printing technique is inkjet printing, the concept applies to extrusion printing as well. Cell viability increases as the shear stress, which is induced by the applied pressure, increases. [29]

Billiet e.a. experimented on the influence of the nozzle shape, diameter and pressure on the cell viability. The material used is a 10 w/V% GelMA solution with HepG2 cells, no crosslinking has been done. The nozzle diameters are 0.20 mm (G27) and 0.15 mm (G30). The data from the graph shows that increasing the pressure has a negative effect on the cell viability as well as decreasing the nozzle diameter.

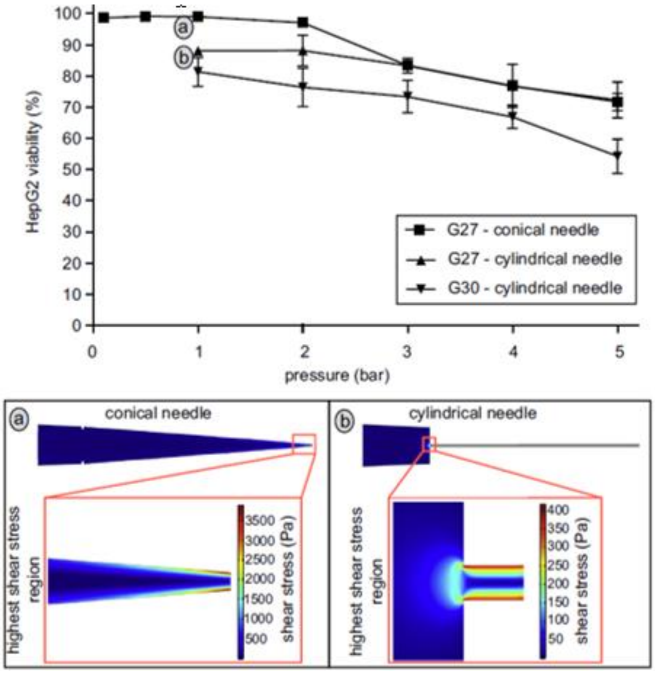

Figure 2.7-7 The viability of HepG2 as a function of the applied pressure and needle shape and diameter a) finite element analyses of the shear stress on the conical needle at 1 bar internal diameter 200 µm b) finite element analyses of the shear stress on a cylinder [28]

Additionally the distribution of the shear stress on the conical and cylindrical needle is presented on Figure 2.7-7. This image shows that the area affected by increased shear stress is along the tip of the conical needle and along the outer surface of the cylindrical needle, suggesting that the conical needle over the cylindrical is preferred. However the maximum stress of the conical needle is significantly higher (about a factor nine) than the maximum peak stress of the cylindrical needle. The assumption according to *Billiet e.a.*, is that for a low pressure the conical needle seems most interesting, because in this case the bioink passes slowly through the nozzle and the area effected by a high shear stress is smaller in the case of the conical nozzle. Moreover at a higher pressure the negative effect of the high shear stresses on the cell viability overpower and a cylindrical needle is preferred. [28]

2.8 Conclusion

To the present day bone grafting still uses traditional methods i.e. allogenous, autogenous and prosthetic bone grafting. However these methods have certain complications, such as infections, immunological rejection and limited tissue supply. BTE can be viewed as an answer to these complications.

With advantages such as customization and potentially more control over the desired geometry, AM techniques are preferred over more conventional techniques to practice TE. In this thesis the specific AM technique chosen is extrusion bioprinting. Advantages are, reaching high cell densities (cell spheroids) and a wide viscosity range (between 30 mPa/s to above 6 x 10^7 mPa/s) can be implemented.

Common biomaterials used in bioprinting are hydrogels, because they generally provide an ideal environment for implementing cells as they aim to mimic the ECM. The downside of these hydrogels is that they lack mechanical strength, to encounter this problem HA nanopowder hydrogel blend has been suggested to augment the stiffness of the printed construct or structure. As a starting point for this study, gelatin is chosen as the base material of interest with the possibility incorporating HA nanopowder. Furthermore gelatin can be modified to form gelMA which can have a favorable impact on the mechanical and thermal properties. Crosslinking is of importance with regards to the whole bioprinting process. The augmentation of the mechanical properties is much more outspoken in the case of photoinitiated crosslinking and chemical crosslinking compared to thermal crosslinking. However, for this thesis, thermal crosslinking is applied to create a first instant stability during the printing process. The idea is that for future work, thermal crosslinking is applied, preceding another crosslinking method.

A huge challenge in bioprinting is to print a construct with a high printing fidelity and cell viability. These factors are controlled by the parameters of the printing process and the bioink properties. An occurring problem is that often the factors that have an advantageous effect on the printing fidelity have a negative effect on the cell viability and vice versa. It is of importance to find a balance between the printing fidelity and cell viability. In this thesis the printing fidelity is the main focus, thus the most important hydrogel properties and printing parameters are examined.

3 METHODOLOGY

3.1 Workflow

The project is divided in three major phases, namely the study of hydrogel material, the analyzing and improving of the printing process and the experimental phase, where the goal is to find the ideal printing parameters.

The first phase starts with a fundamental **literature study**, to gain more knowledge on the subject and existing experiments on 3D bioprinting a structure or construct. Based on this knowledge potential **printing material** is chosen as well as a suitable **crosslinking method** for the specific biomaterial. The material is then produced in a chemistry lab and the **rheological properties are studied** with DSC tests, viscosity tests and microscopy. The crosslinking methods of interest are thermal, chemical and photo-induced. Once the idea of material and crosslinking method is established, adjustments to the 3D printer are made to **improve thermal crosslinking post-printing**. Namely a cooling plate for the printbed is designed and manufactured to provide structure stability of the hydrogel. This is the main focus of the second phase.

The third phase is divided into two steps, experiments and validation. **Printing** is the key part of this phase. The data collected from phase one is processed, based on this data assumption are made, with the help of the literature study, about the ideal printing parameters. This is the starting point, from then on **printing is based mostly on trial and error**, if time permits it a design of experiment is possibly executed. Once materials are successfully printed the validation step is started. In this step the **fidelity and printability is tested**, more specifically the quality of the resolution, porosity and shape stability of the construct. The evaluation is through microscopy and visually.

3.2 Project structure

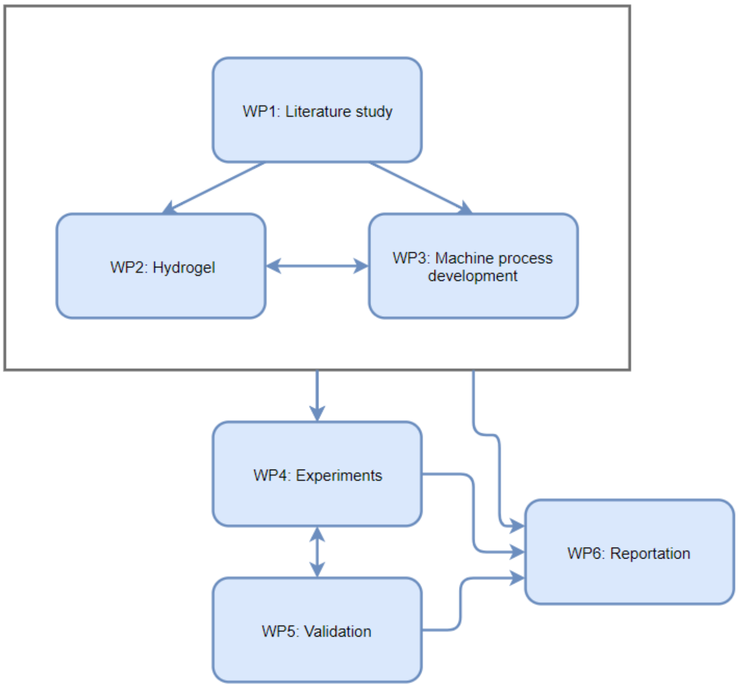

Figure 3.2-1 Project structure

The block diagram consists of **6 work packages** that will be thoroughly discussed. The first three work packages are presented as a cluster, this way the whole of the packages can be related to other work packages. The input/output relationships are represented by the arrows in the scheme.

The starting point of the project is **WP1: literature study**. In this work package information is gathered by reading scientific papers, books etc. and it serves as a backbone for WP2 and 3. **WP2: Hydrogels** focusses on the properties of different hydrogels. Input is gained from WP1 to substantiate the choosing of biomaterials and crosslinking methods. Rheological tests are performed in this work package to gather data about the behavior of specific biomaterial. It is in this work package that the biomaterials of interest are chosen and manufactured. **WP3: Machine process development** focusses on any adjustments that need to be made to the machine, in this case a cooling plate to improve crosslinking post-printing. The whole design cycle from concept to manufacturing of the cooling plate is included in this work package. If an interesting technique to improve the machine process emerges from the literature study it can be implemented in this work package. WP2 and WP3 serve as an input for each other, since the crosslinking method is decided in WP2 and technical adjustments to accomplish this method is the objective of WP3.

In **WP4: Experiments** 3D printing with the bioprinter commences. The work package includes a learning phase, in order to understand the functioning of the machine. The main objective is however, to successfully print biomaterial (this includes the crosslinking process). All the information from WP1, 2 and 3 are crucial inputs for this work package. WP3 provides the possibility, from a technical aspect, to carry out the printing process as desired. WP2 provides the printed material and together with WP1 the data that forms the backbone for the printing parameters. The printed materials are an input for **WP5: Validation**. In this work package the constructs are evaluated based on metrology and microscopy. The results of the evaluation are presented with respect to the printing parameters used in WP4. Conclusions are drawn from the validation and this output is again used as an input for WP4, so improvements of the printing process can be made based on the validation results.

It is crucial to keep track of any information gained during the course of the project, therefore all the preceding work packages serve as an input for WP7 reporting. In this work package a record is kept of any data gained.

3.3 Inkredible+ 3D Bioprinter [31]

The printer used for the experiments is a pneumatic based microextrusion bioprinter acquired from the company *Cellink*, the model is the **Inkredible+ 3D Bioprinter**. This printer uses a bottom-up approach to print bioink layer by layer to form a 3D construct. It includes dual printheads which allows two different biomaterials to be printed simultaneously in one printing cycle. The printheads include a heating function as well, which is interesting for hydrogels with a gelation point above the ambient temperature. Additionally an UV LED curing system is available for photoinduced crosslinking. The *Inkredible+* can be operated with specific software or as a standalone package because of its built-in LCD controller and is equipped with USB and SD-card inputs.

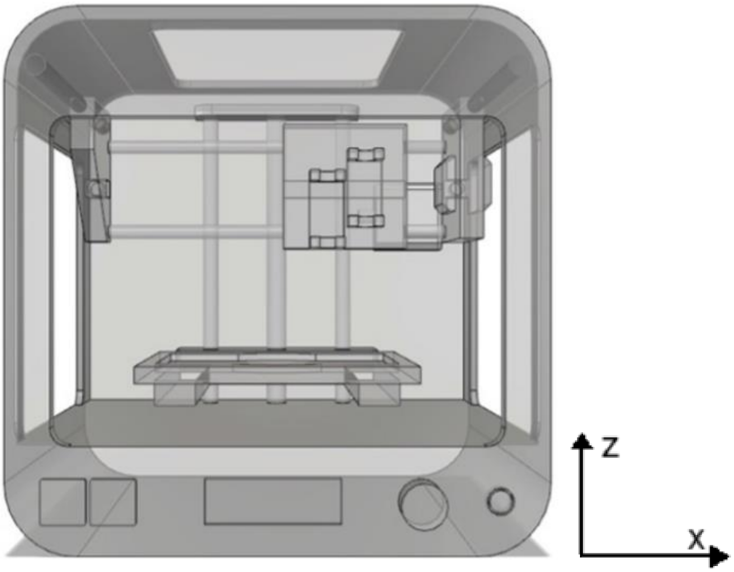

Figure 3.3-1 Schematic presentation Inkredible+ 3D Bioprinter [30]

3.3.1 Specifications Inkredible+ 3D Bioprinter

The Bioprinter can be connected to a standard European power outlet (230 VAC, 50 Hz). The operating power of the printer is 24 VDC, 6A. Furthermore it requires an oil free air compressor to provide the desirable pressure. The constraints of the operating parameters are provided by the *Inkredible+ 3D Bioprinter manual*, and are as followed:

Resolution: 100 μm
Precision XY: 10 μm
Precision Z: 2.5 μm
Wavelength UV LED curing system: 365 nm
Viscosity range: 0.001-250 Pa.s
Response time printhead: 5 ms or less
Minimum/maximum operating pressure: 1 kPa / 700 kPa
Set Pressure rage: 5 to 400 kPa
Sensitivity: 0.2% F.S. (0.8 kPa)
Repeatability: ±1% F.S. (4 kPa)

3.3.2 Software

The software that accompanies the 3D printer is *Repetier-Host*, an open source software where the construct is modelled (3D CAD model is created). It has a built-in slicer software, *Slic3r*, to convert the model into 3D printing instructions. The accepted file types are STL, OBJ and AMF. *Slic3r* converts these files to G-code for the printer to comprehend. The software supports windows, Mac OS X and Ubuntu Linux. Uploading files is done either via the USB connection or SD-card.

3.3.3 Equipment

The printing equipment used is customized for the *Inkredible+* and provided by the manufacturer (*Cellink*). This equipment mainly consists of the cartridges and nozzles. Nozzles are available with a diameter starting from 0.05 mm up to 1.540 mm. Their length varies from 6.35 mm to 38.1 mm.

The cartridge typed used has a volume of 3 ml and comes with a piston and end cap as shown in Figure 3.3-2.

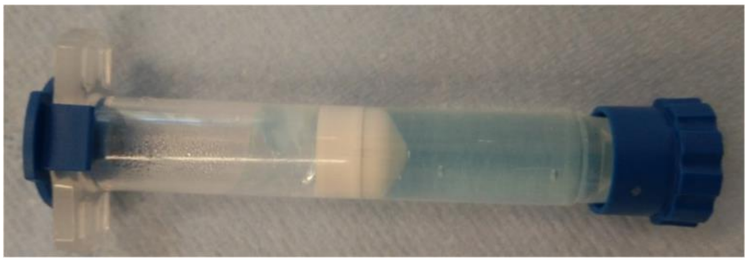

Figure 3.3-2 Cartridge with piston and end caps

The nozzle used are conical shaped polypropylene nozzles with a length of 32 mm. There are three different types used, distinguished by their colors, namely blue, red and white. Their respective diameters are 0.41 mm (22G), 0.25 mm (25G) and 0.20 mm (27G).

Figure 3.3-3 Cartridge and nozzle mounted onto printhead

3.4 Printing material and crosslinking method

3.4.1 Cellink start [32]

The primary material used for printing is *Cellink start*. This material is a polyethylene oxide blend that is used as a sacrificial material. The exact substance of the material is unknown as this is one of *Cellinks* own material blends. It can be argued that the base material is Pluronic mixed with nanocellulose due to the appearance and its behavior in terms of printing and viscosity. Nevertheless there is no guarantee that this is the case.

Given the fact that this material is designed and manufactured for the sake of 3D printing with the *Inkredible+* and other bioprinters sold by *Cellink*, the rheological properties should be suitable for the process. The material can additionally be printed at room temperature. These advantages allows for a clear focus on the printing process itself.

3.4.2 Gelatin

The main, self-manufactured, product used as printing material is gelatin, derived from bovine skin. As mentioned in chapter 2.5.1.2, gelatin is a hydrolyzed collagen. In this thesis type B, gelatin based on base-hydrolysis, is implemented. Collagen, being the key protein for multiple connective tissue such as skin and bone, consists of a triple helical structure representing three polypeptide chains, which in turn are made up of a sequence of amino acids. First protein extraction takes place by boiling the, in this case, bovine skin in water and afterwards the hydrolysis takes place. [33]

The gelatin is obtained from *Sigma-Aldrich* and has a Bloom number of 225g. This number is with respect to the weight required to depress a standard sample of gel 4mm deep, this is measured by a Bloom gelometer. In other words the Bloom number is an indication of strength. [34]

3.4.3 hydroxyapatite

As discussed in the literature study gelatin lacks mechanical strength, which is a downside specifically in bone tissue engineering. To partially overcome this problem a gelatin HA nanopowder blend can be manufactured. The powder is attained from Sigma-Aldrich, it is biocompatible and promotes proliferation and adhesion of (bone-forming) cells. The particle size is under 200 nm. [35]

3.4.4 Crosslinking methods

The crosslinking of gelatin is executed through thermal crosslinking. The platform of the printer is held at 10 °C (given that the ambient temperature does not exceed 22 °C), so when the gelatin makes contact with the platform it instantly crosslinks and stabilizes the material. A cooling platform is manufactured to implement this method. As discussed in previous chapters the interactions caused by thermal crosslinking are weak and reversible, thus it is a first approach to crosslink the material and additionally chemical or physical crosslinking is required in a later stadium in order to form strong covalent bonds.

For the *Cellink start* material there is no crosslinking method foreseen as this material is used as a sacrificial material.

3.5 Measuring Equipment

3.5.1 DSC Q2000 T.A. Instruments [36]

Differential Scanning Calorimetry (DSC) is a method to plot measured heat fluxes as a function of a given temperature range. The idea is to gather information about thermal transitions of a specific material. In this case the main objective is to determine the sol-gel transition temperature of the chosen hydrogels as well as studying their thermal behavior.

The Differential Scanning Calorimeter used is the **Q2000 T.A. Instruments**. It is capable of plotting temperature ranges from -180 °C to 725 °C with a heating rate between 0.05 °C/min and 100 °C/min. It has an accuracy of 0.1°C and a precision of 0.01 °C. The maximum sample size is 2000 mg (in practice up to 300 mg). The samples are placed in an aluminum crucible which has a set of implementations, such as standard, crimped and hermetic. Furthermore the inert atmosphere of the samples are realized with argon, helium or nitrogen. The software tool used is **Universal Analyses**, the data can be visualized as well as edited with the software.

3.5.2 Digital microscope Hirox KH-8700 [37]

Microscopic images are taken with the **digital microscope Hirox KH-8700** available at *Campus De Nayer*. This microscope comes with a controller that allows the user to control the movement of the Z-axis easily, as well as adjusting the lighting. The images captured with this microscope have a maximum pixel resolution of 58 Mega-pixels (8600 H x 6600 V) and can be stored in different formats such as JPEG and BMP. Furthermore the lighting equipment consists of a high intensity LED with a color temperature of 5700K.

The microscope is equipped with a revolver zoom lens (model MXG-2500REZ). The magnifications are between 35x to 2500x with a field of view (FOV) ranging from 8mm to 0.12mm. The revolver is made up of three lenses: Low-range, mid-range and high-range lens.

The most interesting feature of this microscope, for this thesis, is probably the autofocus feature. It captures a focused 2D image of a surface with relief. The user provides the upper and lower limit of the Z-axis and the microscope takes focused images between these limits combining them into one single focused image.

3.5.3 Rheometer MCR 501 Anton Paar [38]

For rheological experiments the **MCR 501 Anton Paar** stress controlled rheometer is used as a parallel plate rheometer with a diameter of 25 mm and a gap of 1 mm. The rheometer is capable of providing temperatures from -40 °C to 1000 °C. The torque that can be applied ranges from 0.01 µN.m and 300 mN.m, with a resolution of 0.1 nN.m. The angular frequency ranges from 10^{-5} to 628 rad/s, the resolution of the displacement is 0.01 µrad. To keep the sample stable the lid is equipped with an evaporation blocker and a solvent trap, in this case H-PTD 150, at the bottom plate as well.

Figure 3.5-1 Manufacturing of mold

Figure 3.5-2 Silicon mold, finished product

In order to perform measurements under the gelation temperature, the right geometry of the samples must be provided. Since ordering molds from the U.S. would take an excessive amount of time, a silicon mold was manufactured. A case was 3D printed and metal disks (35 mm diameter, 2 mm thickness) were provided to give the samples the desired shape and surface quality (the surface finish of 3D printing would not have sufficed). The protocol of the manufacturing process can be found in appendix B.2.

3.5.4 Density meter [39]

For performing density measurements the **Sartorius YDK03** density determination kit is used. This method is based on the Archimedes principle. Knowing that the material undergoes a buoyancy force that essentially is the weight of the liquid being displaced by the material and that the volume of the displaced liquid is the same as the material, the density can be calculated by the device.

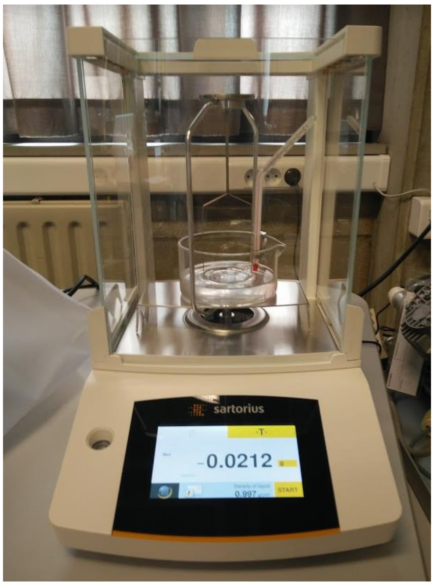

Figure 3.5-3 Sartorius YDK03

There is a lack of information regarding the accuracy and resolution of the measuring device. The manual seems to imply that certain errors could make it difficult to claim the devices resolution. Some examples of possible external errors are air bubbles on the sample, a variation in ambient temperature or humidity.

3.5.5 Scanning electron microscope (SEM) [40]

The SEM is a **TESCAN VEGA3** and has a resolution of 3nm when using 30 keV. With a working distance of 10mm the field of view is approximately 7.7 mm. The microscope is used for studying particles where the resolution of the *Hirox digital microscope* is not sufficient enough.

Figure 3.5-4 TESCAN VEGA3 [40]

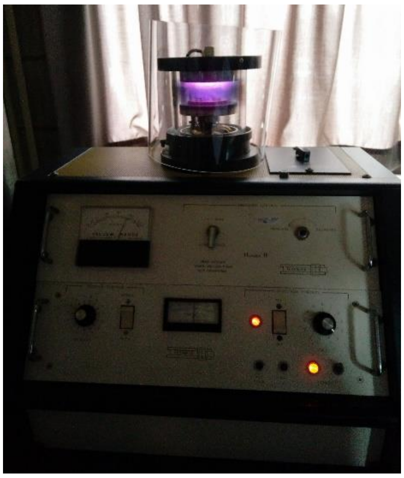

Figure 3.5-5 Sputtering device

Furthermore to prepare the samples gold sputtering is performed. A thin layer of conductive material (in this case gold) is sputtered on to the sample. This is to prevent an electron beam from charging the material when the electron microscopy is performed.

3.5.6 Thermal camera [41]

A thermal camera is used several times i.e. to validate the cooling plate as well as the heating elements as will be discussed in chapter 5. The camera used is the **FLIR 300A** which operates between environmental temperatures of -15 °C and +50 °C. De temperature range of the object itself is -20 to 350 °C with an accuracy of ±2% of the reading. The focus can be done either manually or automatically. The camera has a resolution of 320x240 pixels.

The processing of the thermal images and recordings is done with the thermal analysis software **ResearchIR**. The software makes connection with the camera via an ethernet cable.

3.5.7 Thermometer [42]

Temperature plays a key role in the behavior of thermosensitive hydrogels, for this reason there needs to be a clear indication at which temperature the hydrogel is processed. Additionally the environmental temperature can be recorded.

The **Center 306 DATA LOGGER THERMOMETER** is used for this practice. It is a digital thermometer that functions with a thermocouple. The resolution is 0.1°C with an accuracy of 0.03°C + 0.01% of the reading provided that the probe is calibrated.

4 STUDY OF HYDROGEL MATERIAL

In this chapter different properties of hydrogel materials are studied. First the preparation method is clarified, then there will be further explanation of different measurement methods that have been applied. Moreover the idea is to gain information about how the material behaves in terms of rheology, density, but also visually and in relation to the temperature.

The main focus will lie on gelatin. Additionally a few properties of *Cellink start* will be tested as well, as this is a reference material that has favorable properties regarding printability. For the preparation of gelatin a standard protocol has been established. For experimenting 5 w/v%, 10 w/v%, 15 w/v% and 20 w/v% have been used. The separate protocols can be found in appendix B.1.

4.1 Hydroxyapatite nanopowder

Before commencing with the properties of gelatin and *Cellink start* a brief discussion on the use of hydroxyapatite nanopowder. As mentioned before in chapter 3.4.3, the idea was to augment the mechanical properties i.e. the yield strength.

The nanopowder is studied under the SEM. The samples are prepared by blowing or shaking the container to drop fine powder particles onto a carbon adhesive tab where the material sticks to. Then, as described in chapter 3.5.5, the samples are gold sputtered.

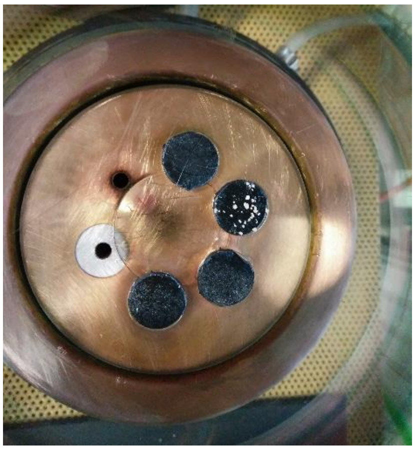

Figure 4.1-1 Prepared HA samples for SEM

The composition of the HA sample is attained from energy-dispersive X-ray spectroscopy (EDS), this is a feature of the SEM. The report can be found in appendix B.5. As expected the mineral is composed of Oxygen, Phosphorus and Calcium atoms. The carbon that is shown in the results is not a consequence of the HA, it is in fact the consequence of the carbon adhesive tab. Apart from carbon surfacing in the EDS report, there is no sign of hydrogen as would be expected. This is because a hydrogen atom has just one valence electron, the energy released after excitation lies too close to the valence electrons of other atoms, thus the signal of hydrogen alone cannot be distinguished.[43]

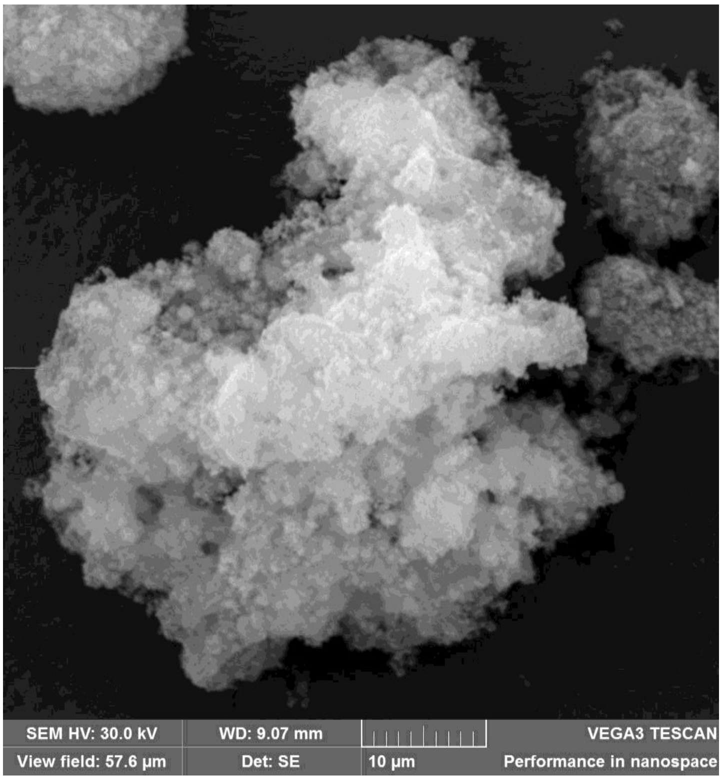

Figure 4.1-2 Hydroxyapatite nanopowder SEM image

Figure 4.1-2 shows a microscopic image of the HA under the SEM, unfortunately the magnification could not be further increased without losing a clear focus of the sample. Given that the particles are under 200 nm in size it is difficult to draw conclusion about the shape of the particles. However it is clear that the powder tends to forms agglomerates. This could make it challenging to manufacture a gelatin HA blend in combination with the insolubility of the powder in water.

There are a couple of approaches to try and disperse the HA powder in the gelatin. The first is working in an acidic environment as *Moreno e.a.* states, HA can go into solution to a certain degree as a function of the acidity.[40] A better approach however, is using a dispersant. There are various dispersants available. Additionally sonication is necessary to counter the problem of agglomerate forming. Unfortunately this requires a deeper understanding and research and is beyond the scope of this thesis, for this reason experimenting with HA is not handled.

4.2 Density measurements

When analyzing hydrogel material it is interesting to have an idea of the densities of the materials, the information is furthermore used when performing rheology tests. Knowing that the gelatin is manufactured in an aqueous environment is an indication of the density. The density is measured of 15 w/v% gelatin, three samples are tested. The *Cellink start* will not be tested as the sacrificial aspect of the material allows it to dissolve in water. Weighing the material in water is a key aspect of the measuring device.

The result of using the **Sartorius YDK03** is the following: (1.035 ± 0,003) g/cm^3

As expected the result approximates the density of water.

4.3 DSC tests [44], [45]

The DSC tests are taken with the Differential Scanning Calorimeter T.A. Instruments Q2000 as discussed in paragraph 3.5.1. Gelatin with a concentration of 10, 15 and 20 w/v% (see appendix B.1 for preparation method) is tested, 5 samples will be taken from each concentration. The objective is to find the sol-gel transition temperature of the gelatin samples. The samples are heated and cooled from 0°C to 90°C with a heating rate of 5 °C/min. The chosen inert atmosphere is Nitrogen.

The plot below shows the DSC curve of a singular sample of 15 w/v% gelatin. It is clear that there is a peak between 32 °C and 38 °C caused by an endothermic reaction when heating the samples. Expected was a peak between 25 °C and 35 °C, as stated in the literature study the gel-sol transition of gelatin takes place between these boundaries. However at first sight there seems to be no peak when cooling from 90°C to 0°C. By zooming in a slight slope becomes visible.

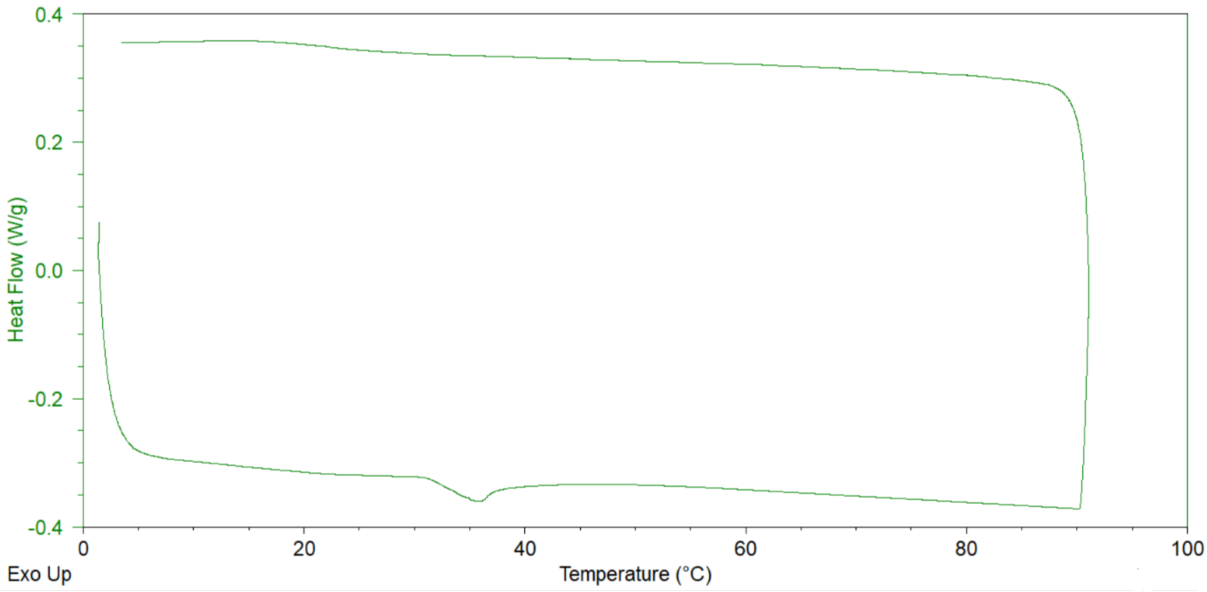

Figure 4.3-1 DSC test of 15 w/v% gelatin, heating and cooling curve between 0 °C and 90 °C

An **Integrate peak** is implemented, by selecting the boundaries of the peaks the maximum peak temperature, the area of the peak (in J/g) and the starting temperature of the sol-get transition process is calculated.

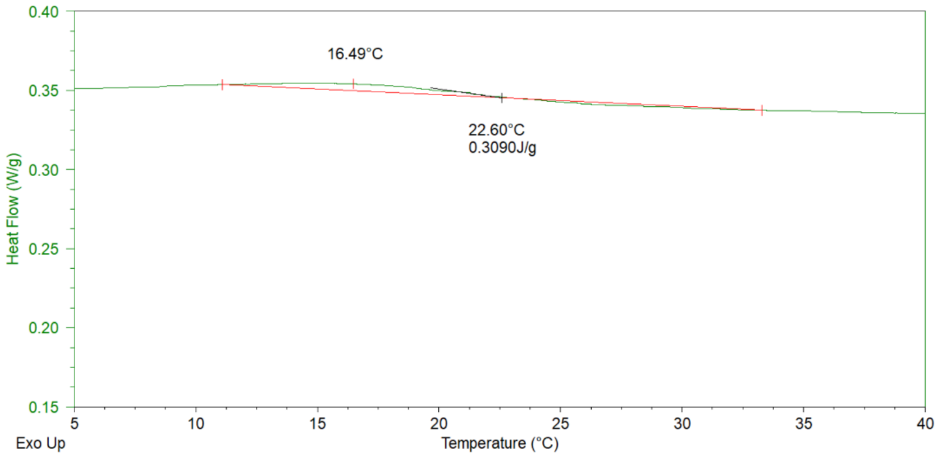

Figure 4.3-2 DSC test of 15 w/v% gelatin, integrated peak of the cooling curve

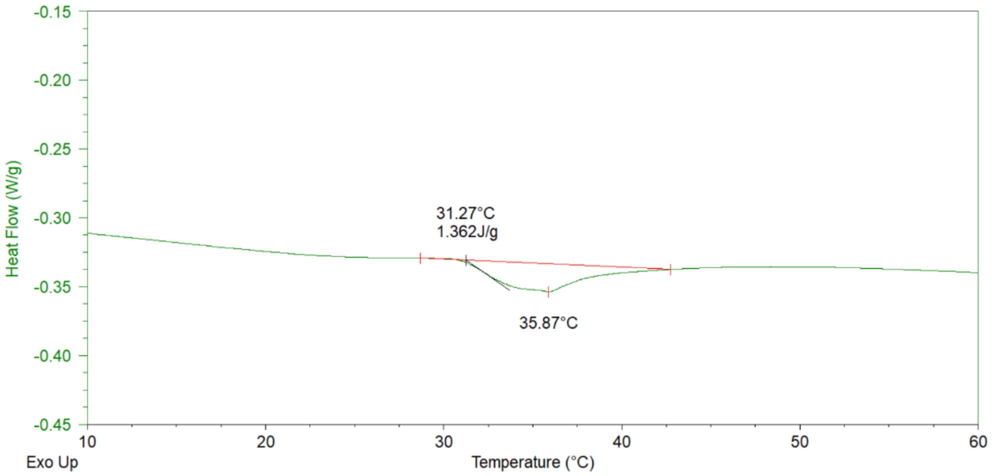

Figure 4.3-3 DSC test of 15 w/v% gelatin, integrated peak of the heating curve

The result above states that around 31.3 °C the transition process starts to take place with its peak at 35.9 °C in the case of heating the sample. During the cooling phase the peak occurs at a lower temperature, in this case 16.5 °C and a starting point at 22.6 °C. The results of the cooling peak are alarming.

An integrate peak is taken from all the samples (repeatability of 5), the average results are taken as well as the standard deviation. With the given accuracy the results are rounded to 0.1 °C. All the individual graphs as well as the data points can be found in the appendix B.3.

Table 4.3-1 DSC test results of the integrated peak for 10, 15 and 20 w/v% gelatin, with the average and standard deviation of the peak temperature, the starting temperature and the peak area as a function of the cooling and heating curve

		Cooling		Heating	
		average	deviation	average	deviation
10 w/v%	start (°C)	20.3	1	32.9	0.7
	peak (°C)	15.4	0.7	34.8	0.6
	peak area (J/g)	0.101	0,096	0,79	0.203
15 w/v%	start (°C)	23.9	0.8	33.3	1.8
	peak (°C)	17.2	0.9	36.4	1.2
	peak area (J/g)	0.568	0.355	1,626	0.46
20 w/v%	start (°C)	24.1	1.1	32.1	1
	peak (°C)	18.4	0.8	35.6	0.5
	peak area (J/g)	0.625	0.27	2.038	0.435

First of all the results seem to indicate that the peak temperatures have a standard deviation of under 1 °C (apart from one exception with a 1,2 °C deviation). This could indicate that the results do show information regarding the gelation point. It is also clear that the peak temperature slightly rises as the concentration increases with an exception of the heating phase between 15 w/v% and 20 w/v%. It was expected that the gelation temperature would increase with increasing concentration.

It can be argued that the peaks of the cooling curves are not outspoken enough to draw conclusions and the peak temperatures are far lower than expected (between 25 °C and 35 °C). However this could be a consequence of the cooling rate, namely 5 °C/min. To illustrate this an example from **T.A instruments** using the **Q2000** device is used to investigate the glass transition temperature of polypropylene. [44]

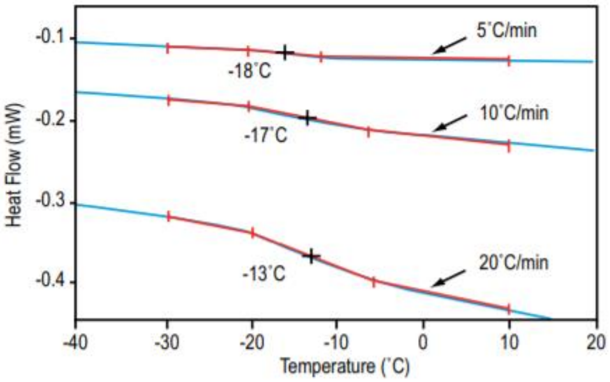

Figure 4.3-4 DSC curve polypropylene [44]

As the graph shows the glass transition temperatures is sensed at 5 °C/min, however the slope seems to progress gradually. In contradiction to the more steep slope when heating at 20

°C/min. Apart from having a more outspoken slope, the transition temperature has slightly shifted. A hypothesis is that changing the cooling speed in the case of gelatin, the peak might become more outspoken and might also shift to a higher temperature. To acquire a reliable gelation temperature more experimenting is required. However there is an alternative method to find this temperature or region which is more favorable to proceed with, namely a temperature sweep. This method is explained in the next chapter 4.4.

4.4 Rheology

Rheology is without a doubt the most interesting data regarding hydrogel properties. The data gives insight in the viscoelastic properties of the material as well as the whereabouts of the gelation temperature (range). The rheometer **MCR 501 Anton Paar** is used as a plate-pate rheometer and the silicon mold is used to shape the samples as described in chapter 3.5.3. All rheology tests (apart from the temperature sweep) are tested under the gelation point at 25 °C.

5 w/v% and 15 w/v% gelatin are used as well as the *Cellink start*. 15 w/v% concentration is selected as this will be the concentration used when printing. 5 w/v% gelatin on the other hand can be viewed as a base material for a gelatin blend, hence why this concentration is tested.

4.4.1 Flow curves

The starting point of the rheology was for this thesis trying to gain insight in the behavior of the biomaterial in terms of viscosity, shear stress and shear rate. Rotary measurements were performed to gather the data. This technique reveals the shear thinning properties of the hydrogels.

Samples of 5 w/v% and 15 w/v% gelatin were prepared and tested at 25 °C. Unfortunately the samples did not withstand the applied force and 'tore apart', which left the data distorted and no data of use was collected. However the issue was evaded, this is explained in the next chapter 4.4.2. The data can be consulted in appendix B.6.1.

4.4.2 Frequency sweep

As the data from the flow curves did not provide the necessary results, a different approach was implemented, namely performing a frequency sweep. This is a type of small deformation test, more specifically a small amplitude oscillatory shear (SAOS) test. Instead of having a rotary motion which was the case with the flow curves, there is a cyclic motion which overcomes the problem of the samples tearing apart. [46]

The boundary condition of a frequency sweep is that the experiments are performed within the linear viscoelastic range (LVE). This is to ensure that the results are independent of the applied stress magnitude. In practice an amplitude strain sweep is carried out once for each different concentration/material. The storage modulus (Pa) is plotted on the y-axis and the strain (%) is plotted on the x-axis, both presented on a log scale. The samples are tested at 10 rad/s. The deviation of the storage modulus should be within a selected tolerance range, in this case 10% of the maximum applied strain (0,05% for gelatin and 0,5% for *Cellink start*). The results and data can be found in attachment B.6.2. [46]

With a frequency sweep the storage and loss moduli can be plotted as a function of the angular frequency, when comparing the moduli it can be observed how solid or fluid-like the material behaves or (from another perspective more elastic or more viscous). These graphs and additional data are found in appendix B.6.2 for informative reasons, this will not be further discussed in detail.

The more relevant aspect of the frequency sweep for the sake of this thesis, is the complex viscosity (η*). This viscosity is based on the shear moduli, it is derived as followed.[47], [48]

The complex modus:

$$G^* = G' + iG" \qquad 4.4\text{-}1$$

The complex viscosity:

$$\eta^* = \frac{G^*}{i\omega} \qquad 4.4\text{-}2$$

$$|\eta^*| = \frac{|G^*|}{\omega} \qquad 4.4\text{-}3$$

With

η^* : complex viscosity

ω : angular velocity

The core value of this information revolves around the **Cox-Merz rule**, which is an empirical formula that states the following relationship between the dynamic and complex viscosity:

$$\eta(\dot{\gamma}) = |\eta^*(\omega)| \qquad 4.4\text{-}4$$

With η : viscosity

$\dot{\gamma}$: shear rate

There is a one to one relationship between the viscosity as a function of shear strain and the complex viscosity as a function of the angular frequency, meaning through this method similar data to that of the flow curves can be attained.

The results are shown for the different concentrations/materials. The data is presented on a logarithmic scale, the slope indicates that there is indeed shear thinning behavior. All samples show shear thinning properties. Furthermore it shows that the gelatin 5 w/v% behaves, as far as the rheology shows, like the *Cellink start* material. Knowing that the *Cellink* start has suitable printing properties it would seems that it is the same case with 5 w/v% gelatin. However this does not mean that 15 w/v% has not got suitable properties for printing, as mentioned in chapter 3.3 the viscosity working range of the *Inkredibe+* is between 0.001 and 250 Pa.s. Unfortunately we do not know the exact shear stress applied on the hydrogel during printing, so this range cannot be specified with the acquired data.

Because of these results it might be tempting to focus on gelatin 5w/v% as it has suitable printing properties. However *Cellink start* is a material that dissolves in aqueous environments as this is a sacrificial material and through experimenting with this material it is clear that the material deteriorates in time after printing has been done. When looking at G' and G" 5 w/v% gelatin shows more fluid like behavior than 15 w/v% gelatin as was expected, but this also means that mechanical properties (i.e. stiffness) are less favorable. There is a possibility that the more aqueous 5 w/v% gelatin tends to behave more like the sacrificial material in terms of deterioration, this is not further examined.

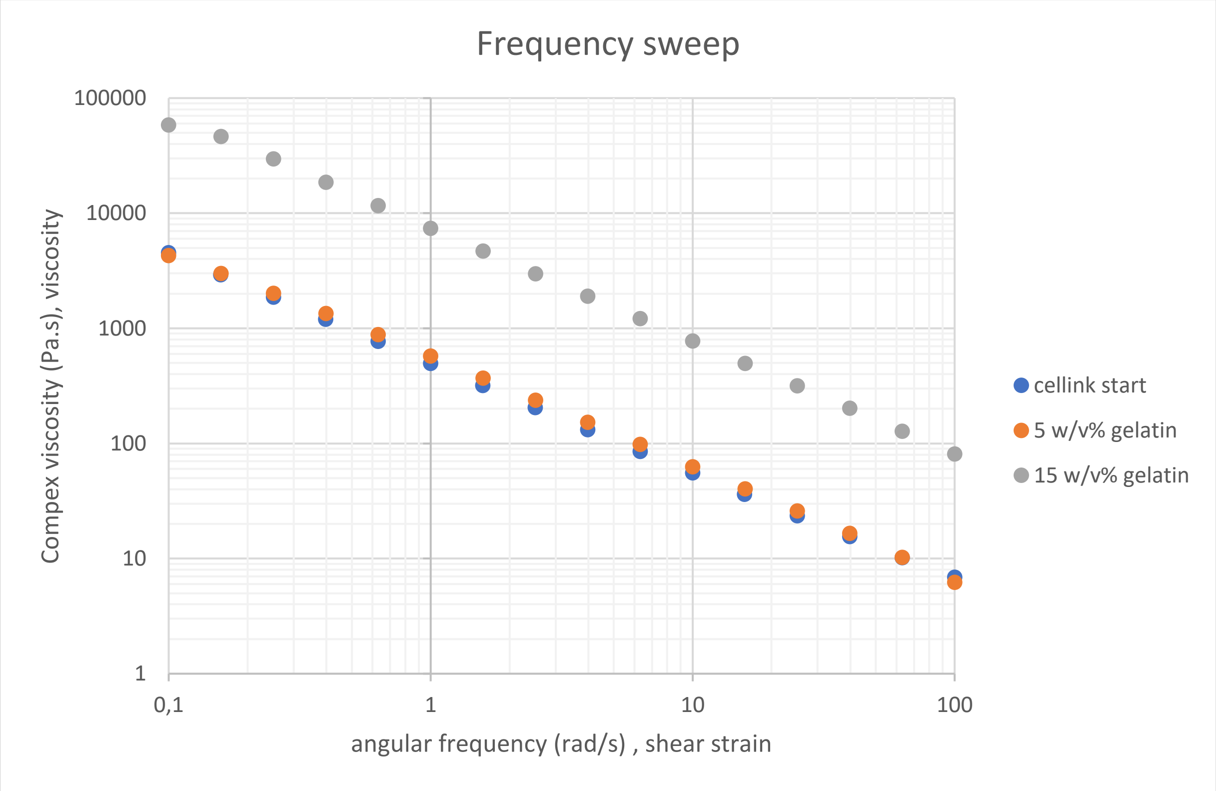

Figure 4.4-1 Frequency sweep curves Cellink start, 5 w/v%, 15 w/v% gelatin at 25 °C. Complex viscosity (Pa.s) plotted as a function of the angular frequency (rad/s). Viscosity and shear strain are labelled to emphasis the Cox-Merz rule

The next step is relating the data to the **power Law**. As defined a Newtonian fluid has the following relation between the viscosity, shear rate and shear stress:

$$\tau = \eta \dot{\gamma} \qquad 4.4\text{-}5$$

When a material is non-Newtonian, the power law can be implemented as an empirical formula to express the relation between the shear rate, shear stress and viscosity. Note that this formula does not bring any time dependency in account.[47], [49]

$$\eta = K\,\dot{\gamma}^{n-1} \qquad 4.4\text{-}6$$

$$\tau = K\,\dot{\gamma}^{n} \qquad 4.4\text{-}7$$

With n : parameter power law

K : parameter power law

By simply taking $\dot{\gamma}$ =1 in equation 4.4-7 K can be calculated. Once K is known, the equation can be solved for n. When calculating n, the average of the data is used. Moreover both the parameter n is dimensionless whereas K has the dimension Pa.s^n. The tests are repeated three times. There is no standard deviation available for 5 w/v% gelatin since one run was available for this concentration. The results are:

Table 4.4-1 Calculated average parameters K and n of the power law, with standard deviation

	5 w/v% gelatin	15 w/v% gelatin	Cellink start
K (Pa.s^n)	572	7356 ± 216	493 ± 6
n (-)	0.05 ± 0.03	0.02 ± 0.02	0.05 ± 0.01

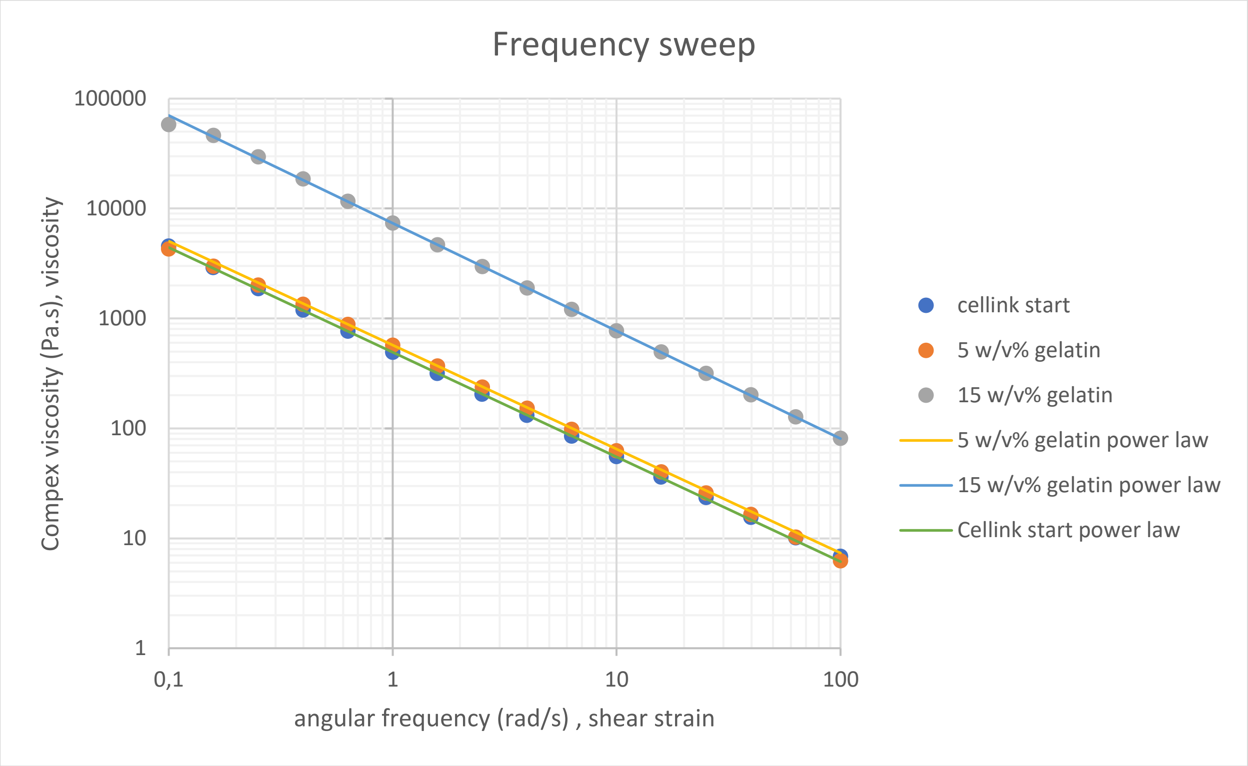

Figure 4.4-2 Frequency sweep curves Cellink start, 5 w/v%, 15 w/v% gelatin at 25 °C with plotted calculated power law models

The power law curves are plotted along with the previously discussed data points. It is pleasing to see that the curves approach the data points. On a side note, the power law curve is only valid when shear thinning is present in the samples.

4.4.3 Temperature sweep

As mentioned in chapter 4.3, an alternative method is used to pinpoint the whereabouts of the sol gel-transition of gelatin. Since actual printing will be done with 15 w/v% gelatin, this concentration will be implemented. Furthermore the samples are heated to 40 °C and then cooled down to 20 °C. The data represents exclusive the cooling curves as these are of importance during the printing process. Again, similar to the frequency sweep, the temperature sweep is a SOAS and works within the LVE, in this case 0,5 % strain. Additionally the tests are performed at a frequency of 10 rad/s and a temperature drop of 1 °C/min. There is a repeatability of 5 samples.

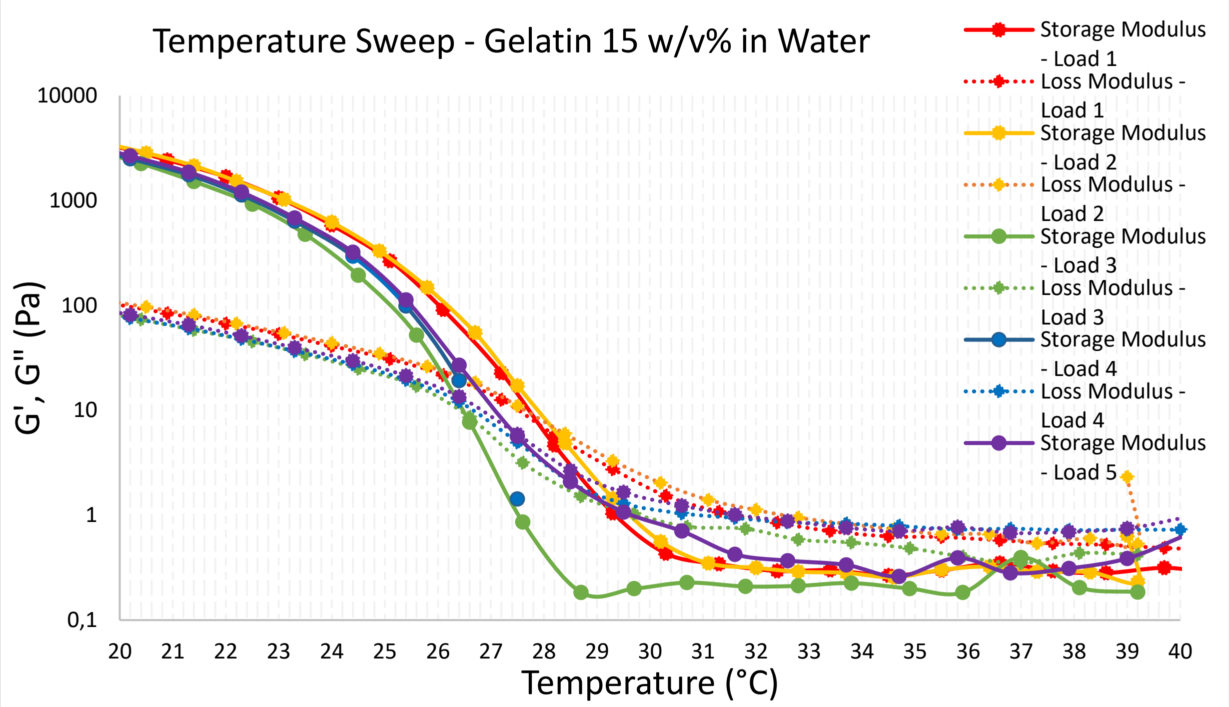

Figure 4.4-3 Temperature sweep 15 w/v% gelatin performed at 10 rad/s between 20 °C and 40 °C with a temperature drop of 1 °C/min. G' and G" (Pa) are plotted as a function of the temperature (°C), 5 samples are tested

The point where G' and G" intersect is the sol-gel transition temperature. Above this temperature G" surpasses G' in value and the gelatin behaves more fluidlike. For this reason the data beyond this point seems to be uncontrolled. The sol-gel transition is in fact more of a region than one specific point, this could partially explain the slightly different intersection points between G' and G" for different samples. Additionally there are different factors that influence the gelation point, *Osorio e.a.* stated that the concentration, the pH value and the bloom degree have a significant effect on the gelation temperature.[50]

The average gelation temperature is calculated. The recorded datapoint that approximates the gelation temperature the closest for each sample is used as a reference temperature.

$T_{gelation} = (27.4 \pm 0.9)\ °C$

From the calculations 27.4 °C is the average transition temperature, taking into account the standard deviation this seems an acceptable result. Furthermore from experience with gelatin this is a very realistic outcome.

4.5 Microscopy

Microscopic tests are taken with the **Digital microscope Hirox KH-8700** as discussed in paragraph 3.5.2. Gelatin of 10, 15 and 20 w/v% is liquified at 60°C. With a micropipette (of 2/20 microliter) samples of the gelatin with different concentration are brought on to a microscope glass slide and are covered with a circular coverslip. The images are shown in appendix B.4.

The results give a first impression of the magnified gelatin structure. This might be more relevant for comparison in future work when different gelatin blends are used.

4.6 Conclusion

The most vital conclusion is that all the tested biomaterials show shear thinning properties within the given ranges of shear stress and shear strain. As discussed in the literature study this was of great importance for cell viability. The second aspect that was thoroughly examined was the gelation temperature, even though the DSC tests did not provided the desired results, the temperature sweep did. The results showed that for 15 w/v% gelatin the gelation temperature is (27,4 ± 0,9) °C, this is interesting background information for the experimenting phase. Moreover density measurements were taken of 15 w/v% gelatin, as expected the results approximated the density of water.

A more unfortunate conclusion is that the implementation of hydroxyapatite is more complex as first foreseen. Therefore it will not be implemented due to the limited time available.

5 PROCESS ANALYZING AND DEVELOPMENT

In this chapter the functioning of the **Inkredible+** as well as the whole printing process is analyzed. Based on the outcome, if needed and where it’s feasible, improvements are made. First the functioning of the cartridges and heating element are examined and improved if needed. Secondly the bioprinter did not possess a cooling function for the print bed which is required for thermal crosslinking. For this reason a cooling platform is manufactured and analyzed.

5.1 Analyzing Cellink cartridges

From experience, the *Cellink* cartridges seem to have a couple of limitations. Mainly this concerns the sealing of the biomaterial from the ambient air. What tends to happen is that air escapes through the piston on top of the material inside the syringe. When pressure is applied the air is in fact pushing down the material and not the piston itself. A bigger issue is that in some cases the vacuum at the bottom of the syringe is lost and the material (if this is more fluidlike) pours out. Additionally it doesn’t seem like the product is sold as disposable in the sense that it is only used once.

Figure 5.1-1 Left, Cellink piston model. Right, B.Braun piston model [51], [52]

For these reasons new 3 ml syringes are bought from **B. Braun** that have a rubber piston and presumably better sealing. By looking at the two different piston types in Figure 5.1-1, it is clear that the piston used for the *Cellink* cartridges has a more streamlined design. Additionally, it appears that the alignment of the piston with the cartridge is well implemented. Moreover the contact between the piston and the *Cellink* cartridge is presumably kept at a minimum to minimize the required friction force. However this could be the reason for poor sealing. There could be a trade-of between the two advantages. The *B.Braun* piston is a rubber piston and has a larger contact surface with the cartridge, so it could be that higher friction forces are needed. This further investigated.

Both cartridges are air-filled and pressure is slowly applied starting from 0 kPa up to the point where the piston moves completely down. This is done to gain understanding of what pressure needs to be applied to overcome the static friction. The results are, with the experiment repeated three times:

Cellink: 21± 2 kPa

B.Braun: 30 ± 3 kPa

As expected the *Cellink* piston requires less pressure for movement to be induced, however an average difference of 9 kPa is not alarming. At higher pressures there seemed to be a pressure loss in the sense that air escaped from the connection between the pressure supply and the **B. Braun** cartridges, to solve this problem plumbers grease was applied where pressure is lost. To illustrate how the pistons function at a slightly higher pressure, *Cellink start* material is used (because this is more predictable in behavior than gelatin) and pressure is applied until droplet formation occurs or any material is pushed out. The experiment is carried out at an ambient temperature of 23 °C and is repeated three times.

Cellink:	42 ± 5 kPa
B.Braun:	58 ± 2 kPa

Again motion in the piston is induced at higher pressure in the case of the *B.braun* cartridge. One last experiment is carried out to have an idea of what effect this difference has on the width of a printed track with a certain applied pressure. Again *Cellink start* is used, the remaining parameters are, an applied pressure of 60 kPa, an nozzle diameter 0.25 mm and printing speeds of 10,15 and 20 mm/s. For more information regarding the printing of tracks, the measuring method and measurements themselves as well as the chosen parameters chapter 6.3– 6.5 can be consulted.

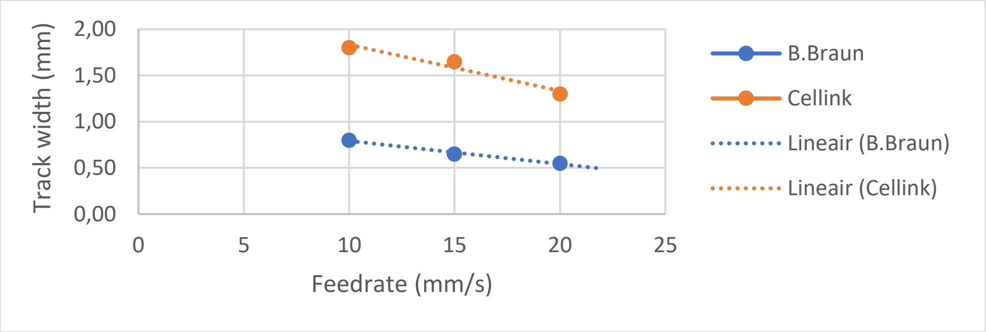

Figure 5.1-2 Track width (mm) as a function of the printing speed (mm/s) for the Cellink and B.Braun cartridges. Three samples are measured

As expected the track width with the same applied pressure is wider for the *Cellink* syringe and as the results show there can approximately be a difference of ~ 1 mm. Do note that during these experiments the piston of the *Cellink* cartridge was stuck in its position and it was in fact the air pushing down the material.

5.2 Analyzing heating element

As mentioned before both printheads of the bioprinter feature a heating element. In order to gain a better understanding of their functioning and most importantly if the material inside the syringe is heated homogeneously, the **FLIR A300** thermal camera is used. The approach is the following.

15 w/v% gelatin is manufactured as biomaterial and syringes, both the **Cellink** and **B.Braun**, are filled beforehand. Calibration of the thermal camera is based on the thermal sensors from

the Inkredible+ itself in combination with the reading of the thermocouple. This means that at room temperature, in this case 25°C, the emissivity of the **ResearchIR** software is adjusted until the interpretation of the room temperature of the software is the same as that of the thermal sensors, in this case (0.99).

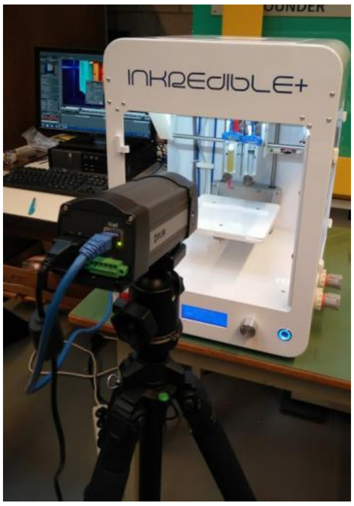

Figure 5.2-1 set up thermal camera

A worst case scenario is implemented, meaning the gelatin is kept at room temperature and all heating is done by the heating elements. The gelatin is heated up to 30°C because during the experimenting phase the temperature will not exceed this threshold.

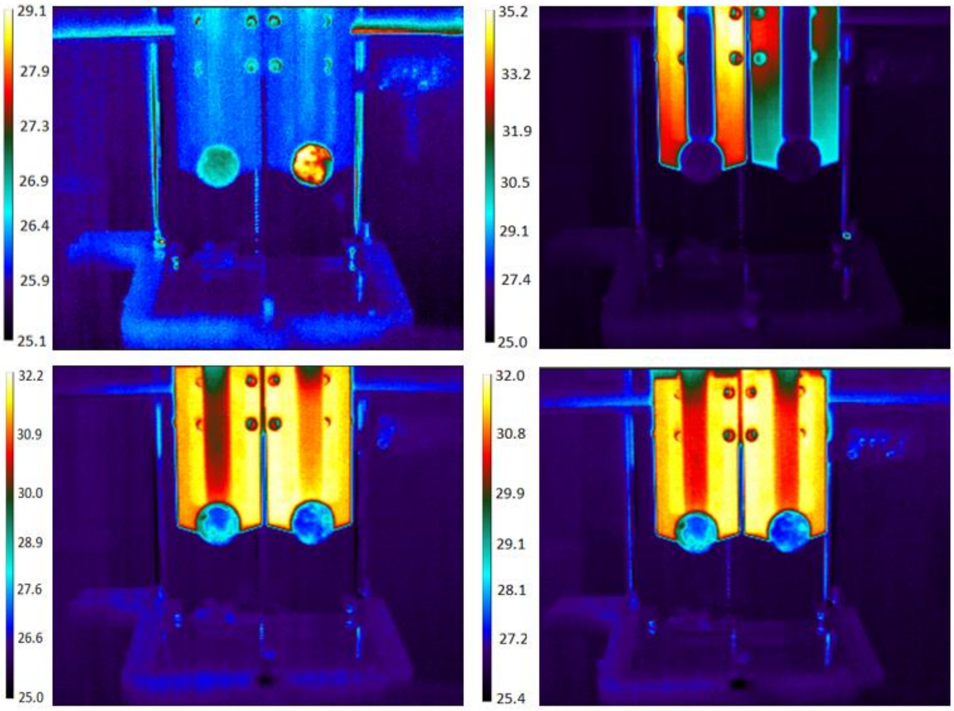

Figure 5.2-2 From top to bottom, left to right, different heating phases of the material and heating elements. Cellink cartridge on the right, B.Braun cartridge on the left. The whole process takes roughly 15min (legend in °C)

The starting point of heating process in Figure 5.2-2 is at the top left corner and works towards the bottom left corner. The results indicate that the heating elements are capable of successfully heating the gelatin (starting from ambient temperature) and do so within acceptable limits to call the outcome a homogeneous temperature distribution. Also, there is no visible significant difference between the heating of two syringe types, despite the fact that *the B.Braun* cartridges are slightly smaller in dimensions.

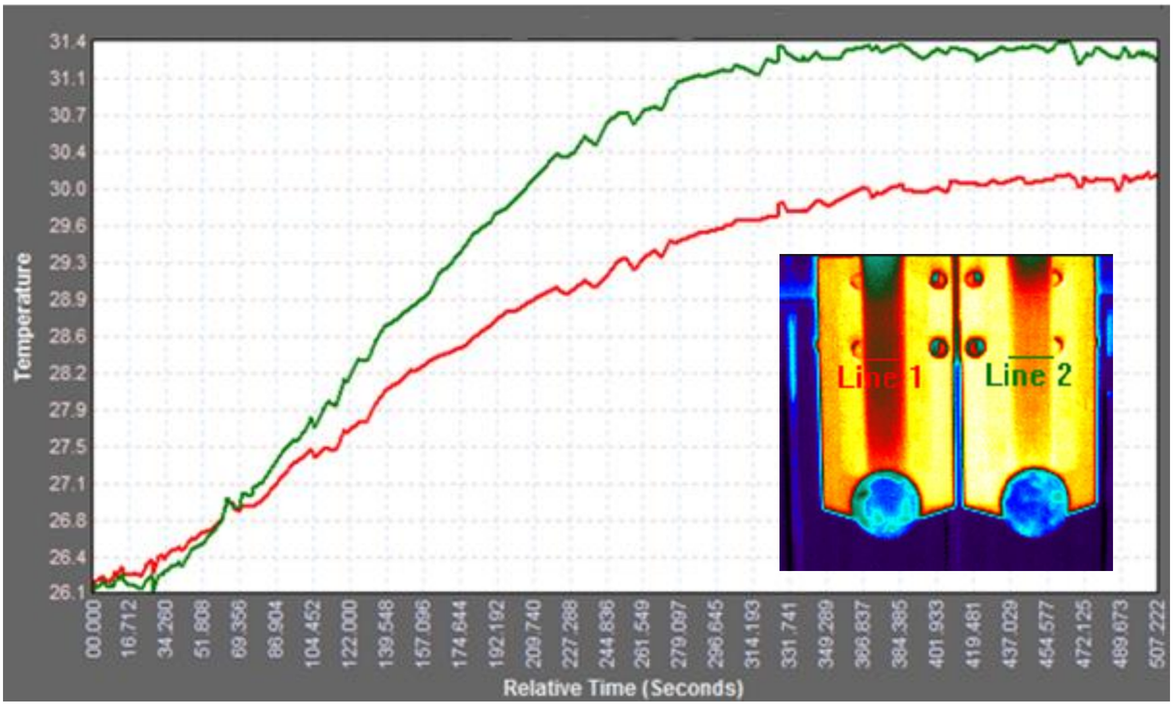

Figure 5.2-3 Temperature (°C) measured as a function of time (s). The data is an average over the corresponding colored line.

The course of the heating process is recorded over a time of about nine minutes as shown in Figure 5.2-3. Unfortunately this does not include the stabilizing phase of the material temperature, however it reveals the functioning of the heating elements. The measured temperatures are an average of the respective colored lines drawn on the cartridges. On a sidenote the left cartridge was turned on about 10 seconds sooner. *Line 2* seems to makes a slight overshoot when working towards the setpoint of 30°C, this can also be viewed in Figure 5.2-2 where the temperature drops once again in the last phase. Because the calibration done is not precise enough, as this is a difficult procedure, and the emisivity of the cartridges and aluminum heaters differ, there can be no definite conclusion drawn regarding the absolute temperatures.

5.3 Design and manufacturing of a cooling platform

When printing hydrogel material there is a lack of stability. To partially overcome this problem thermal crosslinking is applied, the Van der Waals forces and hydrogen bonds then induce stability in the biomaterial. The concept is to manufacture a cooling platform for the printbed to induce thermal crosslinking during printing of thermosensitive hydrogels.

The principle of the design is based on a Peltier element, also referred to as a thermoelectric cooler. When a current is send through the element it introduces a temperature difference between its upper and lower surface. One side will heat up while the other side cools down. What the exact achieved cooling temperature is, depends on the specification of the Peltier element, the applied current and ambient temperature. The idea is to use the cold side of the element to cool the platform. The controlling of the temperature itself is done with a microcontroller with feedback provided by a thermal sensor. The objective temperature of the cooling platform is 10°C with respect to the room temperature (21 °C). Nevertheless a cold environment is not ideal for cells which have a threshold temperature for survival of about 4 °C. For this reason the platform is not cooled beyond the chosen 10 °C.

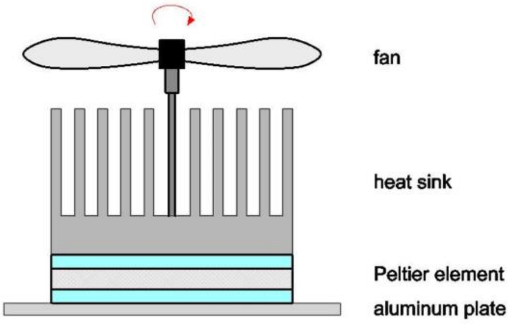

Figure 5.3-1 Design cooling platform

The basic of the design as shown in Figure 5.3-1 consists of the thermoelectric cooler, a heatsink with ventilation (to cool down the hot side of the element as well as the dissipated heat from the electrical circuit) and a platform. Aluminum is chosen as the platform material because of its high conductivity. The chosen printing surface is 8 x 8 cm, this is smaller than the original surface of the printer platform. This is done so in order to decrease the amount of energy that needs to be extracted from the platform for cooling.

The most important step is selecting an appropriate Peltier element, this is the starting point of the design. The reason being that the outcome gives an idea of how much cooling can be done and what type of heatsink is necessary.

5.3.1 Selecting Peltier element and heatsink [53]

In order to select a suitable Peltier element, thermal calculations are required to estimate the heat that needs to be pumped from the aluminum plate (Q_{total}), this information is provided by the datasheet of such an element. The thermal calculations that lead to Q_{total} can be found in attachment C.2.1. With a total safety margin of 20% results are given as a function of (a possible) cooling time:

5min: $Q_{total} = 3.7$ W

2min: $Q_{total} = 7.9$ W

1min: Q_{total} = 14.9 W

There are different factors that need to be taken into account apart from the desired cooling temperature setpoint. For one the cooling time that is needed to reach the setpoint. In this case this is of less importance, in other words a cooling time of about five minutes is not dramatic for the application and thus the required power to cool can be suppressed. Another variable that plays a key role is the absolute thermal resistance (R_{th}) that is required from the heatsink expressed in °C/W. The heatsink must be able to drain excess heat away to stop the Peltier element from overheating. So there is a tradeoff between what cooling power is desired and how much heat can be dissipated by the heatsink.

Peltier elements are rated by their coefficient of performance (COP), the ratio between the amount of heat pumped by the Peltier element and the supplied electrical power. The previously calculated Q_{tot}, is the heat that is pumped by the Peltier element in order to cool the platform, also referred to as Q_c. The total heat dissipated by the Peltier element is Q_h, this is the sum of Q_c and the electrical power used by the thermoelectric cooler. Normally such element works optimal when 70% of its maximum current is used. These specifications are presented with the following formulas:

$$\mathrm{P} = \mathrm{UI} \tag{5.3-1}$$

$$\mathrm{COP} = \frac{\mathrm{Q_c}}{\mathrm{P}}\,100\% \tag{5.3-2}$$

$$\mathrm{Q_h} = \mathrm{Q_c} + \mathrm{P} \tag{5.3-3}$$

$$\mathrm{R_{th}} = \frac{\Delta \mathrm{T_{HS}}}{\mathrm{Q_h}} \tag{5.3-4}$$

With P : the electrical power pumped into the Peltier element

U : the applied voltage

I : the applied current

COP : coefficient of performance

Q_c : Cooling power of the Peltier element

Q_h : total dissipated power by the Peltier element

R_{th} : thermal resistance of the heatsink

ΔT_{HS} : temperature difference between the heatsink and the environment

Based on this information the Peltier element is selected. The chosen thermoelectric cooler is a 3A Peltier element, model **CP30238** with a temperature of 50 °C on the hot side of the element, specifications can be found in appendix C.3. Suppose the element is pumping 6W of heat, then the following characteristics are stated assuming the ambient temperature is 25 °C.

Q_c = 6W

P = 14.7 W

COP = 41 %

Q_h = 20.7 W

R_{th} = 1.2 °C/W

The efficiency of the element is quite low, however this is not abnormal for a Peltier element and doesn't fall out of the ordinary. Furthermore The absolute thermal resistance, R_{th} is strict. Cooling with natural convection will not be sufficient enough, for this reason a fan necessary. The heatsink and fan used in this application is an **Intel D60188-001**, which is in general used for cooling the CPU in a computer. It is powered by 12 V, 0.6 A and has an RPM from 1500 to 2800. The device has a thermal resistance of 0.35 °C/W.[54]

5.3.2 Electrical circuit

As mentioned before the cooling process is controlled and this is done with a microcontroller. In this case an **Arduino nano** is used as a PID-controller. The schematic layout of the controller is presented in Figure 5.3-2.

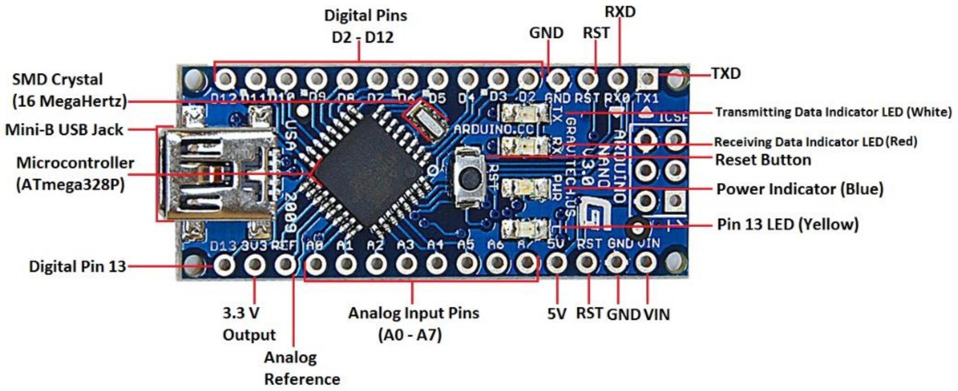

Figure 5.3-2 Schematic overview of the Arduino nano [55]

The key purpose of the *Arduino* is to use PWM signals (digital pins on the circuit board) between 0 V and 5 V to control the current flowing through the Peltier element. The circuit is powered by a DC 12 V, 24 A power supply (this same power supply is used to power the fan of the heatsink).

The main electrical circuit has two transistors in a cascade formation, called a NPN Darlington transistor. Depending on the PWM signal a current is drawn at the base of the transistor which allows a maximum of 3 A to flow through the thermoelectric cooler (this is in combination with 8 V over the element). The components are chosen with respect to this maximum threshold. The second NPN transistor is responsible for keeping the desired current stable. Knowing that there is a voltage drop (of around 0.7 V) from the base to the emitter of the transistors, the resistor values are deducted, this is 560 Ω and 0.22 Ω. Furthermore the signal send by the *Arduino* is at 500 Hz, this is not ideal for a cooling application, a smoothed signal would be advised. To partially solve this problem a capacitor is used to function as a low pass filter. With a capacitor of 20 μF the cutoff frequency is calculated as followed.

$$f_c = \frac{1}{2\pi RC} \tag{5.3-5}$$

With f_c : the cutoff frequency

R: the resistance

C: the capacity

The cutoff frequency is in this case approximately 14 Hz.

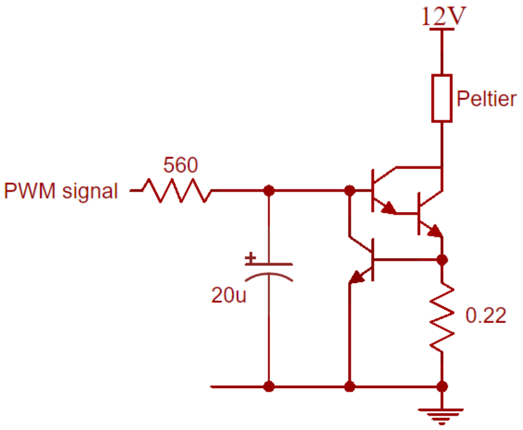

Figure 5.3-3 Electric scheme for cooling the Peltier element with PWM

For information on the exact used components, appendix C.2.3 can be consulted.

5.3.3 Thermal sensor [52]

For the PID-controller to work, feedback is required, this is done by a thermal sensor. The LM35 sensor is used, with an accuracy of 0.5 °C at 25 °C. The sensor has three pins connected to the ground, 5V of the *Arduino* and an analog input pin.

To make the usage of the cooling system more convenient, without the need for connection with a computer, an LCD screen is implemented. This projects the real-time temperature measured by the sensor.

5.3.4 Software

As mentioned before the *Arduino* is implemented as a PID controller. This is done by importing a library, **PID_v1.h**, that already has a build-in PID function. This makes it quite simple to implement. As cooling is a process that does not show instant changes it is opted to only of the proportional control. Additionally the temperature setpoint is slightly adjusted from the 10 °C because the thermal sensor is attached near the edge of the printbed. How the temperature is distributed is discussed more in detail in chapter 5.4. The full program can be consulted in the appendix C.2.4.

5.3.5 Manufacturing and implementing cooling system

The Peltier element is attached with thermal glue to the heatsink on one side and to the aluminum plate on the other side. For implementation in the *Inkredible+* a case is 3D printed and with bolts and screws the construction is tightly held in place. The technical drawing of the printed case can be found in attachment C.4.

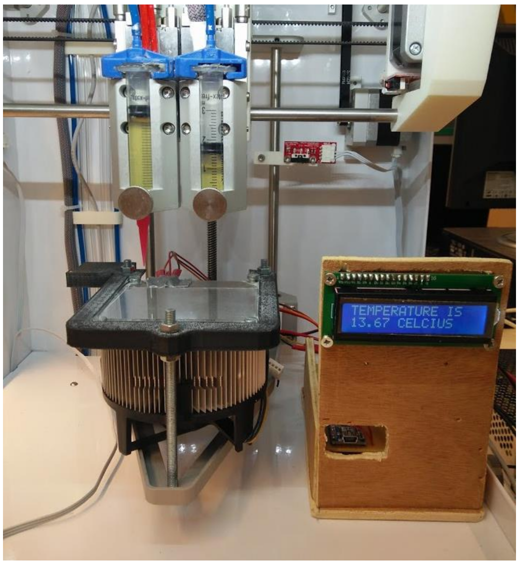

Figure 5.3-4 The cooling system implemented in the Inkredible+

5.4 Analyzing cooling platform

When testing the limits of the cooling bed and performing measurements with the thermal sensor, it is found that the system has the capability to cool down at least 12 °C from ambient temperature.

Further analyzing of the cooling platform is done with the *FLIR* thermal camera. As explained before the calibration is done by adjusting the emissivity in the software to match the measured environmental temperature. In this case environment is measured by the thermal sensor, the emissivity is set to 0.91. The ambient temperature was between 18 °C and 19 °C at the time the measurements were taken. However there was an additional problem, the temperature readings of the aluminum was distorted once the cooling process was started. The cause was presumably thermal reflection. *Helling Reiniger U 87* Spray is used to function as a coating to counter the problem. When the coating was applied the temperature differences in the readings of the camera were compliance with the readings from the sensor.

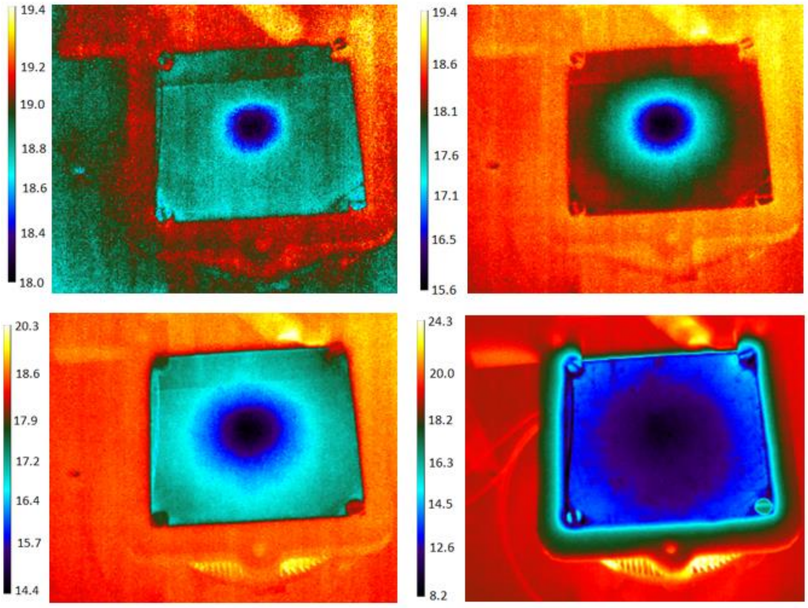

Figure 5.4-1 From left to right, bottom to top four different phases of the cooling platform. The last phase is operation at the setpoint. (legend in °C)

With a setpoint of 10 °C the whole cooling down process took about 2 min 30 sec, which is certainly an acceptable timing. As explained before no conclusions can be drawn from the absolute temperature, however the temperature difference can be taken as a more reliable source of information. The temperature gradient is illustrated in Figure 5.4-2, by measuring the temperature difference between the center and outer corner along the profile line. There is a temperature drop of around three degrees. This should give a general understanding of how the cooling system functions and to what boundaries it can be pushed in terms of cooling.

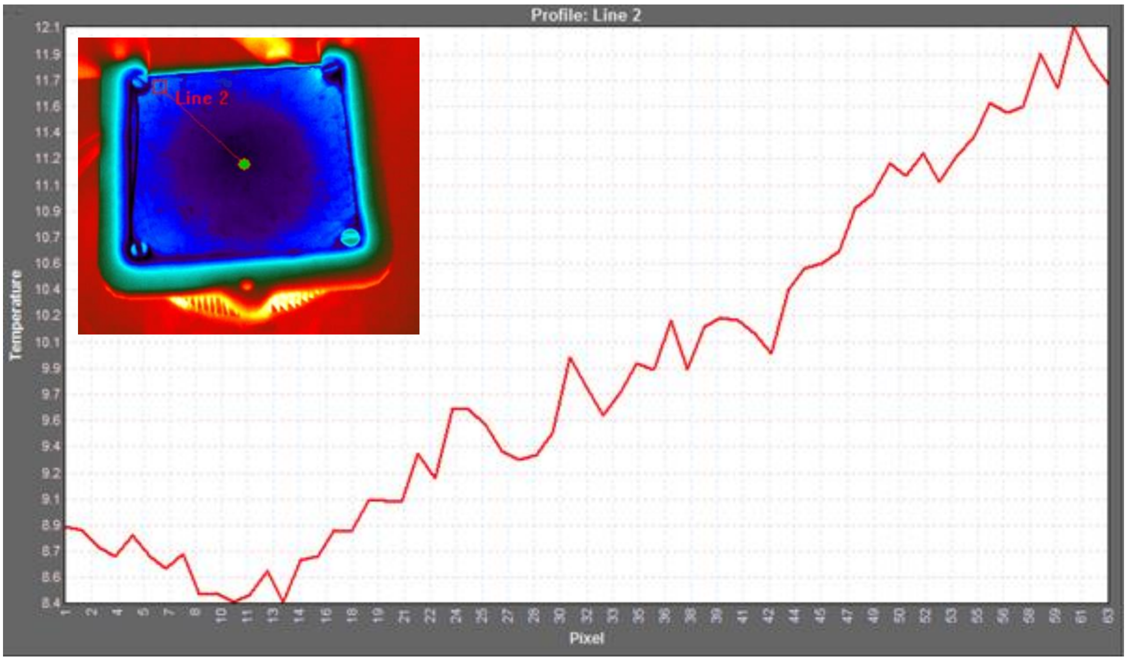

Figure 5.4-2 Temperature of the cooling platform (°C) as a function of the distance from the center along the red line.

Another approach is to measure the track width of gelatin printed with and without the functioning of the cooling plate. The idea is to indicate that that there is less diffusion of the gelatin due to thermal crosslinking. Unfortunately as explained in chapter 6.6, the gelatin printing process is not enough under control to rely on the results, so this is more as an illustration. Why the process is not under control and how measurements are taken is explained in chapter 6.6 as well. Printing is done with the following conditions.

- Ambient temperature: ± 25 °C
- Gelatin concentration: 15 w/v%
- Gelatin temperature: 28 °C
- Feed rate: 20 mm/s
- Printing pressure: 70 kPa

The results are:

With cooling of the bed: (1 ± 0,3) mm

Without cooling bed: (1,35 ± 0,3) mm

The results could possibly be an indication of what effect thermal crosslinking has, however as mentioned the data cannot be seen as consistent results.

5.5 Conclusion

In this chapter the printing process was analyzed where necessary. First a comparison was made between the original cartridges and new implemented cartridges. Even though the *Cellink* syringe does provide some advantages in the sense that it excels in minimaxing friction force and presumably in linear alignment with the cartridge, it does not way up against the consequences of poor sealing around the piston. For this reason, unless mentioned otherwise, the B. Braun syringes are used during the experimenting phase. Secondly the heating elements of the 3D printer were analyzed. The main conclusion from the results is that the material (gelatin) seems to heat op homogeneously, which is ideal for printing at a certain temperature.

Unfortunately the 3D bioprinter is not equipped with a cooling platform for thermal crosslinking. A cooling bed was manufactured based on the principles of a Peltier element. The results indicated that the platform has a cooling capacity of at least 12 °C with reference to the ambient temperature and does so in under 3 min. Furthermore the temperature difference between the center of the platform and the most outer edge is about 3 °C. This is a favorable result.

6 MATERIAL PRINTING EXPERIMENTS

6.1 Workflow

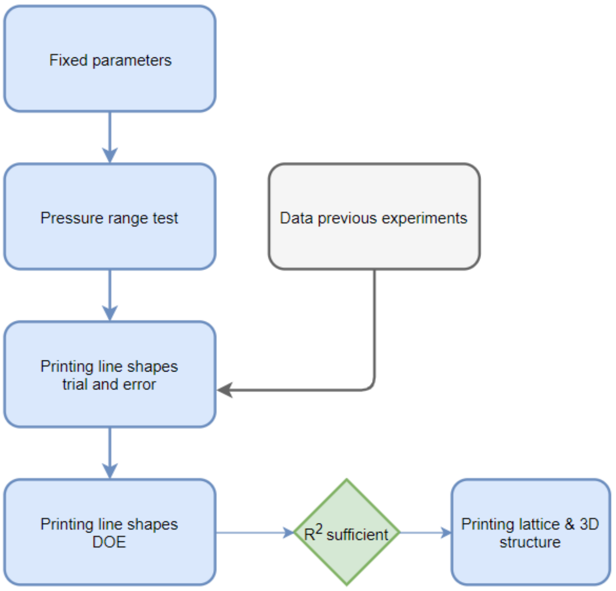

Figure 6.1-1 Flowchart experiments

The experiments carried out follow a certain workflow as shown in Figure 6.1-1. The first step is selecting the fixed parameters. This includes the biomaterial (as well as their concentration), printing temperature and layer height. Note that these parameters could possibly be selected as variables, however this would augment the complexity of the printing process and are therefore chosen to be fixed. The variable parameters in this study are the feed rate, applied pressure and nozzle diameter. Separate experiments are conducted for conical and blunt nozzles. Once the parameters are set the experimenting can commence.

First a pressure ranging tests is taken. Here the pressure is increased starting from 0 kPa up to where jetting or another phenomenon occurs. The threshold values of droplet formation and jetting are of greatest importance, as pressure should not be applied outside these boundaries.

Once the idea of a pressure range is established the trial and error phase starts. Information gained from the pressure range test and possibly previous experimenting are used as inputs. This phase is about experimenting with different pressures, feed rate and possibly switching between nozzle diameters. This is done by printing a predefined track which is validated visually by the consistency of the track in terms of line and corner formation. Based on the findings the levels of the three factors (nozzle, printing speed, pressure) are chosen as input for a design of experiments (DOE), in this case a full factorial design.

If the process is under control within acceptable limits, this can be derived from the DOE outcome as well as visual observation, the next step can be put into action. Desirable printing parameters are chosen and lattice structures as well as 3D printed structures are printed and evaluated.

6.2 Calibration

Before commencing with printing, attention needs to be paid to the calibration process. Sadly, the *Incredible*+ only possesses a homing function and no automatic x and y -axis calibration is provided. Therefore this is done manually by using a spirit level. Furthermore the z-axis is manually calibrated as well. This is done with an old-fashion technique, namely with a piece of paper. This method is not recommended when using actual bioink with cells incorporated as this is not a clean technique, however it does provide a temporary solution. Figure 6.2-1 shows the difference between a calibrated print carried out with the paper technique and one carried out visually. It is clear that calibration has a huge impact on the outcome. When calibrating manually the distance from the printbed to the nozzle is presumably higher, the consequence is that the material does not bond properly to the printbed.

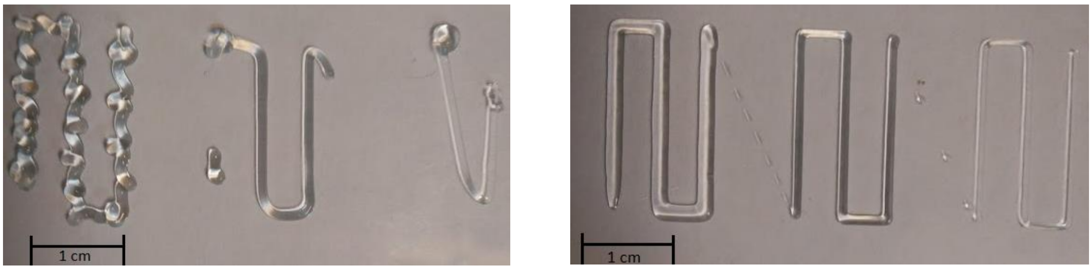

Figure 6.2-1 Left visual calibration, right with a piece of paper. Printed with Cellink start at 60 kPa, 0.25 G conical nozzle and respectively 2, 5 and 10 mm/s

The layer height can be adjusted in the software itself, as a standard 0.4 mm is taken. Normally this is set to approximately the nozzle diameter, however the experiments are conducted with different nozzle types and since the value is chosen to be a fixed parameter this is not alarming.

6.3 Printing geometries

Since this is the first encounter with this bioprinter, small steps are taken towards the printing of a structure. The main focus lies on printing of tracks. Angles are printed as well as this is a good reference of the consistency of the printed pattern.

The initial starting material for printing is *Cellink start*. During each print three replicas are printed. Each in consisting of three, 2 cm long, tracks and four 90° angle corners. The tracks are 0.5 cm apart from each other to avoid any overlap between two tracks to attain a clear image of an individual track.

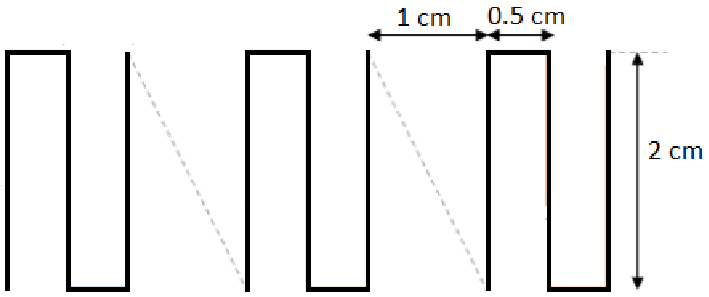

Figure 6.3-1 Three samples with each track alternating between 2 cm and 0.5 cm with a 90 ° angle transition. 1 cm spacing is left between samples

Gelatin is printed on the manufactured cooling platform. As discussed in chapter 5.4 there is a temperature gradient along the platform with the minimum temperature around the center of the platform. For this reason just one pattern is printed at a time near the center of the printbed. Additionally as gelatin has a more unpredictable behavior than *Cellink start* a run-up track (dashed line) is provided of 2 cm so there is enough time for pressure buildup.

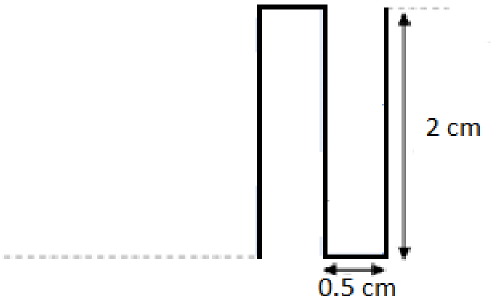

Figure 6.3-2 Pattern consisting of alternating track of 2 cm and 0.5 cm with a 90° angle transition. There is a 2 cm run-up track

The next step is the printing of lattice structures. This is a standard pattern found in the *Repetier* software. The distance between tracks is foreseen in the software as a the percentage of infill. The last step of this study is printing a 3D structure, this is in essence a layer by layer print of this lattice structure. The G-codes for all the printed patterns can be found in attachment D.1.

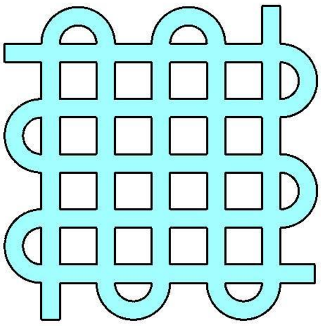

Figure 6.3-3 Example of a lattice structure

6.4 Validation methods

As mentioned before, the validation method of the trial and error phase is done visually. To give an idea of how this pass fail judgement works, some examples.

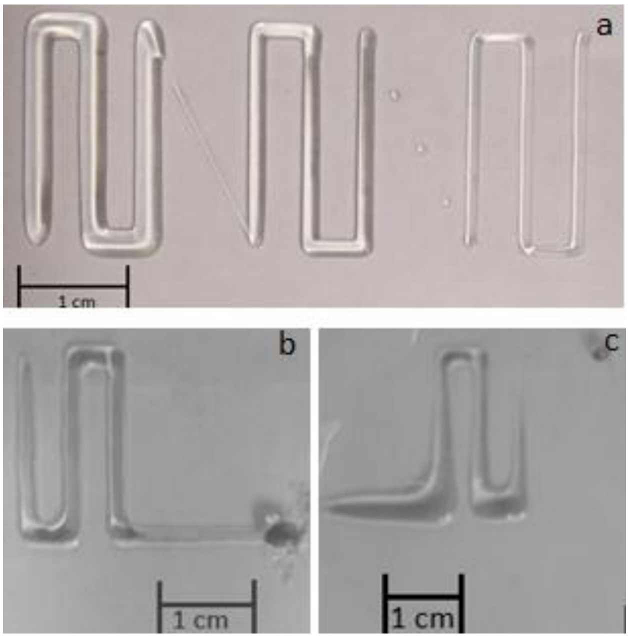

Figure 6.4-1 a) Cellink start at 70 kPa, 25G nozzle, respectively 2, 5 and 10 mm/s b) 15 w/v% Gelatin at 30°C, 50 kPa, 25G conical nozzle and 25 mm/s c) 15 w/v% Gelatin at 30°C, 110 kPa, 25G conical nozzle and 40 mm/s

There are different conclusion drawn from Figure 6.4-1. For the *Cellink start* a feed rate of 2 mm/s in combination with 70 kPa is less favorable compared to the other printing speeds because a finer track can be printed with similar consistency of the print. It is clear that the gelatin print at 70 kPa has smudges edges and the 90 ° corners are badly executed. For gelatin the 50 kPa with 25 mm/s feed rate has a better outcome than at 110 kPa with a feed rate of 40 mm/s. Even though the corners are not as sharp as with the *Cellink start* this a relative good result for the printing of gelatin at 30 °.

During the DOE the printed tracks are evaluated according to their track width. The measuring device is the *Hirox* microscope as described in chapter 3.5.2. Images are taken of the track with the specified width as well as pictured of at least one corner so it can still be acknowledge (and discarded if needed) when there is an inconsistency in the pattern.

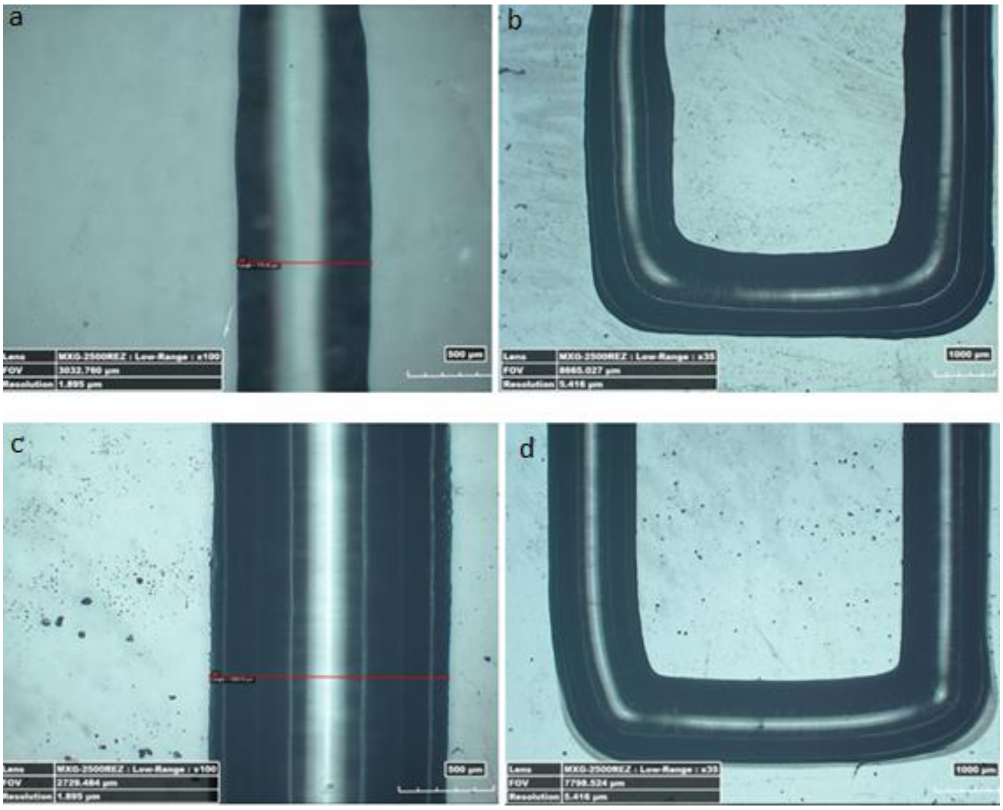

Figure 6.4-2 Microscopic images tracks and corners a) b) gelatin, 28 °C, 25G conical nozzle, 90 kPa, 40 mm/s c) d) Cellink start, 25G conical nozzle, 60 kPa, 15 mm/s

To give an idea how the microscopic measurements performed, Figure 6.4-2 shows microscopic images taken of gelatin and *Cellink start*. The red line on the track is one single width measurement.

There is a quite simple approach when taking measurements. One printed sample is exactly one replica in the DOE. However an average of multiple measurements are taken of one sample. The first approach implemented when printing with the *Cellink start* was measure each individual track three times at random locations, so there are a total of nine measurements per sample. However this is a time consuming approach and it is better to increase the amount of printed samples instead of the amount of measurements per track. For this reason when printing gelatin one measurement is taken per track, in total this is three measurements per sample. This is shown in Figure 6.4-3.

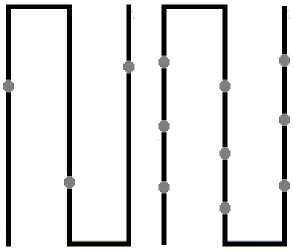

Figure 6.4-3 Indication of measurement methods, each dot presents a measurement at an arbitrary location

Per sample the average is taken from the measurements. This result is rounded because the data should be effected by the printing process only and not by the measuring device or other factors. The microscope has a resolution of 1.8 μm for the specific application. Additionally there are also human errors made while measuring. To partially overcome these measuring errors the measurements are rounded to **0.01 mm**.

6.5 Experiments Cellink start

Two nozzles were implemented as two separate experiments. A 25G (0.25 mm inner diameter) conical nozzle and a 20G blunt nozzle (0.61 mm inner diameter). Pressure range tests were conducted with an ambient temperature of 22 °C and repeated three times. There was little sign of droplet formation. This is a rough reference as it is difficult to visually tell the timing of flow.

25 G

Stream: (27 ± 2) kPa

Jetting: (94 ± 6) kPa

20 G

Stream: (95 ± 2) kPa

For the 20 G nozzle it was unclear when jetting occurred, however this was certainly at pressures above 150 kPa.

From the trial and error experiments the following levels were chosen.

25 G

Pressure: 60 kPa 80 kPa

Feed rate: 10 mm/s 15 mm/s 20 mm/s

20 G

Pressure: 90 kPa 110 kPa

Feed rate: 5 mm/s 15 mm/s 20 mm/s

The DOE was carried out with randomization of the printing parameters. Unfortunately the experiments with the blunt nozzle had to be repeated as, a presumably, human error slipped into the measurements causing distortion in the result.

6.5.1 Analyses of variance (ANOVA) [57]

The data is analyzed in *minitab*. It is assumed that the errors are randomly normally distributed with a zero mean of zero. The main purpose is to specify linear regression model, in order to predict the output (track width).

6.5.1.1 25G conical nozzle

Table 6.5-1 Results ANOVA Cellink start 25G conical nozzle

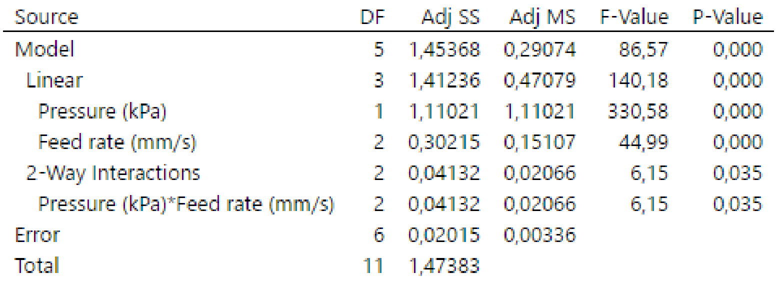

Source	DF	Adj SS	Adj MS	F-Value	P-Value
Model	5	1,45368	0,29074	86,57	0,000
Linear	3	1,41236	0,47079	140,18	0,000
Pressure (kPa)	1	1,11021	1,11021	330,58	0,000
Feed rate (mm/s)	2	0,30215	0,15107	44,99	0,000
2-Way Interactions	2	0,04132	0,02066	6,15	0,035
Pressure (kPa)*Feed rate (mm/s)	2	0,04132	0,02066	6,15	0,035
Error	6	0,02015	0,00336		
Total	11	1,47383			

With an α of 0.05 the p-Values indicate that all the first and second order effects are of significance (note that p ~ 0 for the pressure and feed rate). The adjusted R^2 value is 97.49%, meaning that the model is able to explain this percentage of variation. This is a pleasing result. The regression equation is the following.

$$\begin{aligned}\text{Track width (mm)} &\\ &= \mathrm{C1} + \mathrm{C2}(60\ \mathrm{kPa}) + \mathrm{C3}(80\ \mathrm{kPa}) + \mathrm{C4}\left(10\frac{\mathrm{mm}}{\mathrm{s}}\right) \\ &+ \mathrm{C5}\left(15\frac{\mathrm{mm}}{\mathrm{s}}\right) + \mathrm{C6}\ \left(20\frac{\mathrm{mm}}{\mathrm{s}}\right) + \mathrm{C7}\ \left(60\mathrm{kPa} * 10\frac{\mathrm{mm}}{\mathrm{s}}\right) \\ &+ \mathrm{C8}\ \left(60\ \mathrm{kPa} * 15\frac{\mathrm{mm}}{\mathrm{s}}\right) + \mathrm{C9}\ \left(60\ \mathrm{kPa} * 20\frac{\mathrm{mm}}{\mathrm{s}}\right) \\ &+ \mathrm{C10}\ \left(80\ \mathrm{kPa} * 10\frac{\mathrm{mm}}{\mathrm{s}}\right) + \mathrm{C11}\ \left(80\ \mathrm{kPa} * 15\frac{\mathrm{mm}}{\mathrm{s}}\right) \\ &+ \mathrm{C12}\ \left(80\ \mathrm{kPa} * 20\frac{\mathrm{mm}}{\mathrm{s}}\right)\end{aligned} \tag{6.5-1}$$

With the respective coefficients.

Table 6.5-2 Coefficients of the regression equation (Cellink start 25G conical nozzle)

C1	C2	C3	C4	C5	C6
0,9825	-0,3042	0,3042	0,2025	- 0,0175	- 0,1850
C7	C8	C9	C10	C11	C12
- 0,0658	- 0,0108	0,0767	0,0658	0,0108	- 0,0767

The main effect plots are shown on Figure 6.5-1. The impact of the feed rate and the pressure range on the track width are shown. The second order effect is shown on Figure 6.5-2.

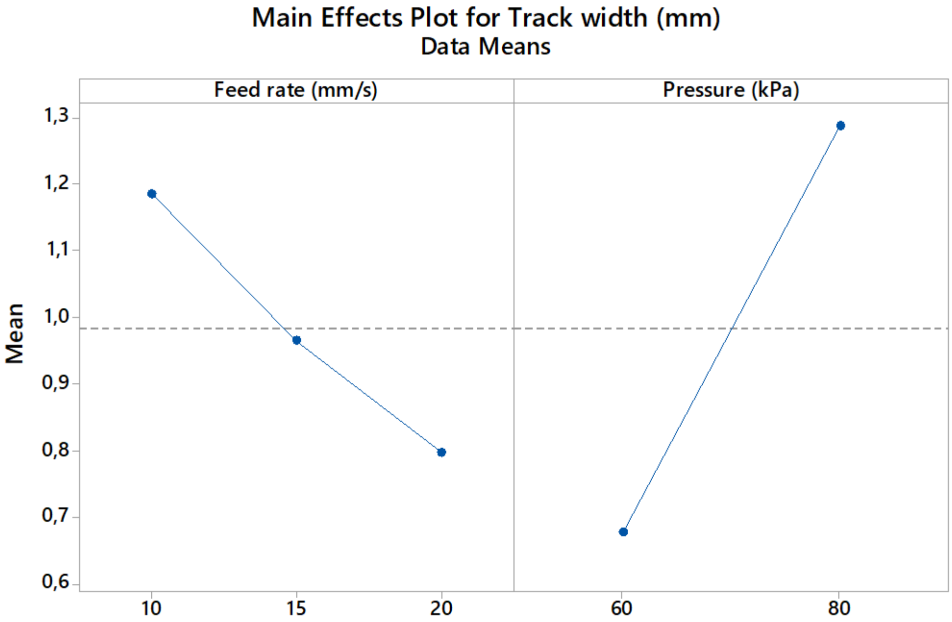

Figure 6.5-1 Main effect plot for the track width (mm) as a function of the feed rate (mm/s), left, and printing pressure (kPa), right

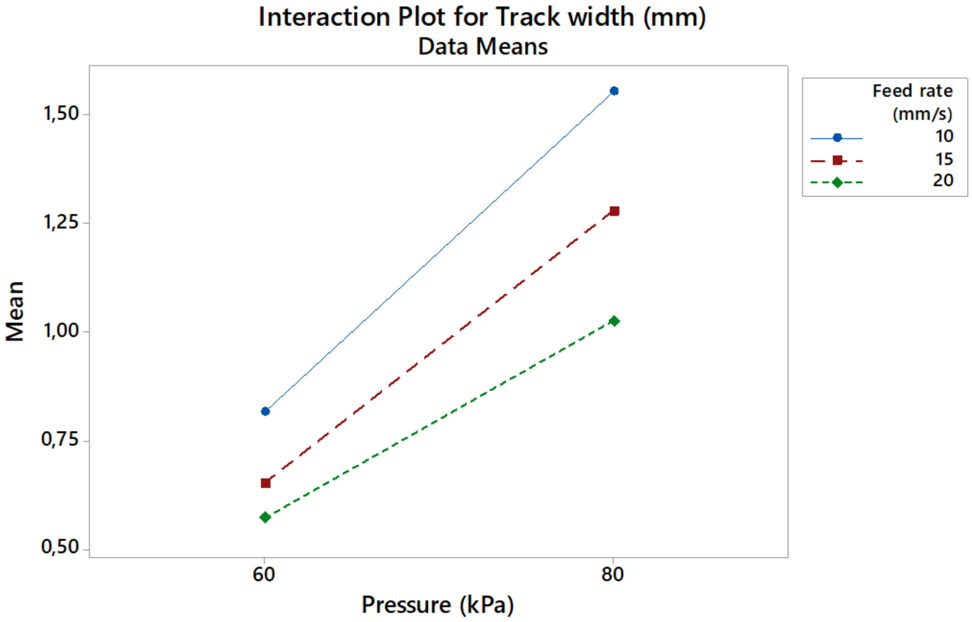

Figure 6.5-2 Interaction plot for the track width (mm) as a function of the two way interaction of the Pressure (kPa) and the feed rate (mm/s)

6.5.1.2 20G blunt nozzle

For this analyses three replicas are taken similar to the measuring method of the gelatin tracks as discussed in chapter 6.4.

Table 6.5-3 Results ANOVA Cellink start 20G blunt nozzle

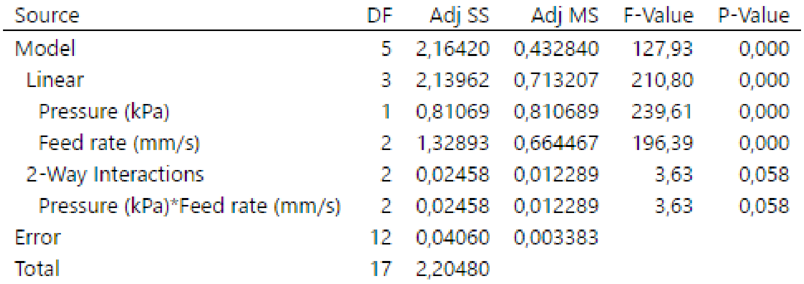

Source	DF	Adj SS	Adj MS	F-Value	P-Value
Model	5	2,16420	0,432840	127,93	0,000
Linear	3	2,13962	0,713207	210,80	0,000
Pressure (kPa)	1	0,81069	0,810689	239,61	0,000
Feed rate (mm/s)	2	1,32893	0,664467	196,39	0,000
2-Way Interactions	2	0,02458	0,012289	3,63	0,058
Pressure (kPa)*Feed rate (mm/s)	2	0,02458	0,012289	3,63	0,058
Error	12	0,04060	0,003383		
Total	17	2,20480			

When analyzing the P-values, only the first order interactions are significant. The adjusted R^2 value is 95.39%, which is again very pleasing. The regression equation is the following.

$$
\begin{aligned}
&\text{Track width (mm)}\\
&\quad = \mathrm{C1} + \mathrm{C2}(90\ \mathrm{kPa}) + \mathrm{C3}(110\ \mathrm{kPa}) + \mathrm{C4}\left(5\frac{\mathrm{mm}}{\mathrm{s}}\right)\\
&\quad + \mathrm{C5}\left(10\frac{\mathrm{mm}}{\mathrm{s}}\right) + \mathrm{C6}\ \left(15\frac{\mathrm{mm}}{\mathrm{s}}\right) + \mathrm{C7}\ \left(90\mathrm{kPa} * 5\frac{\mathrm{mm}}{\mathrm{s}}\right)\\
&\quad + \mathrm{C8}\ \left(90\ \mathrm{kPa} * 10\frac{\mathrm{mm}}{\mathrm{s}}\right) + \mathrm{C9}\ \left(90\ \mathrm{kPa} * 15\frac{\mathrm{mm}}{\mathrm{s}}\right)\\
&\quad + \mathrm{C10}\ \left(110\ \mathrm{kPa} * 5\frac{\mathrm{mm}}{\mathrm{s}}\right) + \mathrm{C11}\ \left(110\ \mathrm{kPa} * 15\frac{\mathrm{mm}}{\mathrm{s}}\right)\\
&\quad + \mathrm{C12}\ \left(110\ \mathrm{kPa} * 20\frac{\mathrm{mm}}{\mathrm{s}}\right)
\end{aligned}
\tag{6.5-2}
$$

The coefficients have the following value.

Table 6.5-4 Coefficients of the regression equation (Cellink start 20G blunt nozzle)

C1	C2	C3	C4	C5	C6
1,9967	- 0,2122	0,2122	0,3633	- 0,0733	- 0,2900
C7	C8	C9	C10	C11	C12
- 0,0478	0,0056	0,0422	0,0478	0,0056	- 0,0422

The main effect plots are shown on Figure 6.5-3. The impact of the feed rate and the pressure range on the track width are shown. The second order effects are shown on Figure 6.5-4.

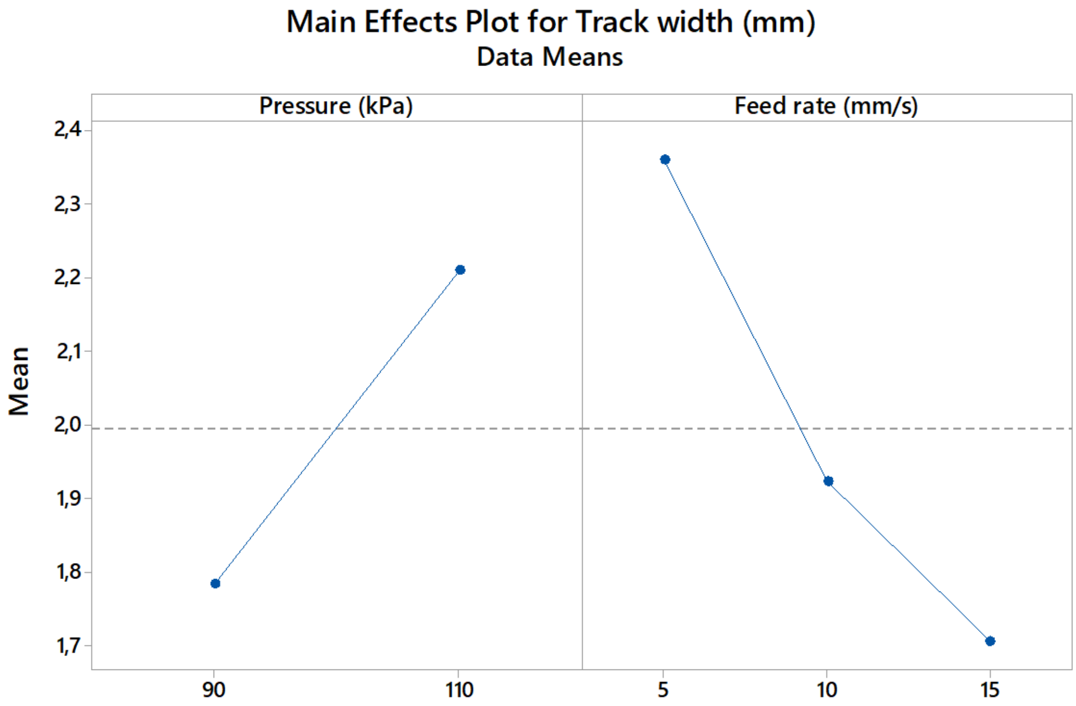

Figure 6.5-3 Main effect plot for the track width (mm) as a function of the feed rate (mm/s), left, and printing pressure (kPa), right

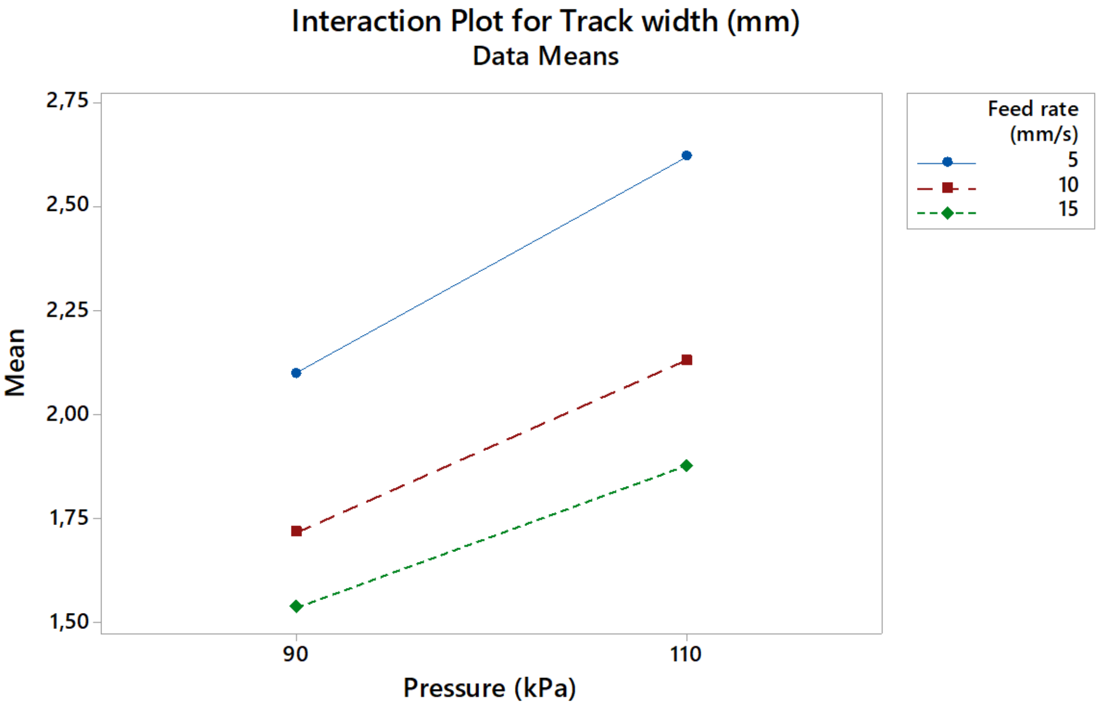

Figure 6.5-4 Interaction plot for the track width (mm) as a function of the two way interaction of the Pressure (kPa) and the feed rate (mm/s)

6.5.2 Printing of lattice structure [30]

As the results were pleasing from the ANOVA, the process can be stated as controlled. Printing of lattice structure can be done. From experience and experimenting, suitable parameters were chosen. The layer height was adjusted to the nozzle diameters.

25 G: 60 kPa 15 mm/s

20 G: 90 kPa 15 mm/s

All parameters are fixed apart from the infill percentage.

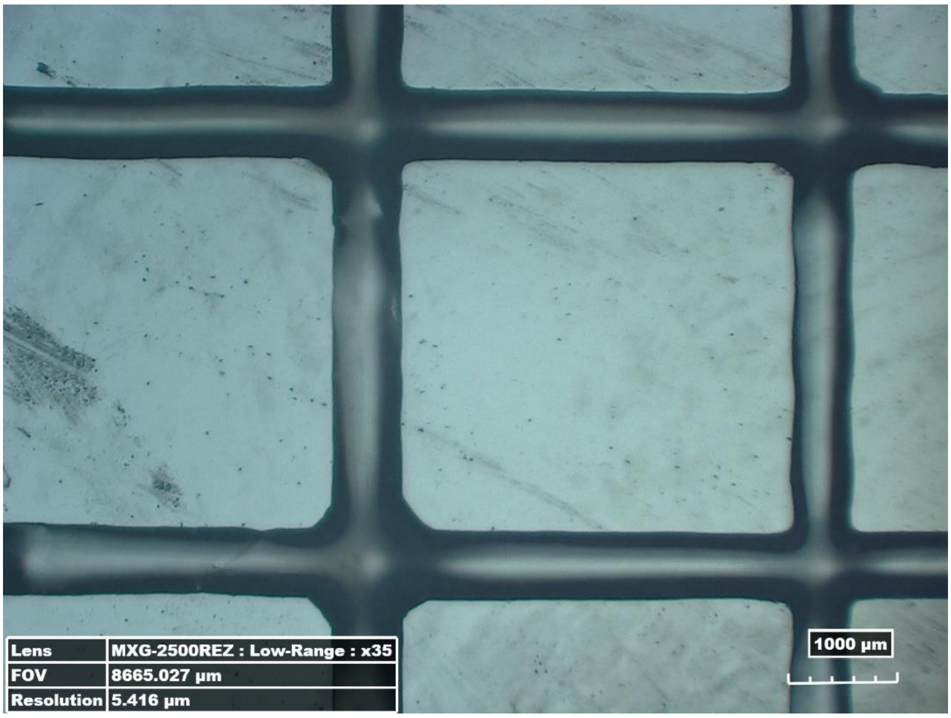

Figure 6.5-5 Lattice structure printed with Cellink start 25G conical nozzle, 60 kPa, 15 mm/s, 20% infill

Figure 6.5-5 illustrates an infill of 20 % printed with a 25G nozzle. This infill clearly shows an increased diffusion at the junctions of the tracks. An increase in diffusion rate is visually perceived as the infill percentage is increased as shown in Figure 6.5-6. So a desired porosity can be implemented by selecting a suitable infill. However note that with an infill of 70% a number of cavities collapsed, this should be avoided.

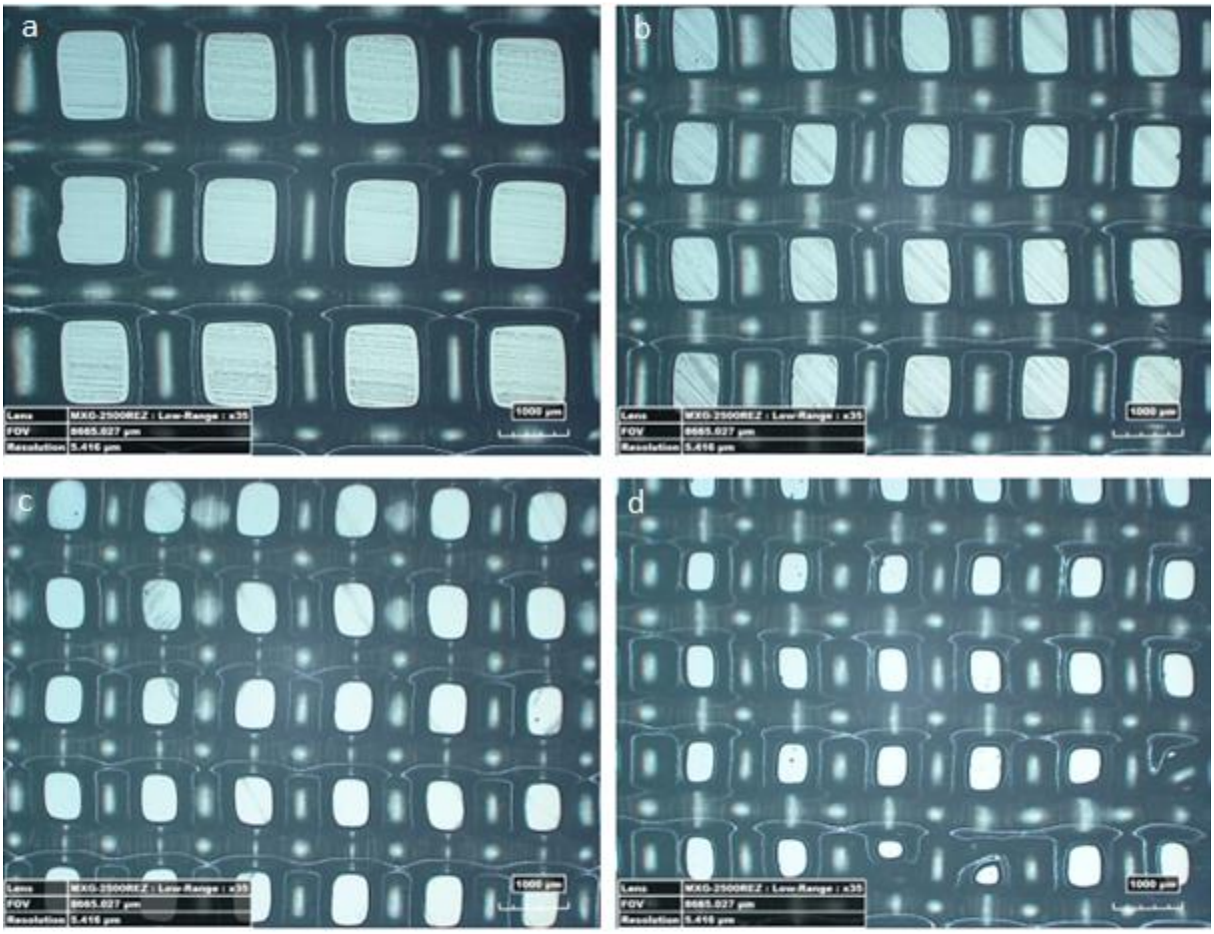

Figure 6.5-6 Lattice structure printed with Cellink start 25G conical nozzle, 60 kPa, 15 mm/s, a) 40% infill b) 50% infill c) 60% infill d) 70% infill

The diffusion rate can be calculated relative to the theoretical dimensions of the lattice structure.

$$\varphi = \frac{A_{th} - A_e}{A_{th}} * 100\% \qquad 6.5\text{-}3$$

With φ: diffusion rate

A_{th} : Theorethical area of the cavity

A_e : Experimental area of the cavity

The theoretical area is calculated using the track distance implemented by the software and a track width that is equal to the nozzle diameter. There is a number of one or three replicas, the data can be found in attachment D.2.3. Diffusion rates:

20% infill:	11%
40% infill:	(62 ± 1) %
50% infill:	(60 ± 4) %
60% infill:	(69 ± 2) %

70% infill: (76 ± 8) %

The trend does seem to be, as the microscopic images imply, that the diffusion rate increases with increasing infill. The same calculations have been carried out with the 20G blunt nozzle with 20% and 40% infill.

20% infill: (24 ± 2) %

40% infill: (83 ± 3) %

The same trend in increase of the diffusion rate is revealed.

6.5.3 3D structure printing

With the 25G conical nozzle the printing was taken a step further and a 3D construct was printed. This is a 0.5 cm high (33 layers) structure printed at 60 kPa with a feed rate of 15 mm/s and infill of 40%. With a layer height of 0.25 mm (nozzle diameter) there was no attachment between layers. The layer height was adjusted until there was bonding, this was at 0.15 mm. The structure is 2 cm x 2 cm in width and length.

Figure 6.5-7 3D structure, Cellink start, 25G conical nozzle, 60 kPa, 15 mm/s feed rate, 40% infill, 0.15 mm layer height. Dimensions (2 x 2 x 0.5) cm

Figure 6.5-7 shows a microscopic image of the structure. In this case not only diffusion takes place, but also fusion between layers. As a results the cavity of the top layer is larger and more consistent in shape than that of the bottom layer.

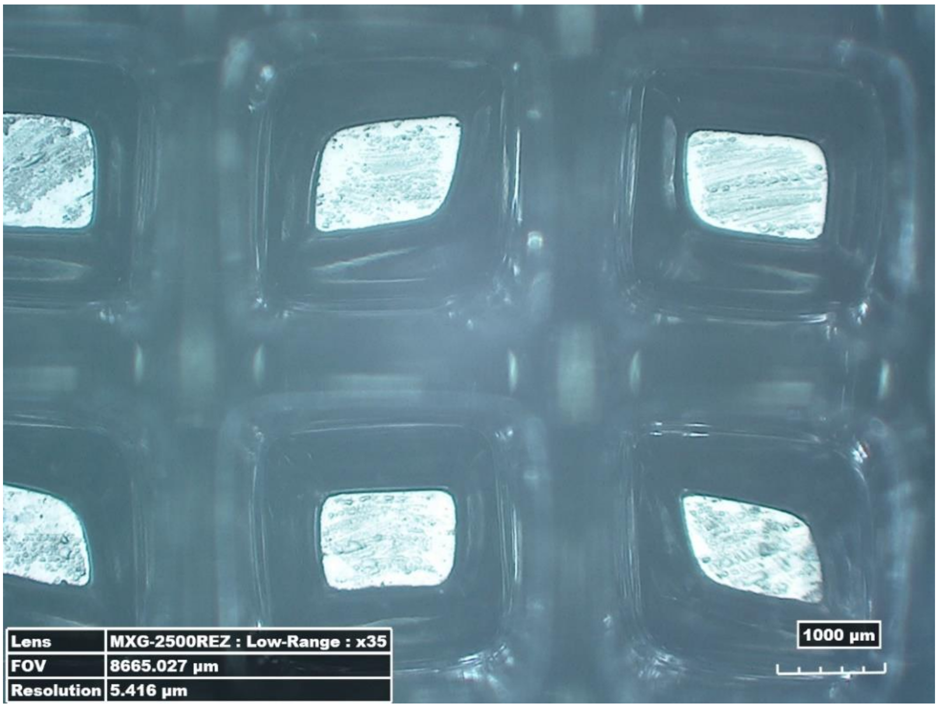

Figure 6.5-8 Microscopic image (top) 3D structure, Cellink start, 25G conical nozzle, 60 kPa, 15 mm/s feed rate, 40% infill, 0.15 mm layer height

6.6 Experiments Gelatin

As mentioned previously all experiment are done with a 15 w/v% concentration of gelatin and functioning of the cooling plate. The first experiments were carried out with conical nozzles (25G and 27G, respectively 0.25 mm and 0.20 mm inner diameter). The initial trial and error tests were carried out at 30 °C. This soon turned out to be difficult presumably because of the liquidlike behavior of the gelatin. For this reason the printing temperature was selected at 28 °C, this is right above the calculated gelation point in chapter 4.4.3 of 27.4 °C. The measuring of the gelatin temperature and ambient temperature is done with the thermocouple described in chapter 3.5.7. The pressure range test at 28 °C was carried out, as this is done visually this data should be taken as a rough estimation. Jetting was not noted as it was difficult to tell when this occurred.

25 G

Droplets: (24 ± 24) kPa

Stream: (65 ± 5) kPa

27 G

Droplets: (31 ± 1) kPa

Stream: (153 ± 25) kPa

A separate experiment was conducted for the conical and blunt nozzles. Three replicas were taken, each on a different day to maximize the randomization. The first levels deducted from trial and error are the following.

Nozzle:	20G	27G	
Feed rate:	20 mm/s	40 mm/s	
Pressure:	50 kPa	70 kPa	90 kPa

When using the blunt nozzles a different approach was implemented because printing below the gelation temperature is a possibility due to the needle shape. The gelatin can be pushed out of the nozzle as filament strand. For the printing temperature the aim was 25 °C. The idea was to keep the nozzles in a heated bath (of around 40 °C) so when printing the outer layer of the filament melts and the inner layer slides through the nozzle still gelated. This technique required a lot of pressure. Because the compressor could not provide pressures above 300 kPa there was a limitation of the pressure range. Another consequence was that not all nozzle diameters could be used as with smaller inner diameters the gelatin could not be pushed out. The selected nozzle is a 22G (0.41 mm) that is capable of working within the provided pressure range. There was no separate pressure range test conducted. The chosen levels for the DOE are the following.

Pressure:	150 kPa	200 kPa	250 kPa
Feed rate:	30 mm/s	40 mm/s	50 mm/s

The DOE was conducted for the conical nozzles. However from the ANOVA the adjusted R^2 value was 10,42% indicating that the process is not under control. For this reason the ANOVA will not be further analyzed as it is of absolute importance that the process in under control. To give an indication of some of the causes, for each conducted measurement the date, temperature and the days since the gelatin was manufactured is recorded. For the blunt nozzle a DOE was not conducted because the outcome of the samples were not consequent to the point that some sample completely diffused into each other and measuring a width was not possible. The processed data for the DOE can be consulted in appendix D.4.

6.6.1 Problem causes and potential solutions

It is clear that the printing process of gelatin is not under control leading to a random outcome a the measured track width. To have an idea of what causes lie at the basis of the problem, a fishbone diagram is employed. Here possible causes are listed, this a more philosophical approach.

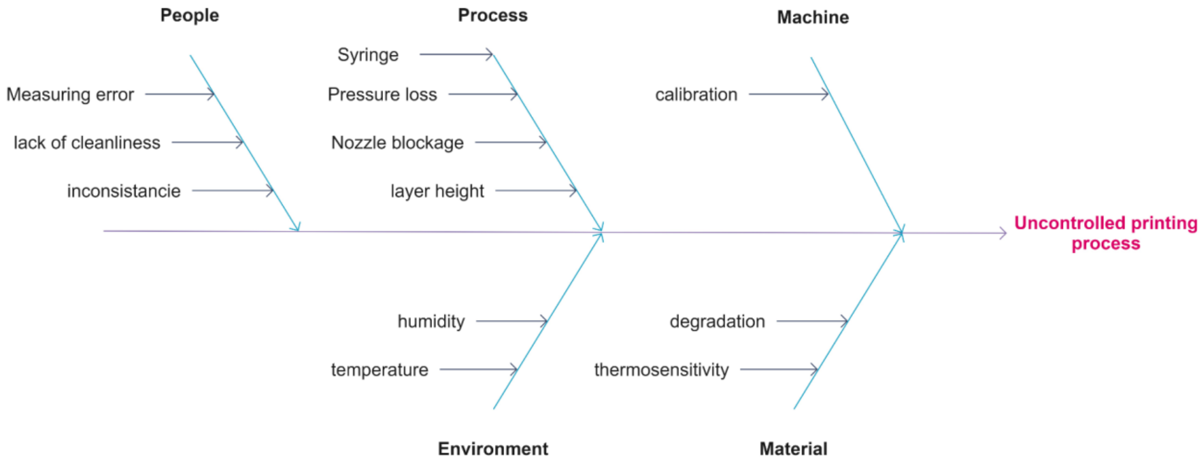

Figure 6.6-1 Cause and effect diagram for the response of the printing process (i.e. the track width)

6.6.1.1 Environment

It is strongly believed that one of the major factors that have an impact on the process is the ambient temperature. On a day that the ambient temperature was around 30 °C, printing was simply not possible because the viscosity of the gelatin was affected, thus the material behaved completely different. It is advisable to perform the experiments in a temperature regulated room.

It is not clear what impact the humidity has on the printing process, partially because this data could not be logged.

6.6.1.2 Material

The thermosensitive property of gelatin goes hand in hand with mentioned effect of the ambient temperature. The viscosity is dependent of the ambient temperature and this sensitivity is more outspoken within the range of 25 °C – 30 °C because that is where the sol-gel transition takes place. To make gelatin less thermosensitive a solution might be to manufacture a gelatin blend that is less sensitive to the environmental temperature.

Another factor is that gelatin degrades over time, keeping the material in the fridge does not overcome the problem completely. During the experimenting phase gelatin was manufactured on a weekly basis. It is possible that by the end of the week, due to degradation, that the gelatin behaved differently.

6.6.1.3 Process

As mentioned in chapter 5.1, different cartridges were used which had to cope with pressure loss. Even though plumbers grease was used, there was still some pressure loss especially at higher pressure ranges. As the loss of pressure is not a constant this could have an impact on the printing process.

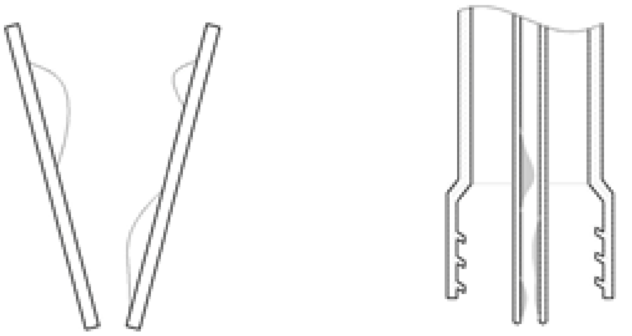

Figure 6.6-2 Gelatin stuck inside the conical nozzle (left) and inside the syringe (right)

There were indication of another problem with the nozzle and syringe as source as illustrated in Figure 6.6-2. First of all the syringe is connected to the nozzle with a luer-lock system. When a specific syringe is in use, this connection is not heated by the heating element. This could cause gelation in the syringe. Additionally it is plausible that between the printing of samples, before printing, during printing or after, that pieces of gelatin gelate in the nozzle itself. To overcome this problem a stricter cleaning procedure can be followed:

- Directly after printing the nozzle is be cleaned with water (of at least 30 °C)
- It is then cleaned with ethanol
- The nozzle placed inside a water bath (of at least 30 °C), a long duration is preferred
- The nozzle is cleaned again with ethanol

During the course of the experiments when dealing with the printing of tracks, the layer height is kept constant. An idea for future work is to also study the consequence of taking the layer height as a variable as this has an influence of the process.

6.6.1.4 Machine

As illustrated in chapter 6.2, calibration is of extreme importance. It is in this light disappointing that the bioprinter does not implement a standard calibration method and that this has to be done manually.

6.6.1.5 People

There are always a certain of human errors that could occur. First of all cleanliness is of importance, making sure the material is cleaned properly before use could help avoid certain errors.

Measuring errors can always occur and additionally each person could measure the same sample in a slightly different way. Sometimes it difficult to judge where the boundary of a track lies. This particular problem is partially overcome with the rounding of the measurement results.

The last problem could be inconsistencies. For example the calibration of the Z-axis is not again repeated when a different nozzle type is implemented, this could lead to a different printing distance from the platform and thus the results differ.

6.7 Conclusion

In this chapter the focus lied on experimenting with the *Cellink start* and 15 w/v% gelatin. The information gained from experiments revolving around the hydrogel properties in chapter 4 served as a backbone for the experiments.

Cellink start material, as expected, proved itself to have favorable printing properties. The printed tracks and 90° corners were printed with a high rate of repeatability. Printing was done with a 25G conical nozzle and a 20G blunt nozzle. The blunt nozzle required to be operated at a higher pressure range, the flow of material through the nozzle was induced at approximately 70 kPa higher. The process was under control as the results from the ANOVA stated and over 95% of the variation could be explained for both the conical and blunt nozzle by the calculated ANOVA model. The results state that both the pressure and printing speed as well as their two way interaction have a significant effect on the track width. Increasing the pressure and decreasing the printing speed results in a wider track.

With this result lattice structures was commenced with suitable parameters. Here the focus lies on the infill of the pattern. It was stated that with a higher percentage of infill a higher a higher diffuse rate was perceived. When ranging the infill from 20% to 40% for a 25G conical nozzle there was a 51% increase of diffusion rate and for a 20G blunt nozzle a 59% increase of diffusion rate. It is interesting to see that for two different nozzle types with different inner diameters, the results are in a similar range. Furthermore starting from a lattice structure as pattern a 3D structure of (2 x 2 x 0.5) cm was successfully printed.

The printing process of gelatin was unfortunately not under control. For this reason a cause and effect diagram was setup. There are multiple causes that could lie at the base of the variation. The most outspoken causes, based on experience, are the ambient temperature, this goes hand in hand with the thermo-sensitivity of the gelatin and the gelation of gelatin in the nozzle.

7 CONCLUSION

This thesis can be divided into three main phases, namely the study of hydrogel material, the analyzing and improving of the printing process and the experimental phase, where the goal is to find the ideal printing parameters.

The first phase is a property study of the chosen hydrogel material. In this case gelatin is chosen as it provides an ideal environment and possesses shear thinning properties, which protects the cells against stresses and creates a smooth flow through the nozzle. Furthermore gelatin is a collagen derived hydrogel which can be used as a base material, for example it can be modified to form gelMA or a gelatin blend can be manufactured with alginate. Another interesting approach is to manufacture a gelatin HA nanopowder blend. The HA augments the mechanical properties of the hydrogel, making it more suitable for BTE. However due to the complexity of manufacturing such blend, this was beyond the scope of this thesis. Experimenting with a gelatin HA nanopowder blend definitely has potential for future work. Besides gelatin, *Cellink start* material is used, as it is a material manufactured by the company *Cellink* itself and has suitable printing properties, thus can serve as a good reference material.

The most import part of the hydrogel study is the rheological data. The results indicate that for *Cellink start*, 5 w/v% and 15 w/v% shear thinning properties occur. As 15 w/v% gelatin was used as printing material, a temperate sweep test was performed, which indicated that the sol-gel transition takes place around 27 °C. This is valuable information with regards to the printing phase. The idea from the hydrogel study emerged to induce thermal crosslinking, despite the formation of weak reversible bonds, it can create instant stability of the printed material. It can be viewed as a first step before an additional crosslinking method is applied.

The main focus of the second phase is improving the printing process. A drawback of the *Inkredible+* was that it did not possess a cooling plate to apply thermal crosslinking. To overcome this problem a cooling plate was manufactured; it was able to cool down at least 12 °C from the ambient air and did so in under 3 minutes. Furthermore the temperature difference between the center of the cooling plate and its outer corner was about 3 °C. The temperature is regulated by an *Arduino nano* microcontroller which uses PID to regulate the setpoint of the cooling plate at 10 °C. Lowering this temperature might be alarming for the cell viability.

Another improvement made was switching the *Cellink* syringes with syringes that provided better sealing. This was to overcome the piston from being stuck in position or worse, to overcome the material from pouring out because the vacuum was lost. The new syringes helped to overcome this problem, however they did experience pressure loss at the connection between the syringe and the pressure supply. Finally there were doubts about the effectiveness of the heating elements of the bioprinter. To investigate this, the heating elements were analyzed with a thermal camera. The results showed that the material is the syringes heated homogeneously, which makes the heating element suitable for printing at higher temperatures to a certain extend.

During the last phase all the improvements and knowledge gained from the previous phases were collected and implemented in order to find suitable printing parameters. *Cellink start* material quickly proved to be a relatively easy material to print. A full factorial DOE was conducted with the feed rate and printing pressure as factors and the printed track width as response. The idea was to print a fine track that still has its consistency in shape. The results from the ANOVA the regression equation, i.e. the relationship between the factors and the response. Increasing the printing pressure and decreasing the feed rate lead to a increase in line width. As the process was under control a (2 x 2 x 0.5 cm) 3D structure was successfully printed.

The printing of gelatin on the other hand did not go as smoothly. The process was not under control, this was confirmed by the results of the ANOVA. A cause and effect diagram was implemented to try and unravel the main causes of the problem. The two main causes that are assumed to lie at the basis are the printing temperature and the gelation of the material in the nozzle. For this reason printing in a controlled temperature room is recommended. Additionally a new cleaning process was implemented in order to ensure the cleanliness of the nozzle in use. Nozzles can best be cleaned after every run.

For future work, the most interesting aspect is the development of a hydrogel or even bioink. In this thesis a basic material, namely gelatin, was implemented. It would be of interesting to explore the possibilities of a gelatin blend in order to induce favorable properties.

Literature review

[1] C. M. Piard, Y. Chen, en J. P. Fisher, “Cell-Laden 3D Printed Scaffolds for Bone Tissue Engineering”, *Clinic Rev Bone Miner Metab*, vol. 13, nr. 4, pp. 245–255, dec. 2015.

[2] J. J. Sela en A. B. Itai, “Principles of bone regeneration”, *Springer Science & Business Media*, 2012. .

[3] H. Burchardt, “The Biology of Bone Graft Repair”, *Clinical Orthopaedics & Related Research*, vol. 174, pp. 28–34, apr. 1983.

[4] Y. Huang, X.-F. Zhang, G. Gao, T. Yonezawa, en X. Cui, “3D bioprinting and the current applications in tissue engineering”, *Biotechnol. J.*, vol. 12, nr. 8, p. n/a-n/a, aug. 2017.

[5] L. Roseti *e.a.*, “Scaffolds for Bone Tissue Engineering: State of the art and new perspectives”, *Materials Science and Engineering: C*, vol. 78, nr. Supplement C, pp. 1246–1262, sep. 2017.

[6] R. R. Jose, M. J. Rodriguez, T. A. Dixon, F. Omenetto, en D. L. Kaplan, “Evolution of Bioinks and Additive Manufacturing Technologies for 3D Bioprinting”, *ACS Biomater. Sci. Eng.*, vol. 2, nr. 10, pp. 1662–1678, okt. 2016.

[7] S. V. Murphy en A. Atala, “3D bioprinting of tissues and organs”, *Nature Biotechnology; New York*, vol. 32, nr. 8, pp. 773–85, aug. 2014.

[8] A. Berger, “Magnetic resonance imaging”, *BMJ*, vol. 324, nr. 7328, p. 35, jan. 2002.

[9] A. Carlier *e.a.*, “Computational model-informed design and bioprinting of cell-patterned constructs for bone tissue engineering”, *Biofabrication*, vol. 8, nr. 2, p. 025009, 2016.

[10] C. Mandrycky, Z. Wang, K. Kim, en D.-H. Kim, “3D bioprinting for engineering complex tissues”, *Biotechnology Advances*, vol. 34, nr. 4, pp. 422–434, jul. 2016.

[11] I. Donderwinkel, J. C. M. van Hest, en N. R. Cameron, “Bio-inks for 3D bioprinting: recent advances and future prospects”, *Polymer Chemistry*, vol. 8, nr. 31, pp. 4451–4471, 2017.

[12] I. T. Ozbolat en M. Hospodiuk, “Current advances and future perspectives in extrusion-based bioprinting”, *Biomaterials*, vol. 76, nr. Supplement C, pp. 321–343, jan. 2016.

[13] M. Guvendiren, J. Molde, R. M. D. Soares, en J. Kohn, “Designing Biomaterials for 3D Printing”, *ACS Biomater. Sci. Eng.*, vol. 2, nr. 10, pp. 1679–1693, okt. 2016.

[14] A. Panwar en L. P. Tan, “Current Status of Bioinks for Micro-Extrusion-Based 3D Bioprinting”, *Molecules*, vol. 21, nr. 6, p. 685, mei 2016.

[15] S. Ji en M. Guvendiren, “Recent Advances in Bioink Design for 3D Bioprinting of Tissues and Organs”, *Front Bioeng Biotechnol*, vol. 5, apr. 2017.

[16] W. Aljohani, M. W. Ullah, X. Zhang, en G. Yang, “Bioprinting and its applications in tissue engineering and regenerative medicine”, *International Journal of Biological Macromolecules*, sep. 2017.

[17] J. Jia *e.a.*, “Engineering alginate as bioink for bioprinting”, *Acta Biomaterialia*, vol. 10, nr. 10, pp. 4323–4331, okt. 2014.

[18] K. Yue, G. Trujillo-de Santiago, M. M. Alvarez, A. Tamayol, N. Annabi, en A. Khademhosseini, “Synthesis, properties, and biomedical applications of gelatin methacryloyl (GelMA) hydrogels”, *Biomaterials*, vol. 73, pp. 254–271, dec. 2015.

[19] D. B. Kolesky, R. L. Truby, A. S. Gladman, T. A. Busbee, K. A. Homan, en J. A. Lewis, “3D Bioprinting of Vascularized, Heterogeneous Cell-Laden Tissue Constructs”, *Adv. Mater.*, vol. 26, nr. 19, pp. 3124–3130, mei 2014.

[20] E. M. Ahmed, “Hydrogel: Preparation, characterization, and applications: A review”, *Journal of Advanced Research*, vol. 6, nr. 2, pp. 105–121, mrt. 2015.

[21] W. E. Hennink en C. F. van Nostrum, “Novel crosslinking methods to design hydrogels”, *Advanced Drug Delivery Reviews*, vol. 64, nr. Supplement, pp. 223–236, dec. 2012.

[22] H. Jeong Yoon *e.a.*, *Cold Water Fish Gelatin Methacryloyl Hydrogel for Tissue Engineering Application*, vol. 11. 2016.

[23] C.-H. Yao, B.-S. Liu, C.-J. Chang, S.-H. Hsu, en Y.-S. Chen, “Preparation of networks of gelatin and genipin as degradable biomaterials”, *Materials Chemistry and Physics*, vol. 83, nr. 2, pp. 204–208, feb. 2004.

[24] X. Chen *e.a.*, “Fabrication of gelatin methacrylate/nanohydroxyapatite microgel arrays for periodontal tissue regeneration”, *International Journal of Nanomedicine*, 14-sep-2016. [Online]. Beschikbaar op: https://www.dovepress.com/fabrication-of-gelatin-methacrylatenanohydroxyapatite-microgel-arrays--peer-reviewed-fulltext-article-IJN.

[25] S. Wüst, M. E. Godla, R. Müller, en S. Hofmann, “Tunable hydrogel composite with two-step processing in combination with innovative hardware upgrade for cell-based three-dimensional bioprinting”, *Acta Biomaterialia*, vol. 10, nr. 2, pp. 630–640, feb. 2014.

[26] J. Malda *e.a.*, “25th Anniversary Article: Engineering Hydrogels for Biofabrication”, *Adv. Mater.*, vol. 25, nr. 36, pp. 5011–5028, sep. 2013.

[27] K. Hölzl, S. Lin, L. Tytgat, S. V. Vlierberghe, L. Gu, en A. Ovsianikov, “Bioink properties before, during and after 3D bioprinting”, *Biofabrication*, vol. 8, nr. 3, p. 032002, 2016.

[28] T. Billiet, E. Gevaert, T. De Schryver, M. Cornelissen, en P. Dubruel, “The 3D printing of gelatin methacrylamide cell-laden tissue-engineered constructs with high cell viability”, *Biomaterials*, vol. 35, nr. 1, pp. 49–62, jan. 2014.

[29] A. Blaeser, D. F. Duarte Campos, U. Puster, W. Richtering, M. M. Stevens, en H. Fischer, “Controlling Shear Stress in 3D Bioprinting is a Key Factor to Balance Printing Resolution and Stem Cell Integrity”, *Adv. Healthcare Mater.*, vol. 5, nr. 3, pp. 326–333, feb. 2016.

[30] Y. He, F. Yang, H. Zhao, Q. Gao, B. Xia, en J. Fu, “Research on the printability of hydrogels in 3D bioprinting”, *Scientific Reports*, vol. 6, p. 29977, jul. 2016.

[31] “Inkredible+ User Manual”. Cellink.

[32] “CELLINK Start ~ Bioinks”, *CELLINK*, 06-sep-2016. [Online]. Beschikbaar op: https://cellink.com/product/cellink-start-2/.

[33] S. B. Ross-Murphy, “Structure and rheology of gelatin gels: recent progress”, *Polymer*, vol. 33, nr. 12, pp. 2622–2627, jan. 1992.

[34] “Gelatin”, *Sigma-Aldrich*. [Online]. Beschikbaar op: https://www.sigmaaldrich.com/technical-documents/articles/biofiles/gelatin.html.

[35] “Hydroxyapatite 677418”, *Sigma-Aldrich*. [Online]. Beschikbaar op: https://www.sigmaaldrich.com/catalog/product/aldrich/677418.

[36] “Differential scanning calorimetry”. [Online]. Beschikbaar op: https://www.mtm.kuleuven.be/equipment/diffscan/diffscan.

[37] “Hirox Europe Ltd | Products | Digital Microscope KH-8700”. [Online]. Beschikbaar op: http://www.hirox-europe.com/products/microscope/index8700.html.

[38] KU Leuven, “SMaRT MCR501 (Anton Paar)”. [Online]. Beschikbaar op: https://cit.kuleuven.be/smart/infrastructure/documents/mcr501.pdf.

[39] S. YDK, “User’s Manual, p. 104.

[40] “TESCAN | VEGA3”. [Online]. Beschikbaar op: https://www.tescan.com/en-us/technology/sem/vega3.

[41] “FLIR A300 (30Hz) - 48201-1001 - FLIR Systems - IP Thermography Camera - 320x240 Resolution - 25°(H) × 18.8°(V) FOV - MPEG-4 Streamed Video - Multiple Lens Options”. [Online]. Beschikbaar op: http://www.flircameras.com/flir_a-series_a300.htm.

[42] “MARTEL306 manual”. [Online]. Beschikbaar op: https://www.instrumart.com/assets/MARTEL306_manual.pdf.

[43] N. Stojilovic, “Why Can’t We See Hydrogen in X-ray Photoelectron Spectroscopy?”, *J. Chem. Educ.*, vol. 89, nr. 10, pp. 1331–1332, sep. 2012.

[44] “2012 DSC Brochure”. [Online]. Beschikbaar op: http://www.tainstruments.com/pdf/brochure/2012%20DSC%20Brochure%20r1.pdf.

[45] T. Instruments en D. Wylie, “Universal Analysis Getting Started Guide”, p. 28.

[46] C. Yan en D. J. Pochan, “Rheological properties of peptide-based hydrogels for biomedical and other applications”, *Chem. Soc. Rev.*, vol. 39, nr. 9, pp. 3528–3540, aug. 2010.

[47] J. V. David Strutt, “The Role of Rheology in Polymer Extrusion”, *ResearchGate*. [Online]. Beschikbaar op: https://www.researchgate.net/publication/266472193_The_Role_of_Rheology_in_Polymer_Extrusion..

[48] “Rheology applications note, the principles and applications of the Cox-Merz rule”. TA Instruments, Inc.

[49] F. A. Morrison, *Understanding Rheology*. Oxford University Press, 2001.

[50] F. A. Osorio, E. Bilbao, R. Bustos, en F. Alvarez, “Effects of Concentration, Bloom Degree, and pH on Gelatin Melting and Gelling Temperatures Using Small Amplitude Oscillatory Rheology”, *International Journal of Food Properties*, vol. 10, nr. 4, pp. 841–851, okt. 2007.

[51] “Nordson Piston, 5”. [Online]. Beschikbaar op: https://www.hisco.com/Manufacturers/Nordson/Adhesives-Sealants-Tapes/Dispensing-Equipment-Accessories/Adhesive-Dispensing-Equipment-Accessories/7012172-16022.

[52] "400 Series Syringe Pistons". [Online]. Beschikbaar op: https://www.adhesivedispensing.net/400_Series_Syringe_Pistons_s/120.htm.

[53] "Meerstetter - TEC / Peltier Element Design Guide | Compendium". [Online]. Beschikbaar op: https://www.meerstetter.ch/compendium/tec-peltier-element-design-guide.

[54] E. Fylladitakis, "Battle of The CPU Stock Coolers! 7x Intel vs 5x AMD, plus an EVO 212". [Online]. Beschikbaar op: https://www.anandtech.com/show/10500/stock-cooler-roundup-intel-amd-vs-evo-212.

[55] "Arduino Nano Pinout & Schematics - Complete tutorial with pin description". [Online]. Beschikbaar op: http://www.circuitstoday.com/arduino-nano-tutorial-pinout-schematics.

[56] Texas Instruments, "LM35 Precision Centigrade Temperature Sensors datasheet". [Online]. Beschikbaar op: http://www.ti.com/lit/ds/symlink/lm35.pdf.

[57] M. L. G. Sr en M. George, *Lean Six Sigma for Service: How to Use Lean Speed and Six Sigma Quality to Improve Services and Transactions*. McGraw Hill Professional, 2003.

[58] B. Clarke, "Normal Bone Anatomy and Physiology", *CJASN*, vol. 3, nr. Supplement 3, pp. S131–S139, jan. 2008.

[59] A. E. Oestreich, "The Two Types of Bone Formation", in *Growth of the Pediatric Skeleton*, Springer, Berlin, Heidelberg, 2008, pp. 1–5.

[60] J.-Y. Rho, L. Kuhn-Spearing, en P. Zioupos, "Mechanical properties and the hierarchical structure of bone", *Medical Engineering & Physics*, vol. 20, nr. 2, pp. 92–102, mrt. 1998.

[61] "BBC - GCSE Bitesize: Bone growth". [Online]. Beschikbaar op: http://www.bbc.co.uk/schools/gcsebitesize/pe/appliedanatomy/2_anatomy_skeleton_rev4.shtml.

[62] CENGEL, Yunus A., et al., *Fundamentals of thermal-fluid sciences*. . New York, NY: McGraw-Hill, 2008.

[63] "Air Properties". [Online]. Beschikbaar op: https://www.engineeringtoolbox.com/air-properties-d_156.html.

Appendix A LITERATURE STUDY

A.1 Bone structure

This paragraph is meant to clarify the bone structure and specific terminology in order to gain more understanding about bone regeneration.

Bones can be divided into four categories: long bones, short bones, flat bones and irregular bones. Flat bones are formed by membranous bone formation, meaning the bone is formed from membrane fibrous tissue or mesenchyme. Long bones are formed from membranous bone- as well as endochondral bone-formation, this formation is derived from cartilage cells. [58], [59]

The main purposes of bones are structural and metabolic, achieved when preserving a skeletal **extracellular matrix (ECM)**. E.g. storing and healing cells, induce body movement and maintain mineral homeostasis. Because of their complexity it is important to locate the bone structure on a scale in order to discuss them. [1], [4], [58], [60]

A.1.1 Hierarchical structure of the bone

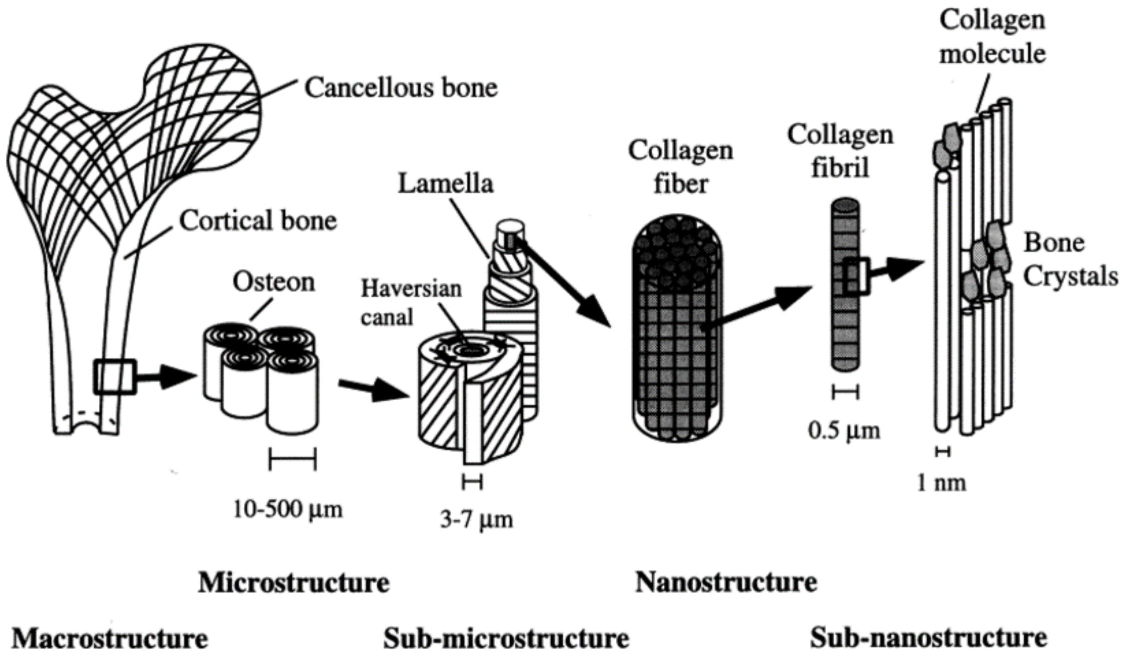

Figure A-6.7-1 Hierarchical structural organization of bone [60]

A.1.1.1 *Macrostructure*

The bone is at macrolevel made out of **cortical** (or **compact**) and **cancellous** (or **trabecular**) tissue type. Long bones are divided into three parts, a hollow shaft (**diaphysis**), the head at both ends (**epiphysis**) and in-between the **metaphysis**. The epiphysis and metaphysis have a dense cortical shell with porous, honeycomb-like network, cancellous bone on the inside as to the diaphysis which is made up of dense cortical bone. Flat bones have dense cortical layers as outer surface and a thin cancellous structure at the interior. Cancellous bone had a porosity of 50-90 vol% while the cortical bone has a porosity of 10 vol% and is less metabolically active. The ratio (in the case of an adult) is 80% cortical bone and 20% cancellous bone. [58], [60], [61]

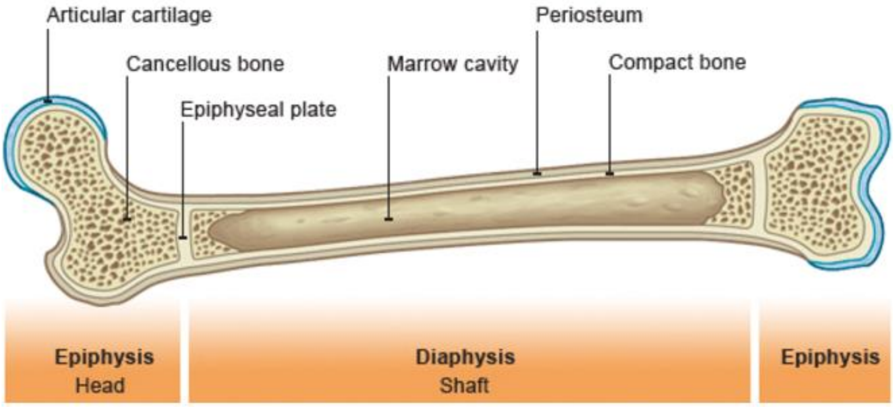

Figure 2-6.7-2 composition of a long bone [8]

A.1.1.2 *microstructure and sub-microstructure*

Lamellae sheets (3 -7 µm in width) are **mineral collagen fibers** and may occur in concentric layers around a central canal, called the Haversian system, this cylindrical structure is then called a cortical osteon or (200- 250 µm in diameter) and form a branching network in the cortical tissue. In case lamellae sheets do not follow a specific pattern they are called woven bone. A third possibility is that the lamellae are more tangent towards the outer layer of the bone, together with the woven bone tissue they are called lamellar bone, are thick layered (159 – 300 µm) and wrap around the bone. Trabecular bone on the other hand is composed of a trabeculae framework following a cellular structure. [58], [60]

A.1.1.3 *Nanostructure and sub-nanostructures*

This scale is represented by collagen fibers including the mineral in and around the fibers. The accent locations macromolecules attach to the collagen fibers is unclear. Sub-nanostructures are crystals, collagens and non-collagenous organic proteins. Spaces between collagen fibers are occupied by apatite crystals of bone. Impurities occur within the bone apatite, e.g. HPO_4, Na, Mg, carbonate, K among others. Organic proteins are mainly Type I collagen which make up a matrix, they are secreted by osteoblasts and form a tertiary structure of fibers. Examples of non-collagenous organic proteins are osteopontin, osteonectin and osteocalcin. These proteins fulfill functions such as regulating size and orientation of the mineral deposits as well as a reservoir for calcium or phosphate ions. [60]

A.1.1.4 *Bone formation and growth*

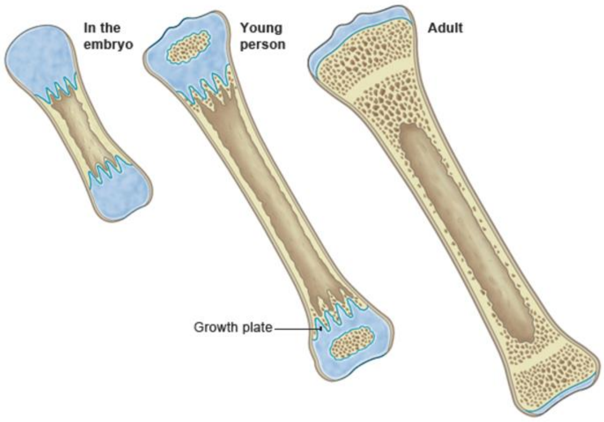

Figure 2-6.7-3 Bone growth [8]

Throughout childhood and adolescence radial and longitudinal growth takes place. This last one occurs at the growth plates where cartilage expands in the epiphyseal and metaphyseal areas of the long bones and in time mineralizes to form new bone.

Bones respond to mechanical forces or physiological changes, the bone then changes its shape. This called modeling and can also take place throughout adulthood. Bone tissue can be removed or added, osteoblasts and osteoclasts are responsible for these actions.

Remodeling, which takes place continuously regardless of age, helps the bone assure its strength and mineral homeostasis. It could occur at random or it could respond to tissue that needs to be repaired (but can be undermined in the case of a serious injury or such). [4] Remodeling is similar in cancellous and cortical bone. The process involves removing packages of old bone and replacing them with a new matrix consisting of protein which then mineralizes to form new bone. Here as well a group of osteoclasts and osteoblasts are responsible for the process. This process will be discussed in more detail as it represents the bone healing process.

There are four cycles to remodeling, in sequence being activation, resorption, reversal and formation. Osteoclast, osteoblast and osteocyte cells play a key role in this process. In the activation phase mononuclear **osteoclast** are recruited and activated from the circulation and fuse to form multinucleated **preosteoclasts**. These preosteoclasts bind to the bone matrix

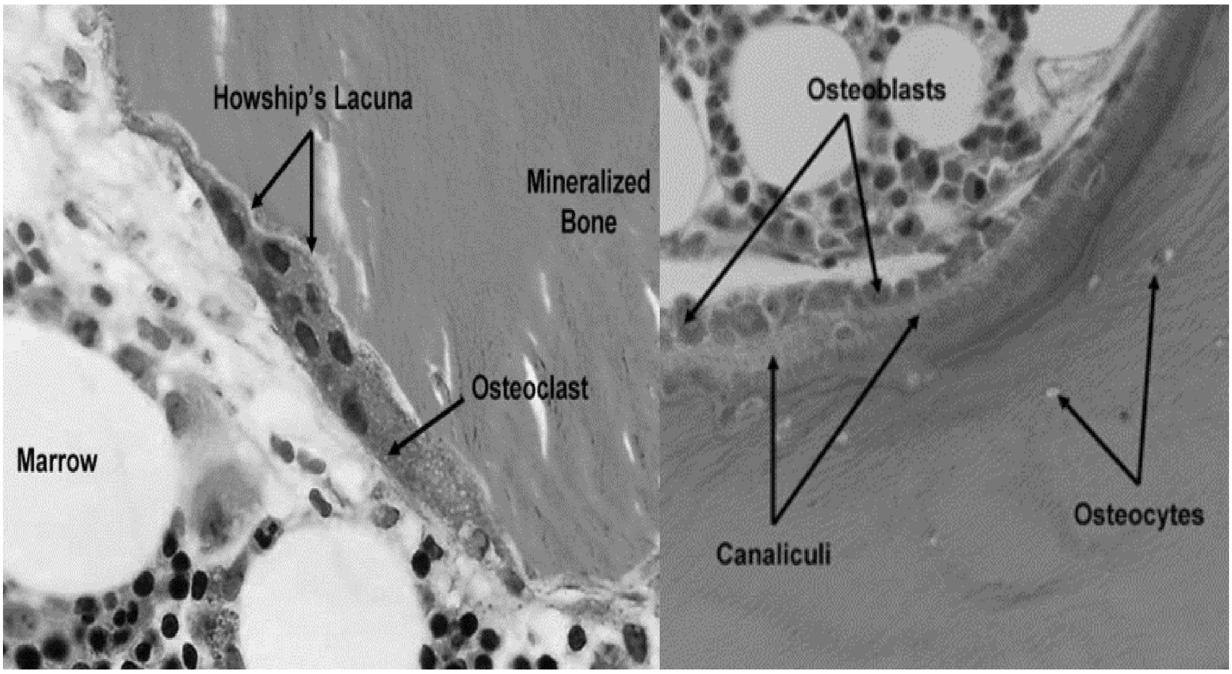

through interaction between transmembrane receptors. During a remodeling cycle osteoclast stimulated resorption (breaking down of bone tissue) takes about two to four weeks.

Figure 2-6.7-4 Osteoclasts resorb bone to form Howship's Lacuna (left), osteoblasts manufacturing new organic matrix (right) [58]

During the resorption phase the organic matrix is digested through secretion produced by the **osteoclasts**, causing formation of what is called Howship’s lacunae located on cancellous bone surface and Haversian canals in cortical bone. The phase is ended by apoptosis of the multinucleated osteoclasts. The transition between resorption and formation is called the reversal phase where **preosteoblasts** are recruited (**osteoinduction**). The formation phase can take up to six months to complete. **Osteoblasts** manufacture a new organic matrix (**osteogenesis**) and take maintenance over the mineralization, the surrounding osteoblasts become an osteocyte network which connects to the surface of the bone. At the end of the phase most of the remaining osteoblasts undergo apoptosis (50 -70%). When all four stages are completed a new osteon has emerged. [58]

A.2 Bioprinting techniques

A.1.2 Inkjet bioprinting

Inkjet printing is the most well-known form of droplet-based bioprinting, where a nozzle layers picolitre droplets on a substrate without any contact between the two. [11] This technique was one of the first AM processes and there are currently four different types available: electrostatic, acoustic, thermal and piezoelectric inkjet printing. Inkjet printing is quite popular, specially the last two mentioned types, thanks to the low cost and fast printing speed.

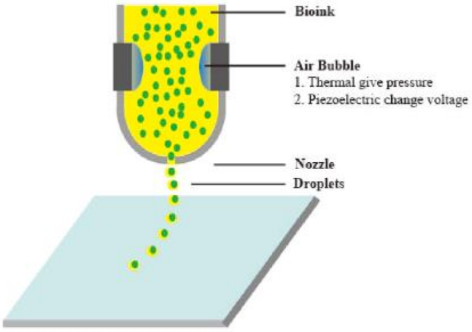

Figure 2-6 Inkjet bioprinting [4]

Thermal inkjet printing relies on high pressured air bubbles generated by heating patterns (up to 300°C) to eject ink droplets by overcoming the surface tension at the nozzle. Although the process is efficient and approaches a uniform distribution for the printed cells, there are still certain flaws. Because of the low stiffness of the hydrogel the shape are mostly irregular and the direction of the droplets are difficult to control.

Piezoelectric inkjet printing is less favorable for bioprinting then its thermal counterpart. It uses voltage with certain frequencies instead of heat to apply pressure, the frequencies used in this process could damage the cells. [4]

A.1.3 Laser-assisted bioprinting

In general there are four parts a laser-assister printer consists of: a laser source, a focusing tool, a substrate and a metallic ribbon film. The ribbon film is divided in a donor layer with an energy absorbing layer at the bottom, this last one responds to the laser pulse. [4] The energy absorbing layer locally heats up and creates a high pressure bubble while part of the donor layer evaporates. The bioink will then fall onto the substrate and at the same time be crosslinked. [11]

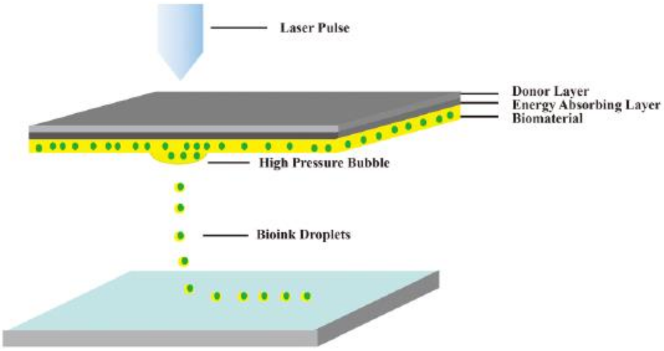

Figure 2-7 Laser-assisted bioprinting [4]

The technique allows the surface properties to be optimized and the cell viability is high, however the process is time consuming and has a relatively high cost. Moreover the laser could potentially damage the cell. [4]

A.1.4 Stereolithography

This technique photolytically crosslinks bioinks with laser or digital projector as a light source and does this layer by layer. Stereolithography provides a high resolution, high cell viability and is a fast process. [11]

A.1.5 Integrated bioprinting [11]

As discussed earlier (paragraph *strategies for tissue engineering*) 3D bioprinting of hydrogels lacks mechanical strength. In order to overcome this problem hybrid techniques have been enhanced. For example a cell-laden hydrogel in combination with a synthetic biopolymer can be printed in a hybrid manner and are able to construct a tissue with a significant amount of mechanical stress.

A.3 Cell sources

The importance and influence of the bioprinting technique as well as the bioink has been discussed in previous chapters. However the chosen cell type(s) are also of significance and apart from its primary functions there are cell types that offer a structural and supportive function. Furthermore cells can also be involved in the vascularization process and provide an environment for stem cells differentiation and maintenance. The main objective is to mimic the *in vivo* biological state of cells with the idea that the cells fulfill their in vivo functions.[7]

Cell viability is a result of the proliferation of the chosen cell type (in combination with the printing parameters and hydrogel properties as discussed earlier). Stimulating proliferation enhances cell viability, however there is a limitation as hyperplasia and apoptosis can be a result of excessive proliferation. Timing is also crucial, at first the construct must be populated, so proliferation must be high enough. In the long term (*in vivo*) proliferation needs to be stable in order to attain tissue homeostasis.[7]

Appendix B STUDY OF HYDROGEL MATERIAL

B.1 Hydrogel preparation protocols

Equipment

The following equipment is necessary:

- Gelatin (bovine skin type B)
- Purified water (Milli-Q water)
- Volumetric flasks (50 ml, 10 ml)
- Beakers
- Volumetric pipette (10ml)
- Heated bath with bowl, water, thermometer and heater
- Spatula
- Steering magnets
- Analytical balance (0,1 mg accuracy)
- Parafilm

Protocol 15 w/v% gelatin

- 7.5 gram gelatin is weighed and added to a 50 ml volumetric flask.
- (Purified) water is added to the volumetric flask so that the center of the concave meniscus is in line with the 50 ml mark.
- The mixture is brought into a heated bath at ± 60°C and is steered with a magnet for ± 35min. Parafilm is used to cover the top of the flask.

Protocol 20 w/v%, 15 w/v%, 10 w/v%

20 w/v% gelatin

- 10 gram gelatin is weighed and added to a 50 ml volumetric flask.
- (Purified) water is added to the volumetric flask so that the center of the concave meniscus is in line with the 50 ml mark.
- The mixture is brought into a heated bath at ± 60°C and is steered with a magnet for ± 35min. Parafilm is used to cover the top of the flask.

15 w/v% gelatin

- 20ml is extracted from the 20w/v% gelatin using a 10ml volumetric flask.
- Using a volumetric pipette, 6.67 ml water is added to the 10ml solution in a beaker.
- The now 15w/v% solution is steered with a magnet in the heated bath for another ± 15min.

10 w/v% gelatin

- 20ml is extracted from the 20w/v% gelatin using a 10ml volumetric flask.
- Using a 10ml volumetric flask, 20ml water is added to the 20ml solution in a beaker.

- The now 10w/v% solution is steered with a magnet in the heated bath for another ± 15min.

Protocol 5 w/v%, 15 w/v%

15 w/v% gelatin

- 7.5 gram gelatin is weighed and added to a 50 ml volumetric flask.
- (Purified) water is added to the volumetric flask so that the center of the concave meniscus is in line with the 50 ml mark.
- The mixture is brought into a heated bath at ± 60°C and is steered with a magnet for ± 35min. Parafilm is used to cover the top of the flask.

5 w/v% gelatin

- 20ml is extracted from the 15w/v% gelatin using a 10ml volumetric flask.
- Using a 10ml volumetric flask, 40ml water is added to the 20ml solution in a beaker.
- The now 5w/v% solution is steered with a magnet in the heated bath for another ± 15min.

B.2 Protocol mold manufacturing

In order to be able to provide the right geometry of the samples a mold is necessary. I had the idea to manufacture a silicon mold ourselves as ordering molds from the US will take an excessive amount of time. Lore provided a 3D printed case and metal disks (35mm in diameter and 2mm thick). I provided the Silicon (*Siliconen condensatie 20)* and poured the mold on 16.03.2018 using the following protocol:

- The metal disks were glued (with superglue) to the case to make sure there is no movement of the disks possible during the process.
- The amount of silicon needed was calculated based on the volume of the case, this was 75 ml. The silicon used was *Siliconen condensatie 20*.
- To the base material (the silicon itself) 1.5% of a B component was added (an unknown monomer as this information is a company's trade secret). 1.5% was chosen because this amount gives air bubbles the time to escape and has a slow and steady hardening process.
- Vibrations were induced to allow bubbles inside the material to rise to the top.
- The hardening will take over 24h as this is a slow process.

B.3 DSC tests results

B.3.1 Data DSC tests

10 w/v%	cool			heat		
	start (°C)	peak (°C)	peak area (J/g)	start (°C)	peak (°C)	peak area (J/g)
	19.37	16.28	0.06521	32.71	33.97	0.7909
	19.7	15.77	0.261	32.5	34.7	0.8124
	19.92	15.49	0,005768	32.1	35.62	0.6205
	20.65	14.75	0.09868	33.9	34.51	1.113
	21.98	14.59	0.07433	33.19	35.22	0.6116

15 w/v%	cool			heat		
	start (°C)	peak (°C)	peak area (J/g)	start (°C)	peak (°C)	peak area (J/g)
	22,6	16.49	0.309	31.27	35.87	1.362
	24,7	16.51	1.023	31.94	35.46	1.888
	23,94	16.89	0.6214	33.39	35.49	2.295
	24,4	18.48	0.1289	35.82	37.12	1.43
	23,79	17.7	0.7566	33.92	38.23	1.155

20 w/v%	cool			heat		
	start (°C)	peak (°C)	peak area (J/g)	start (°C)	peak (°C)	peak area (J/g)
	24.04	18.4	0.411	3.,9	34.73	1.775
	22.38	19.34	0.853	33.24	35.76	2.764
	23.97	17.55	0.2607	31.68	36.03	2.129
	24.63	18.97	0.7873	31.78	35.95	1.786
	25.47	17.66	0.8127	33.08	35.59	1.737

B.3.2 Graphs DSC tests

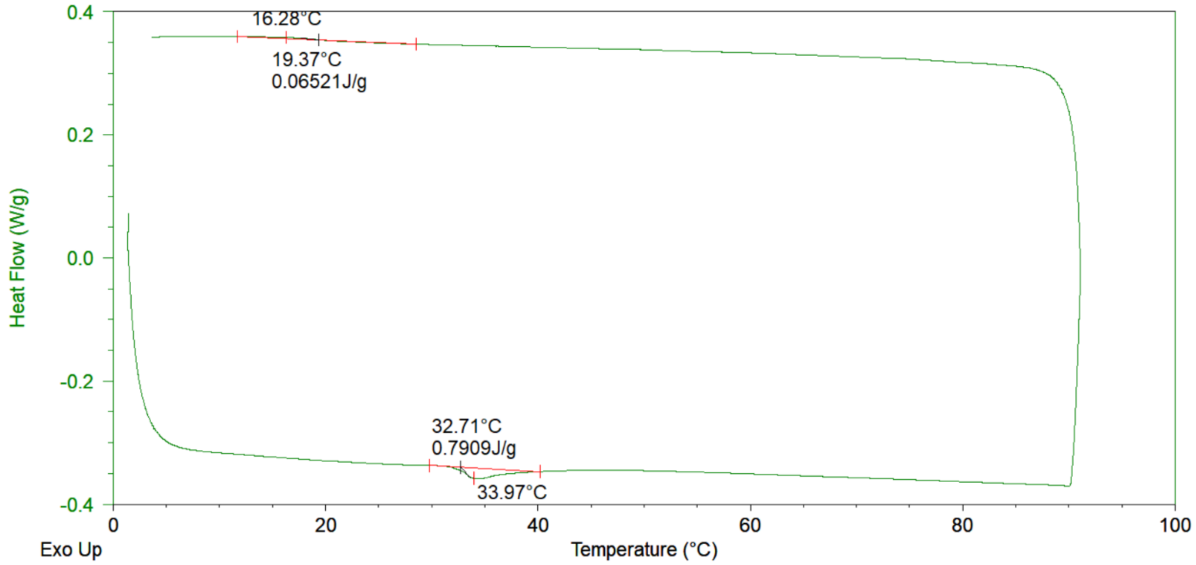

Figure 6.7-5 DSC test 10 w/v% run 1

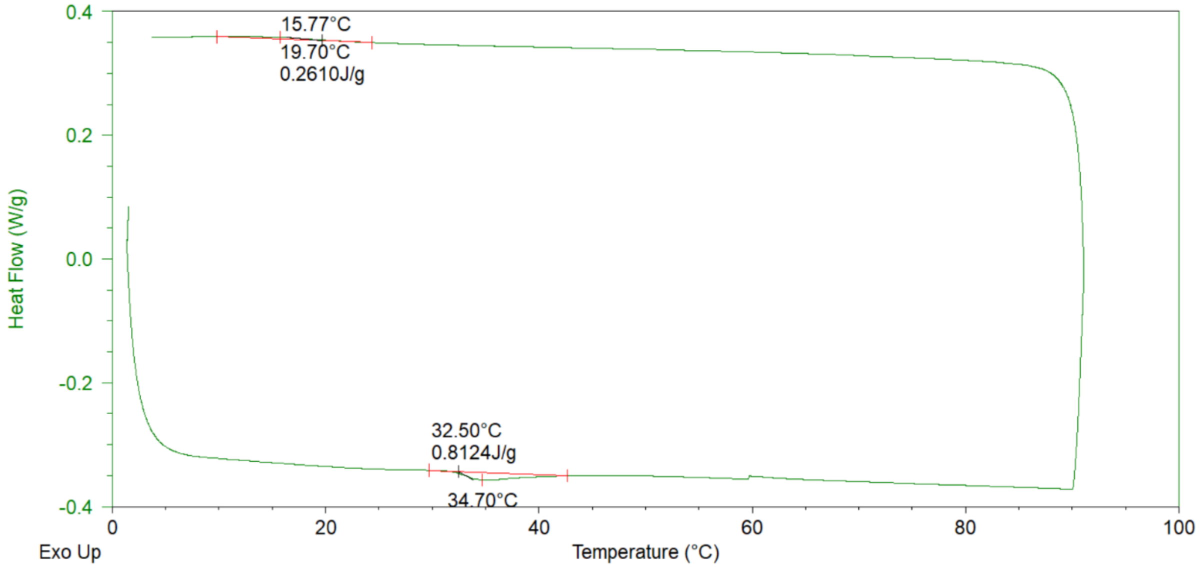

Figure 6.7-6 DSC test 10 w/v% run 2

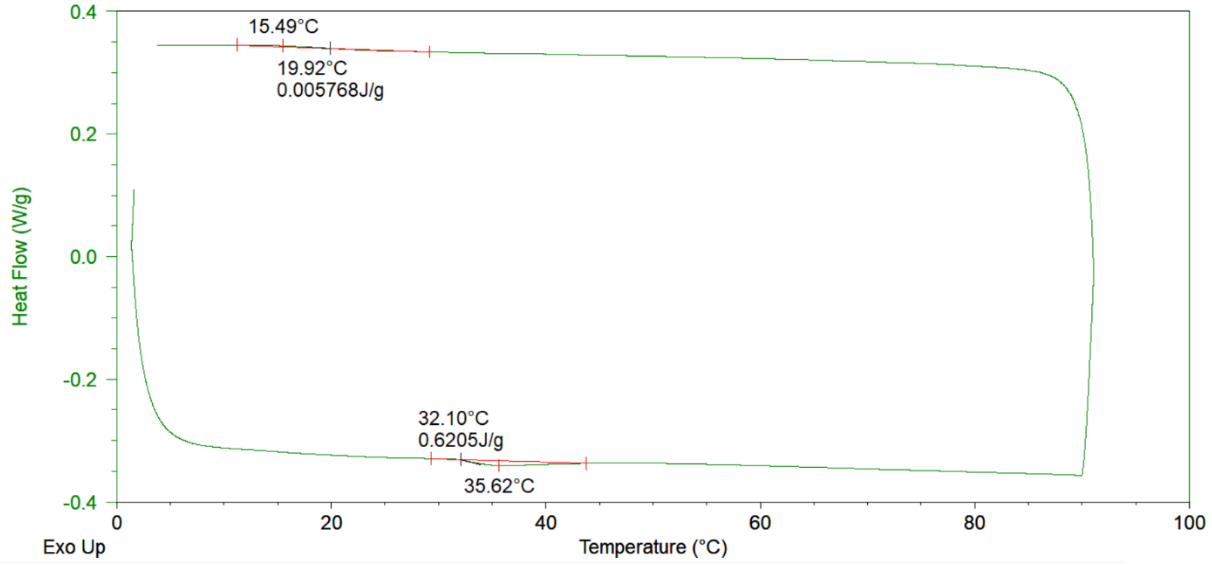

Figure 6.7-7 DSC test 10 w/v% run 3

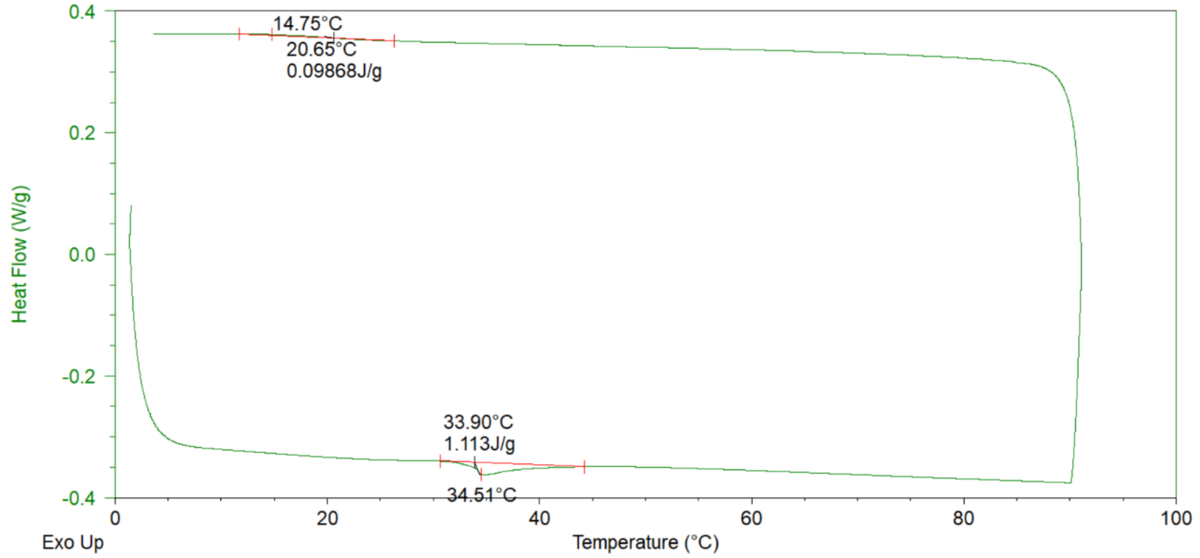

Figure 6.7-8 DSC test 10 w/v% run 4

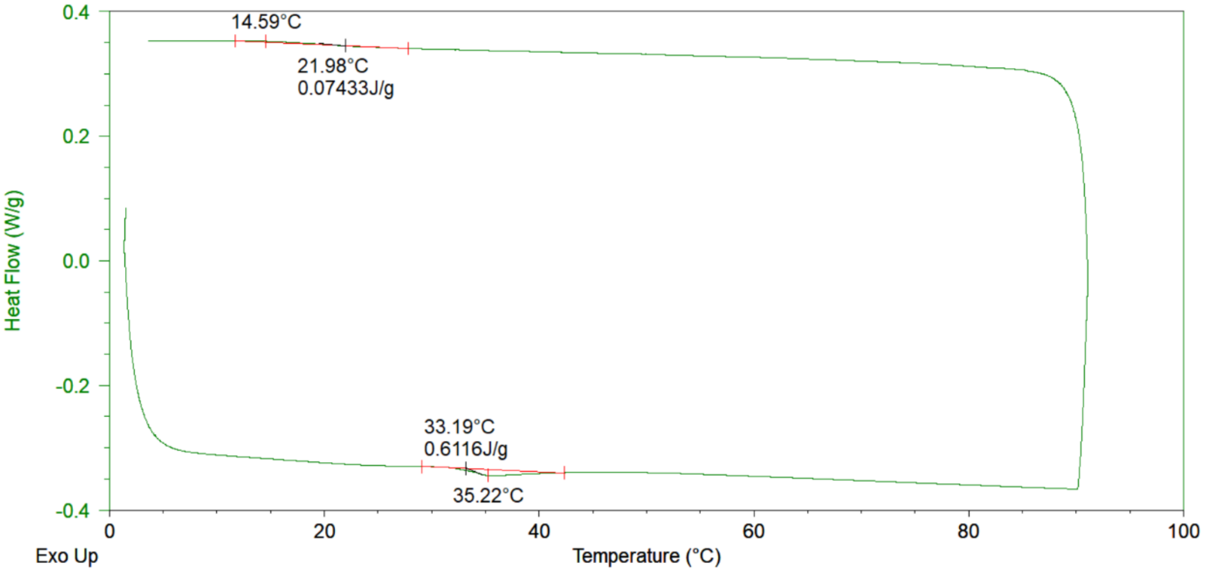

Figure 6.7-9 DSC test 10 w/v% run 5

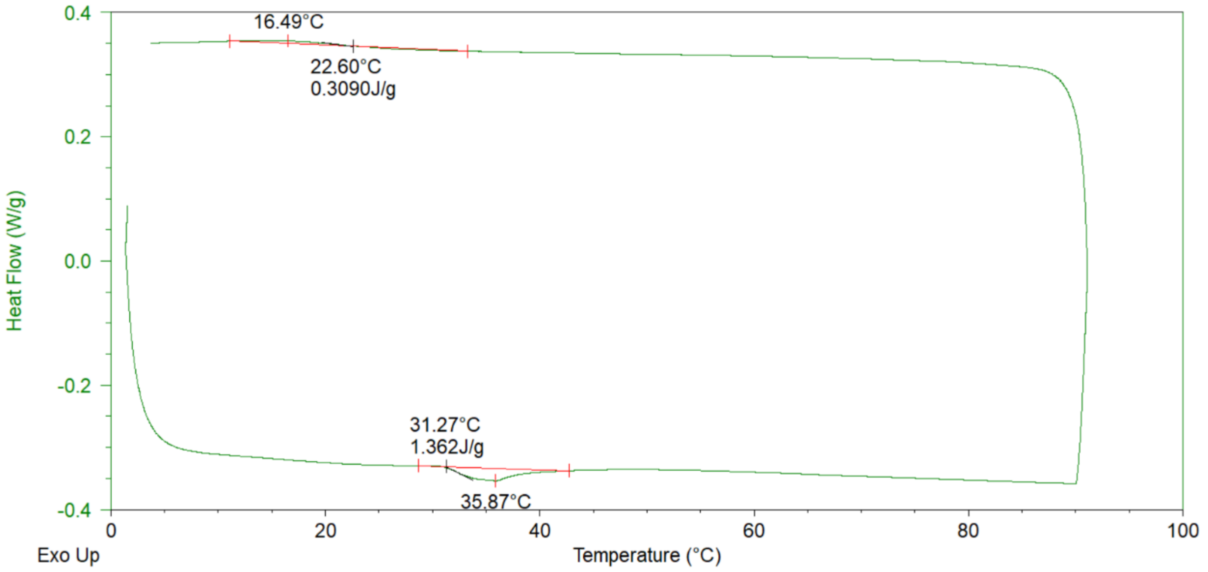

Figure 6.7-10 DSC test 15 w/v% run 1

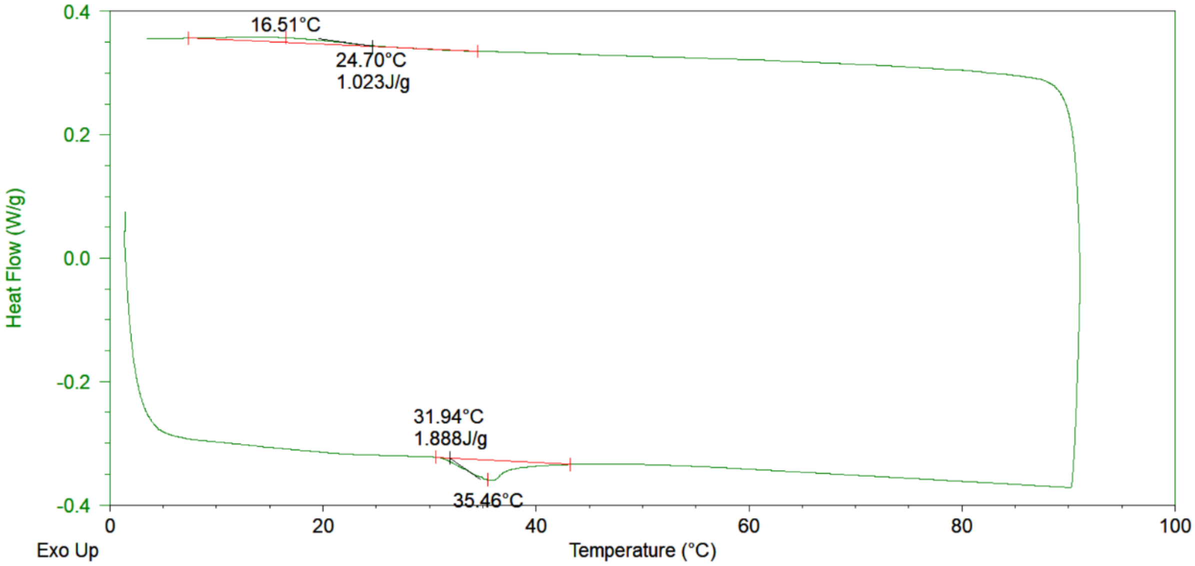

Figure 6.7-11 DSC test 15 w/v% run 2

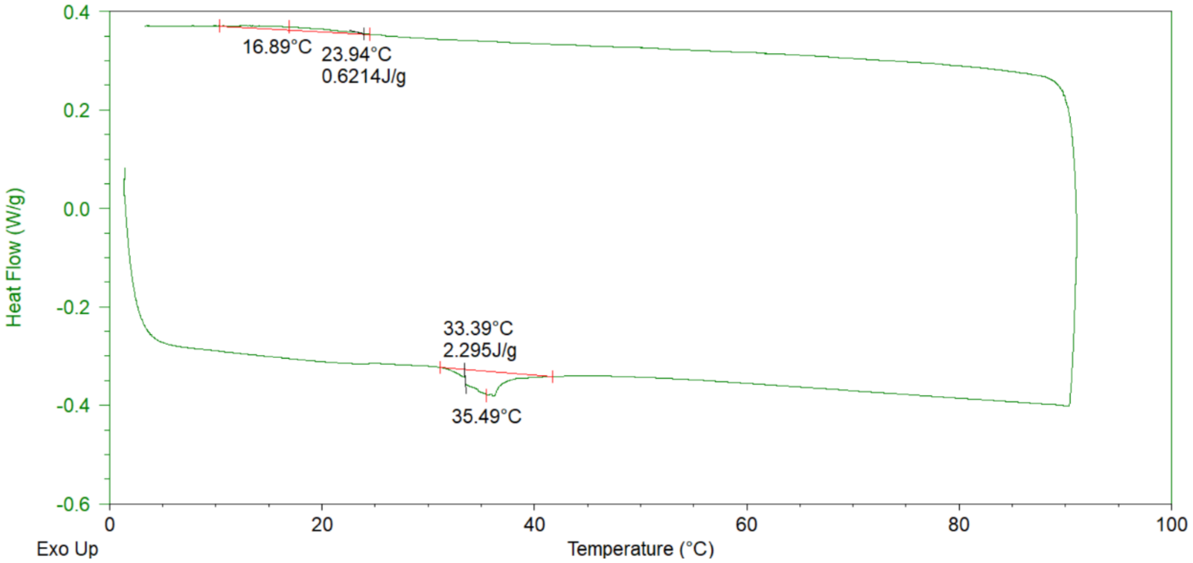

Figure 6.7-12 DSC test 15 w/v% run 3

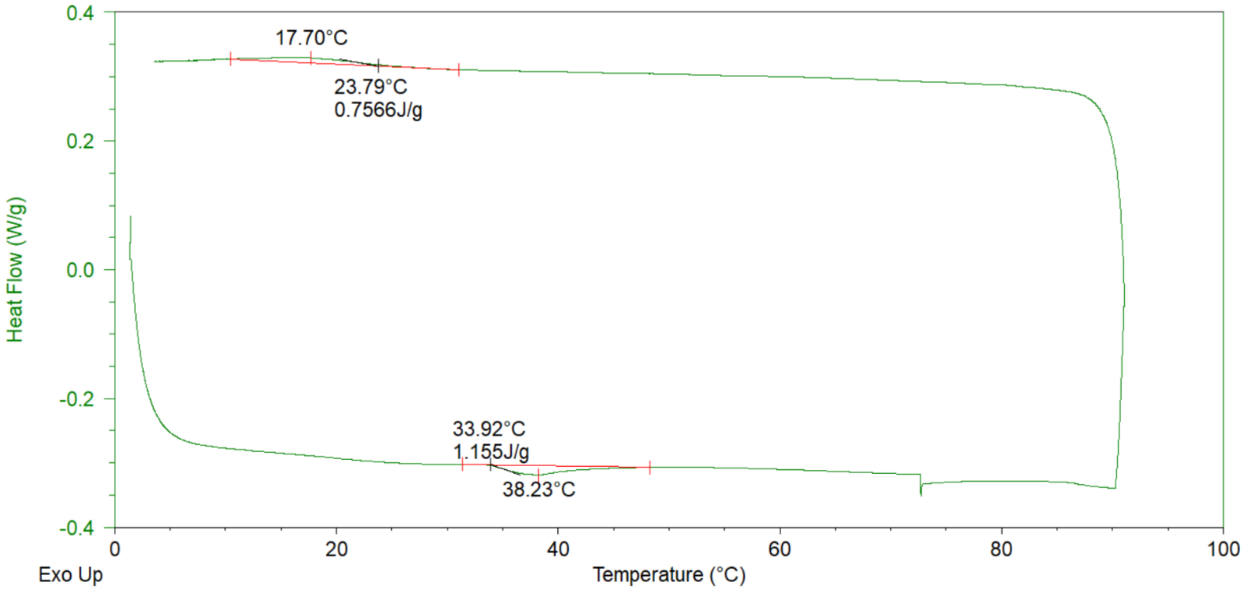

Figure 6.7-13 DSC test 15 w/v% run 4

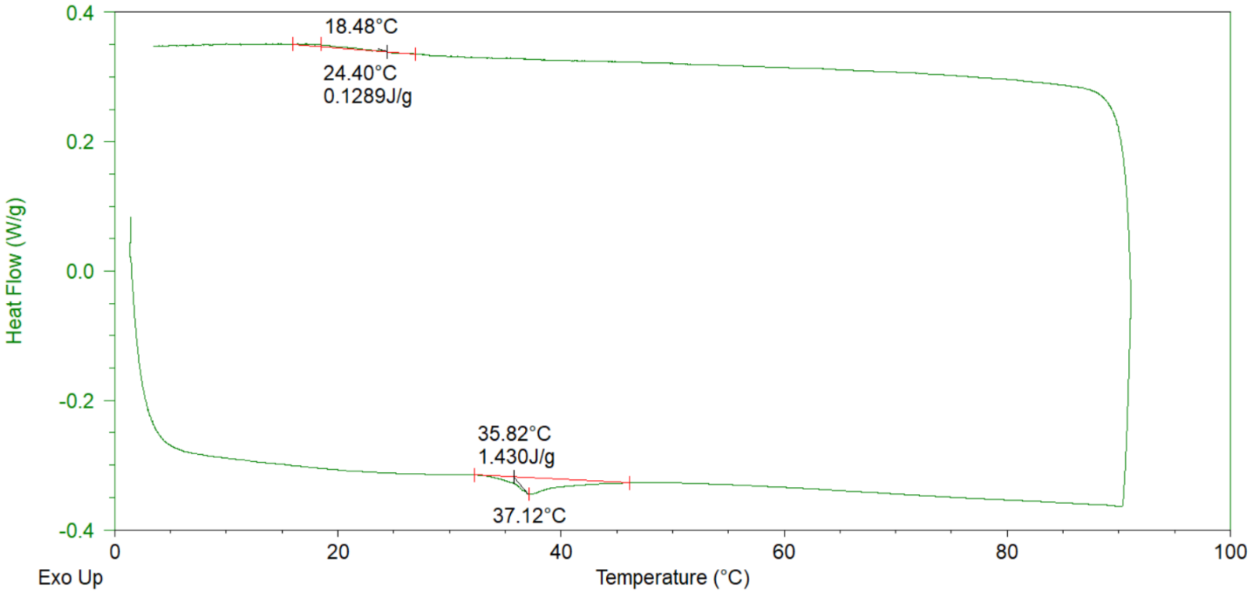

Figure 6.7-14 DSC test 15 w/v% run 5

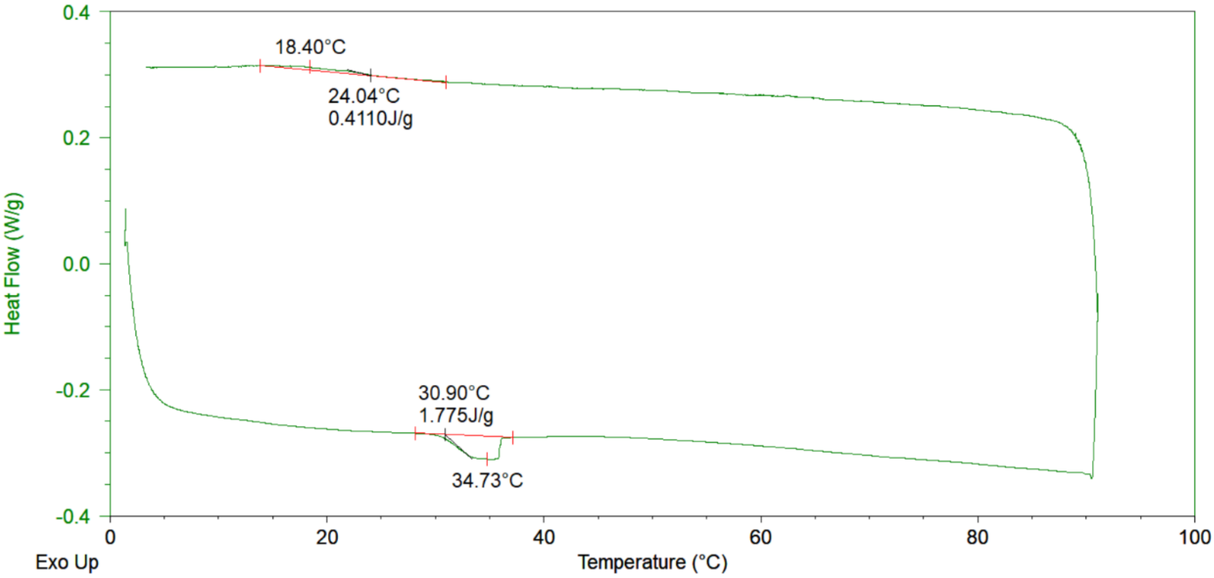

Figure 6.7-15 DSC test 20 w/v% run 1

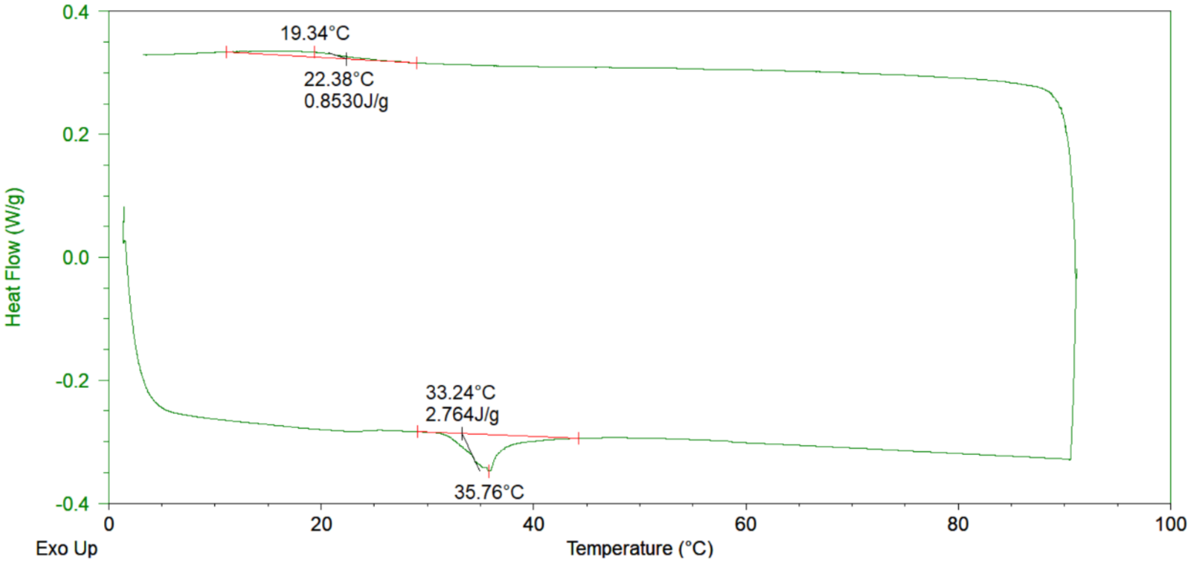

Figure 6.7-16 DSC test 20 w/v% run 2

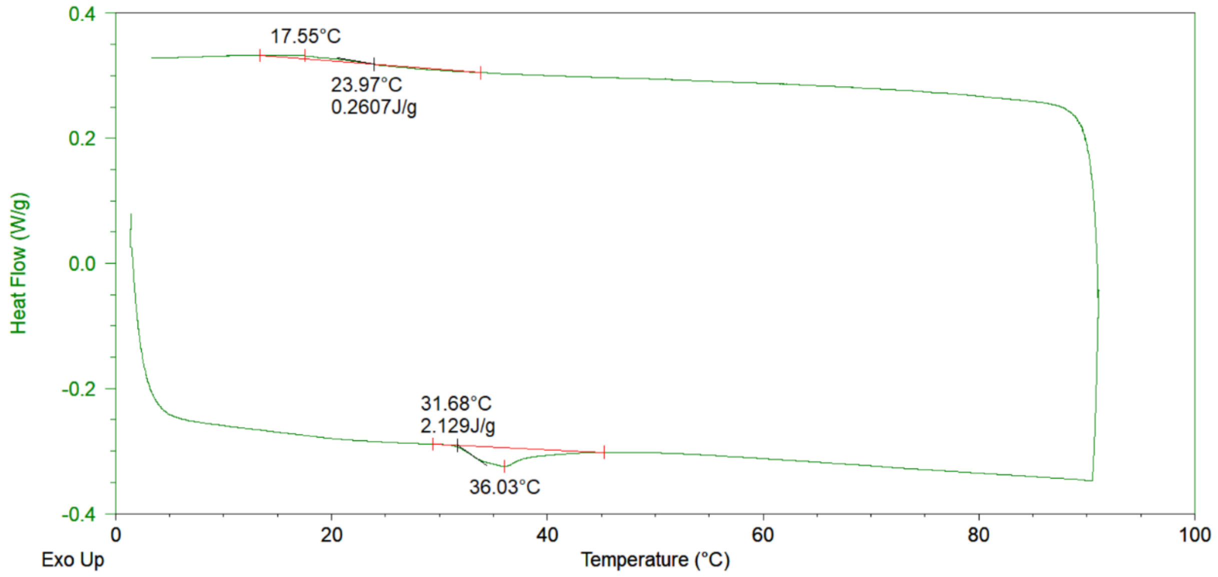

Figure 6.7-17 DSC test 20 w/v% run 3

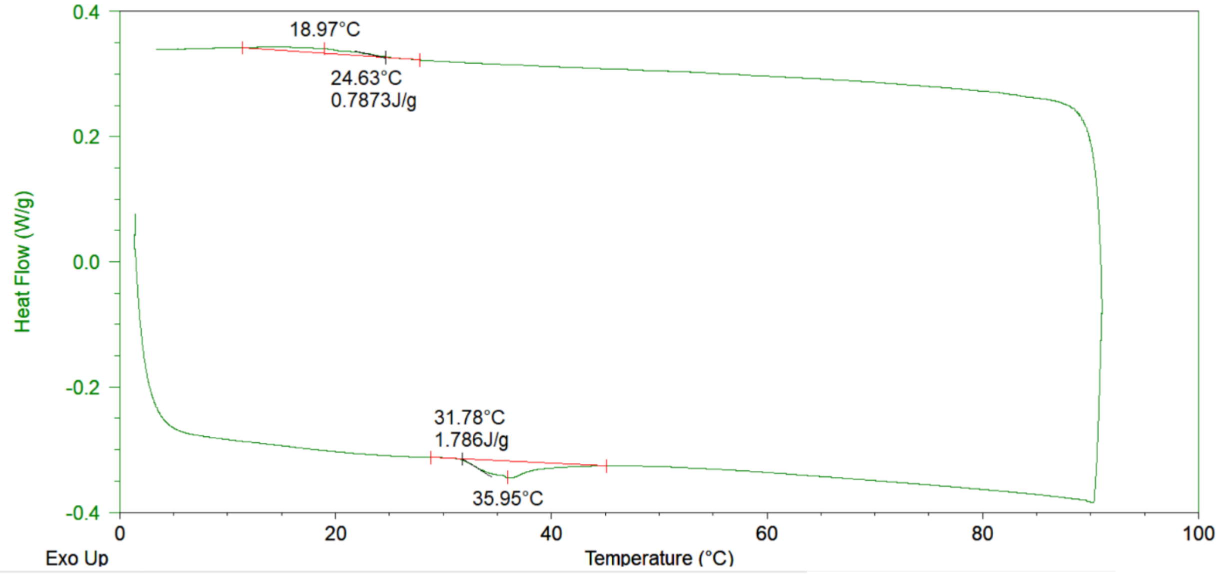

Figure 6.7-18 i DSC test 20 w/v% run 4

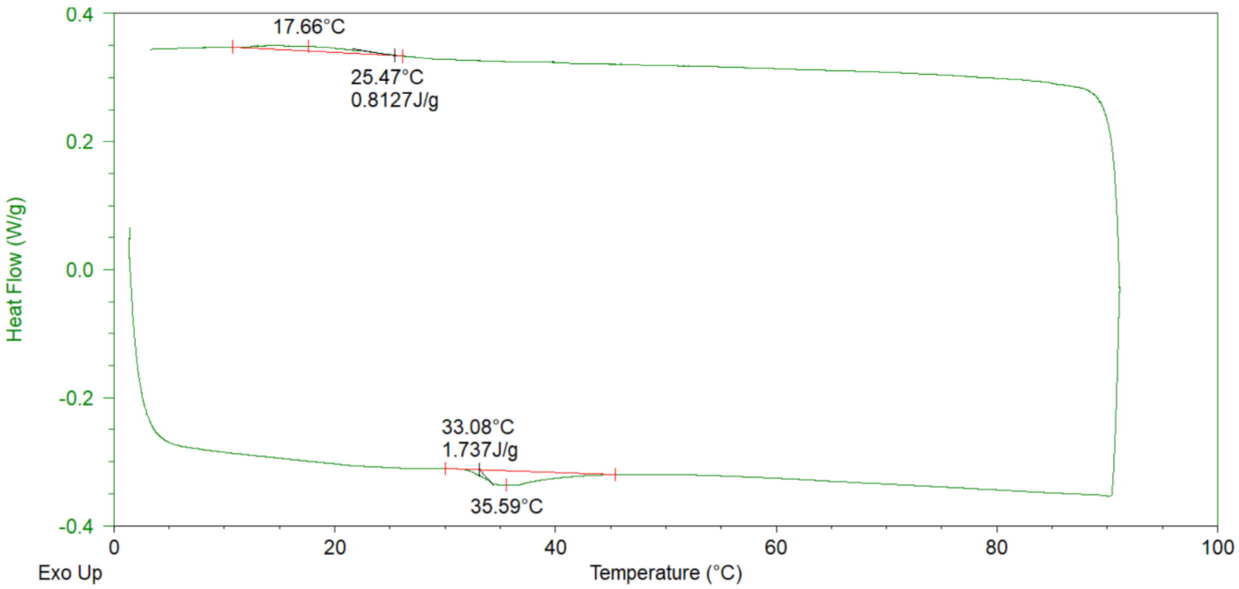

Figure 6.7-19 DSC test 20 w/v% run 5

B.4 Results microscopy gelatin

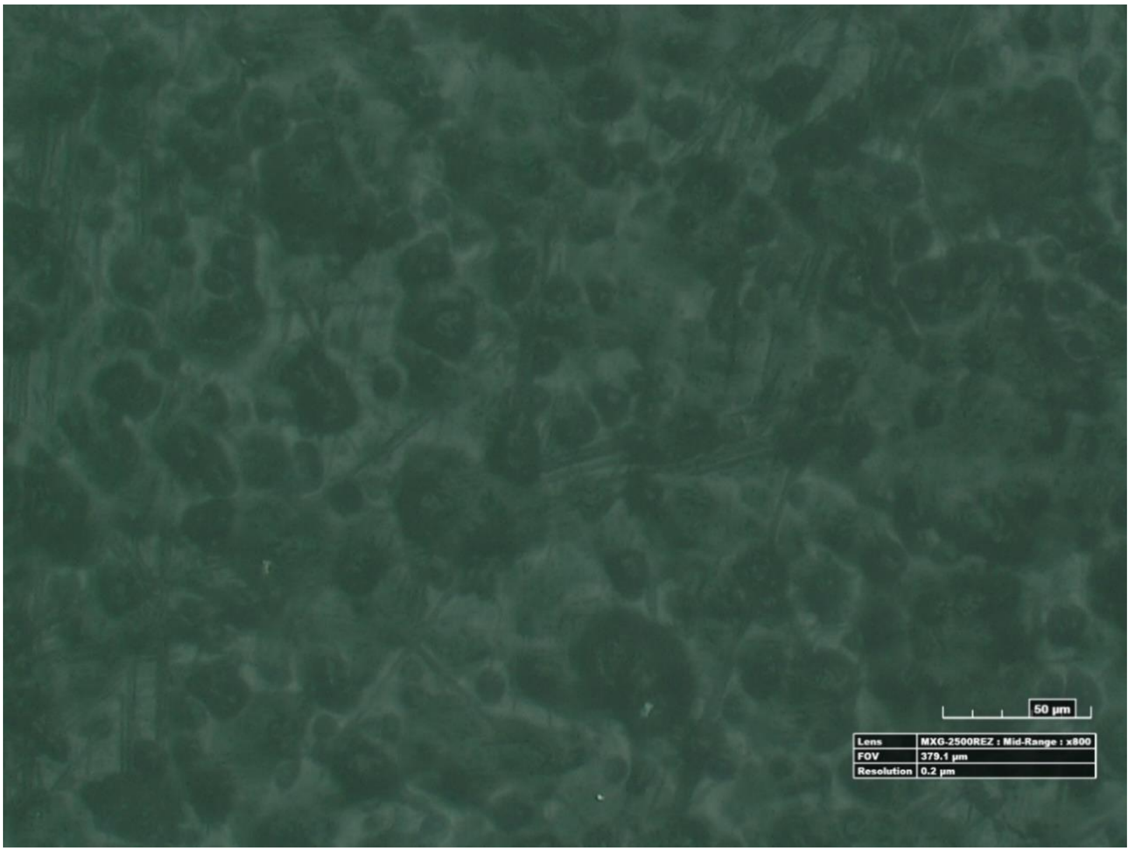

Figure 6.7-20 Microscopic image gelatin 10 w/v% (Magnification x800, FOV 379.1 µm, resolution 0.2 µm)

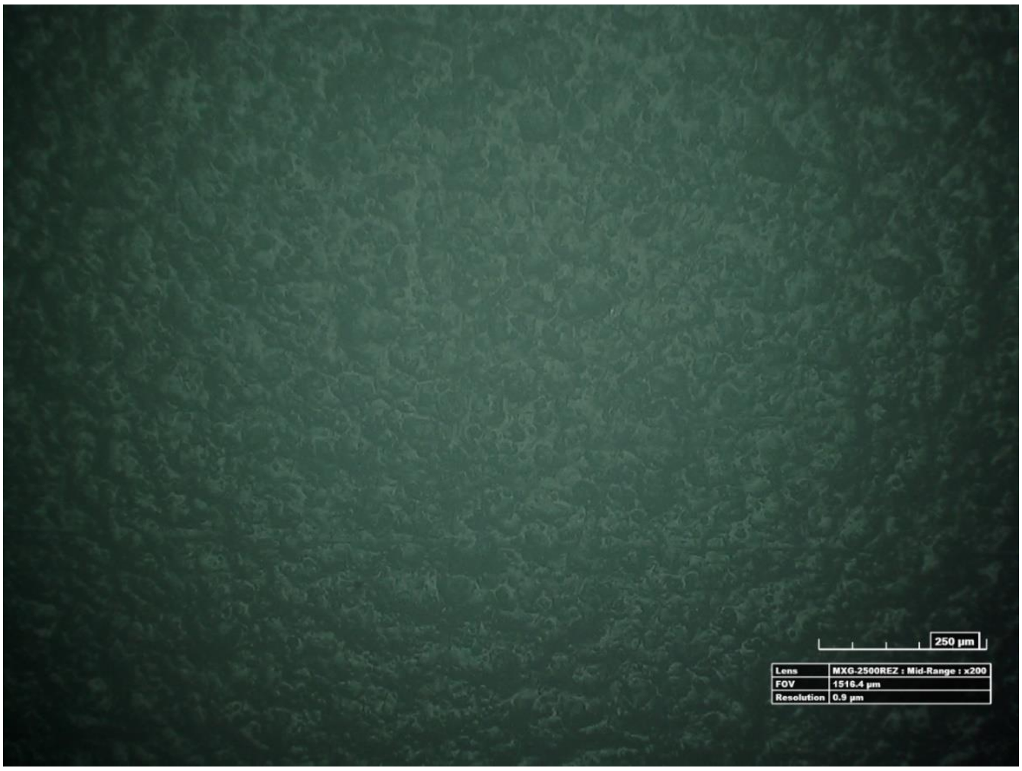

Figure 6.7-21 Microscopic image gelatin 20 w/v% (Magnification x200, FOV 1516.4 µm, resolution 0.9 µm)

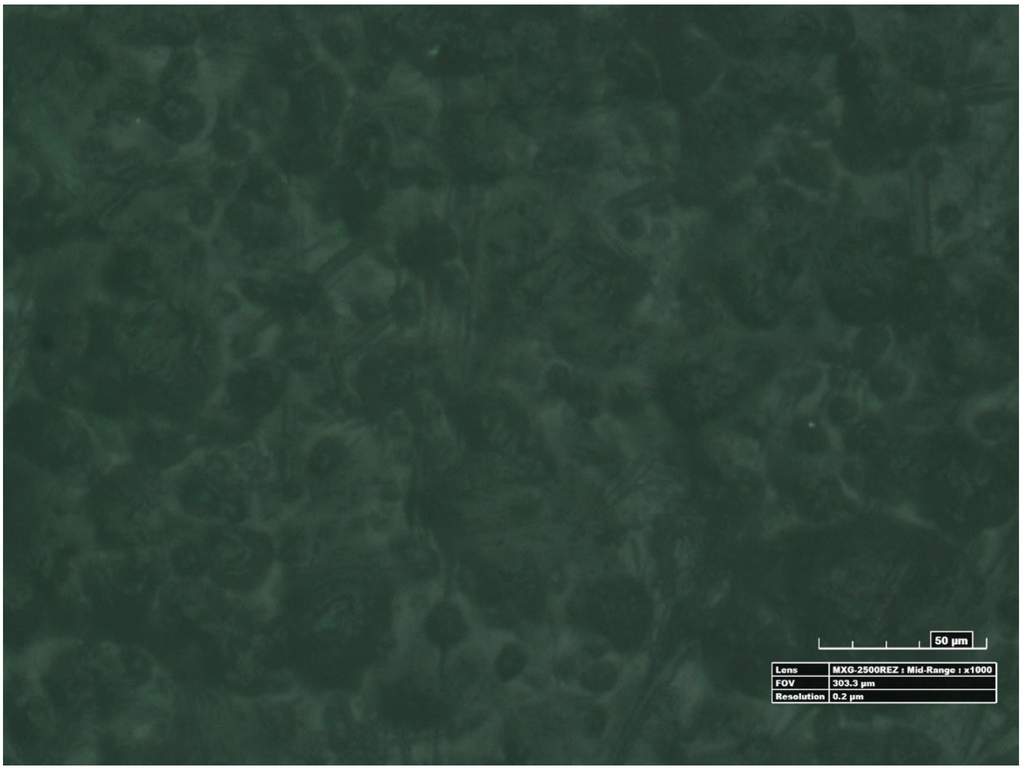

Figure 6.7-22 Microscopic image gelatin 15 w/v% (Magnification x1000, FOV 303.3 µm, resolution 0.2 µm)

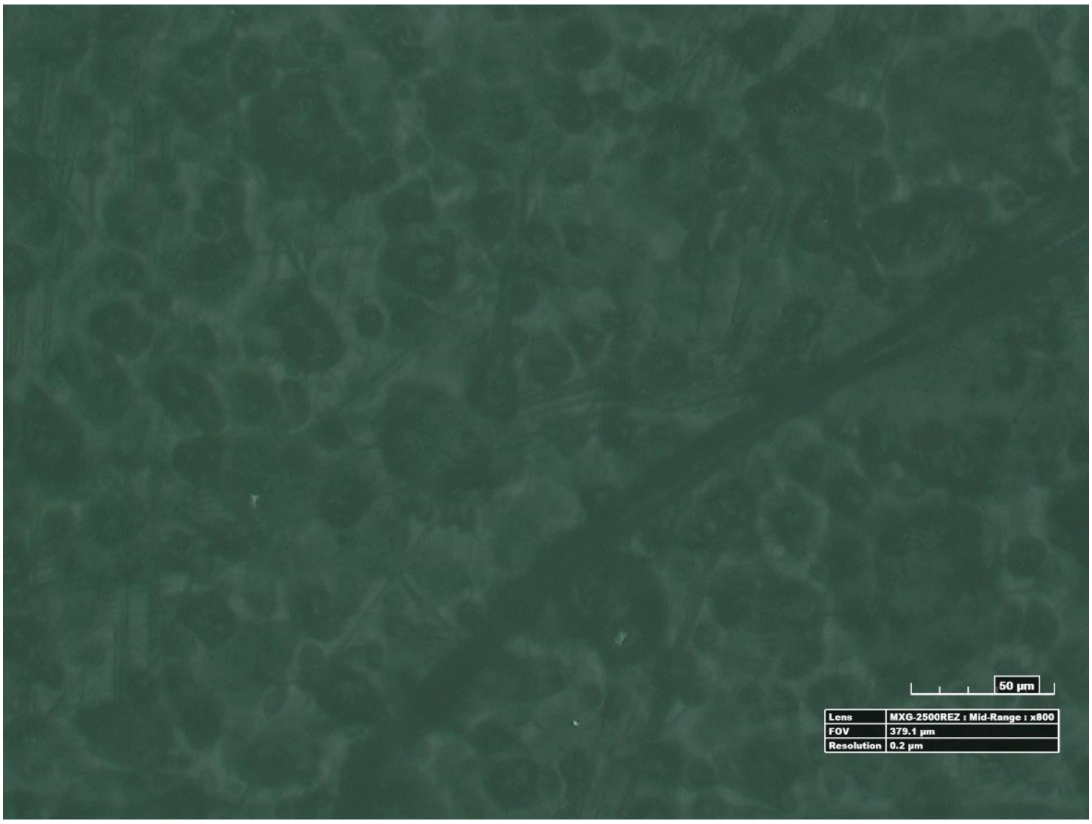

Figure 6.7-23 Microscopic image gelatin 20 w/v% (Magnification x800, FOV 379.1 µm, resolution 0.2 µm)

B.5 EDS HA nanopowder

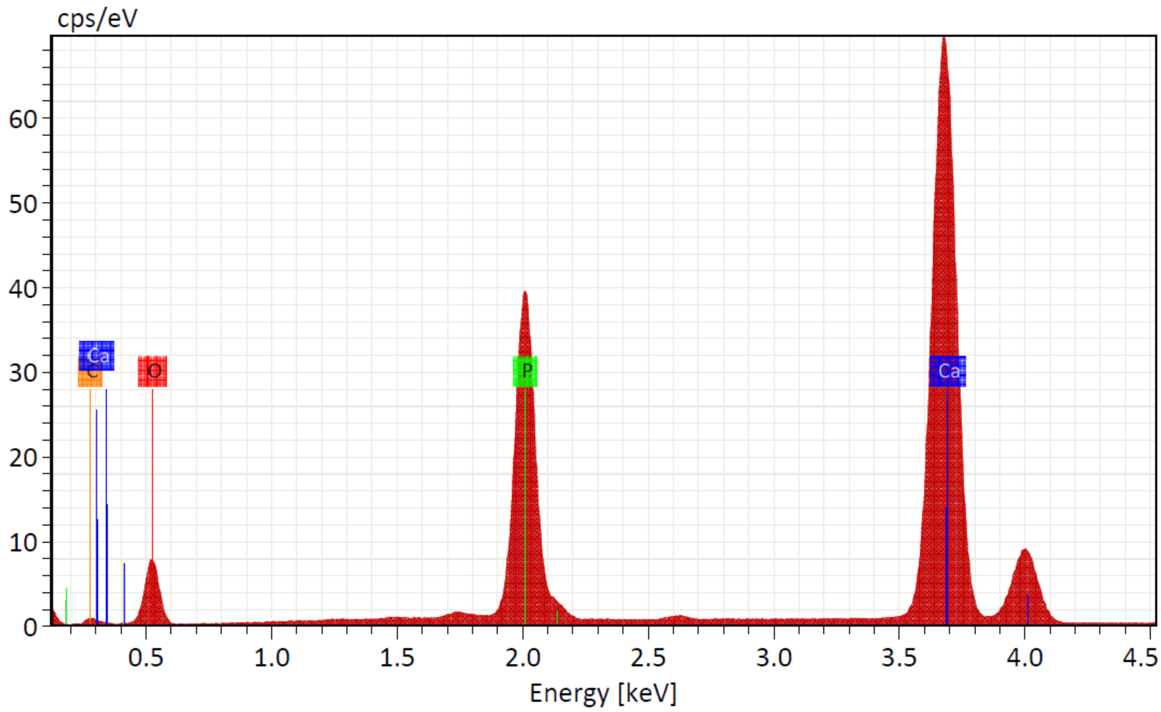

Figure 6.7-24 EDS results HA nanopowder

Table 6.7-1 EDS results HA nanopowder

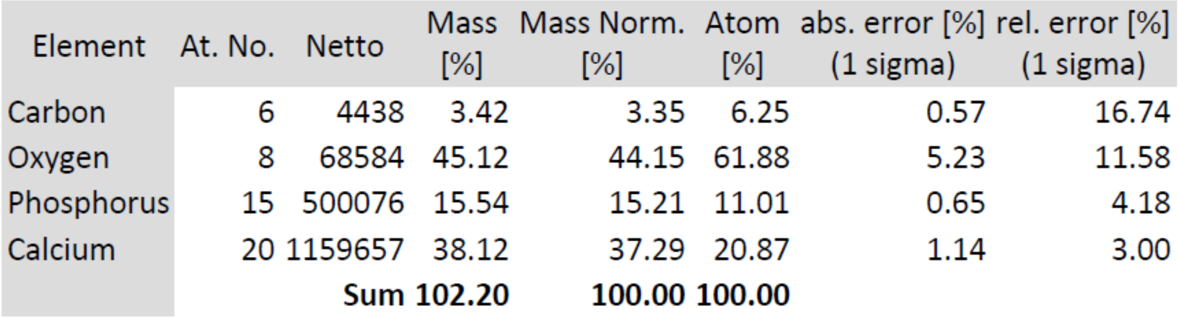

Element	At. No.	Netto	Mass [%]	Mass Norm. [%]	Atom [%]	abs. error [%] (1 sigma)	rel. error [%] (1 sigma)
Carbon	6	4438	3.42	3.35	6.25	0.57	16.74
Oxygen	8	68584	45.12	44.15	61.88	5.23	11.58
Phosphorus	15	500076	15.54	15.21	11.01	0.65	4.18
Calcium	20	1159657	38.12	37.29	20.87	1.14	3.00
		Sum	**102.20**	**100.00**	**100.00**		

B.6 Rheology

B.6.1 Flow curves

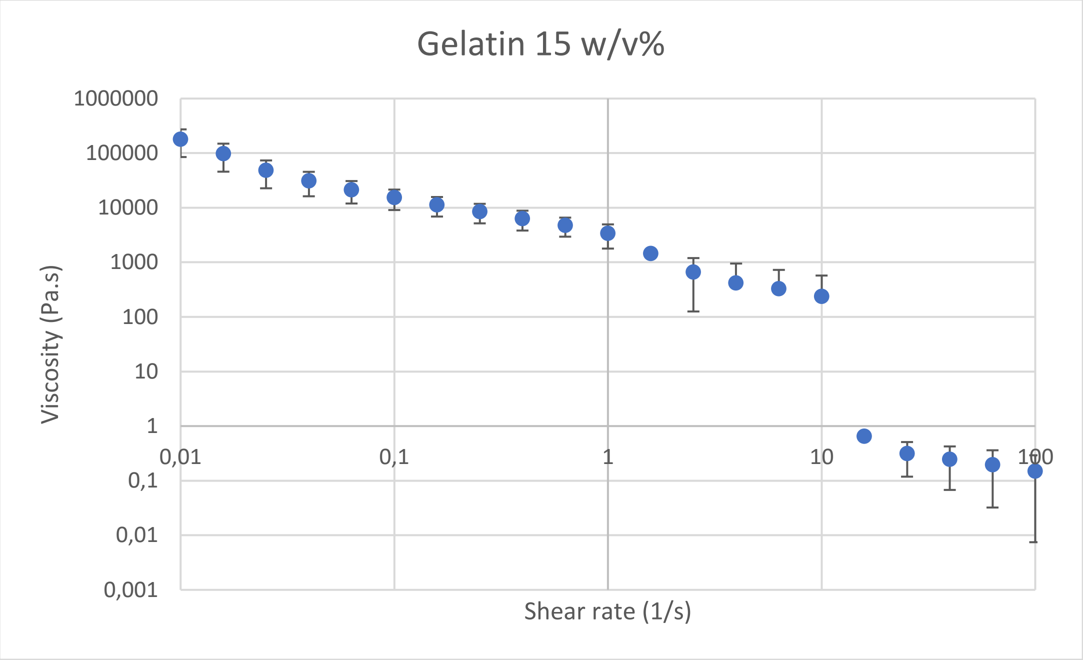

Figure 6.7-25 viscosity as a function of shear rate 15 w/v% gelatin (two runs)

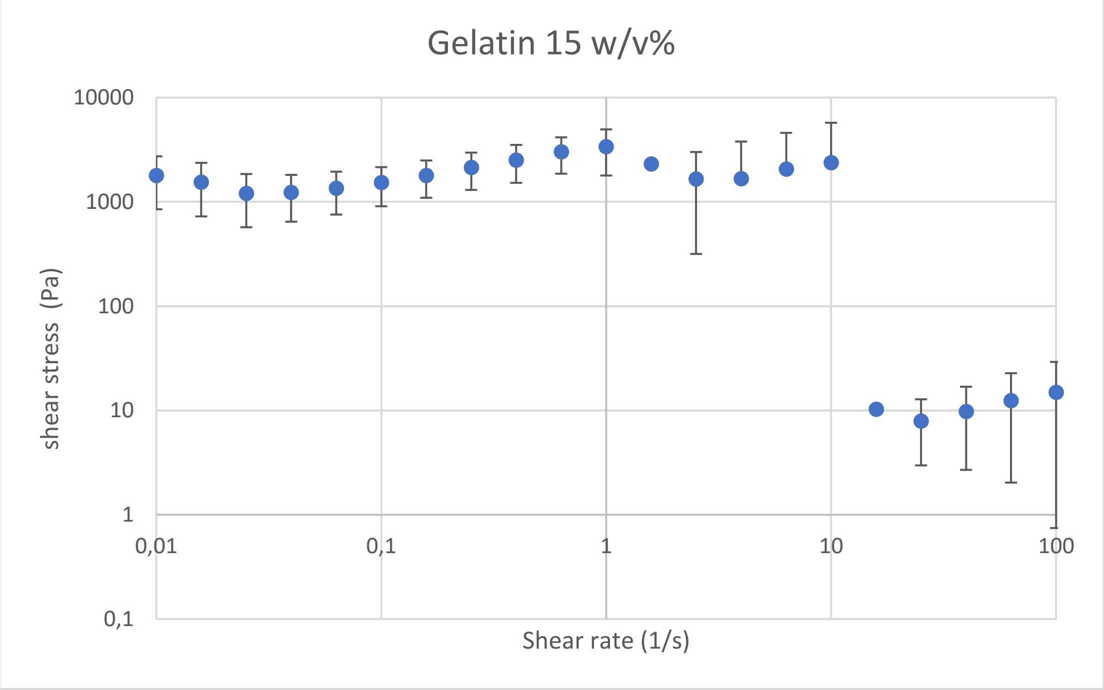

Figure 6.7-26 shear stress as a function of shear rate 15 w/v% gelatin (two runs)

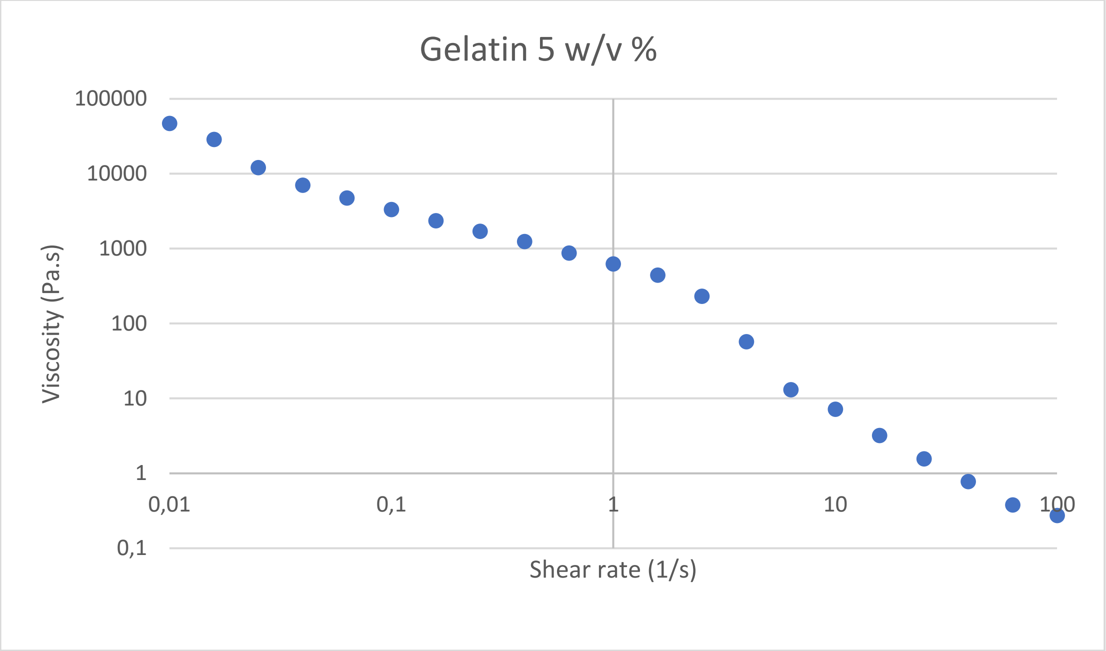

Figure 6.7-27 Figure 6.7-28 viscosity as a function of shear rate 5 w/v% gelatin (one run)

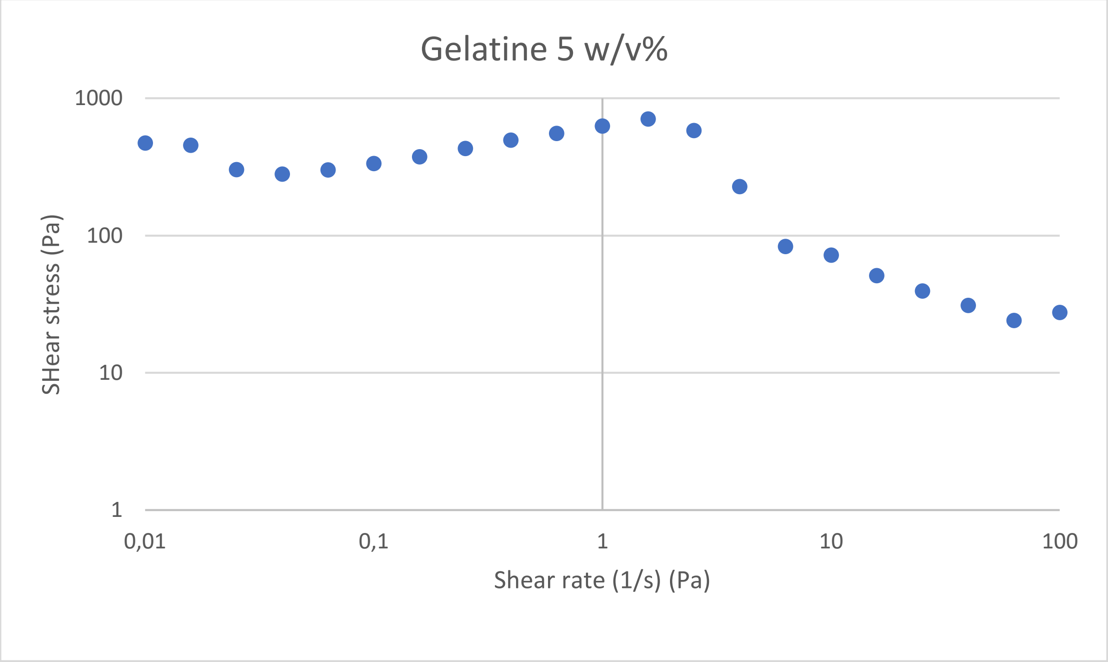

Figure 6.7-29 shear stress as a function shear rate 5 w/v% gelatin (one run)

B.6.2 Frequency sweep tests

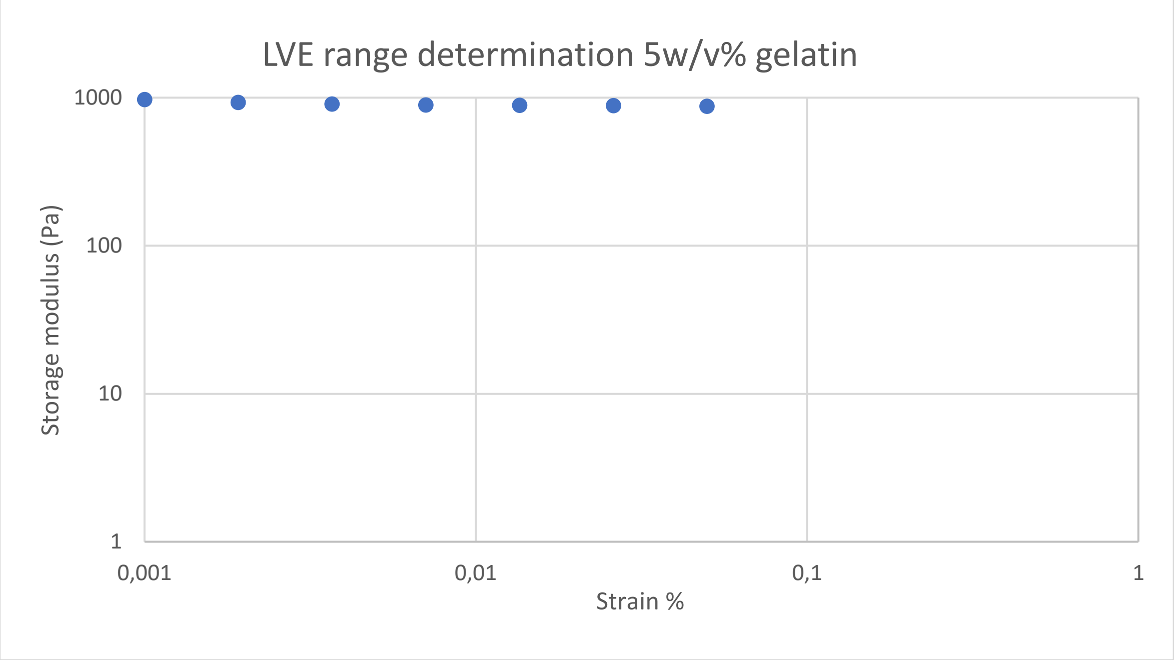

Figure 6.7-30 LVE 5 w/v% gelatin (one run)

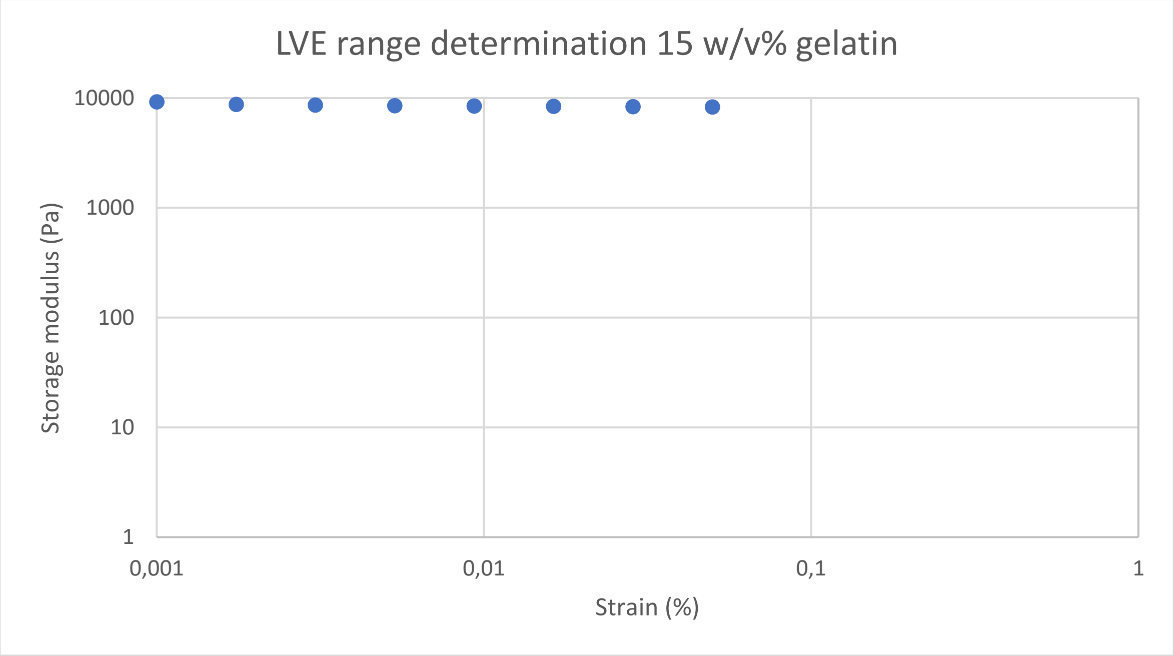

Figure 6.7-31 LVE 15 w/v% gelatin (one run)

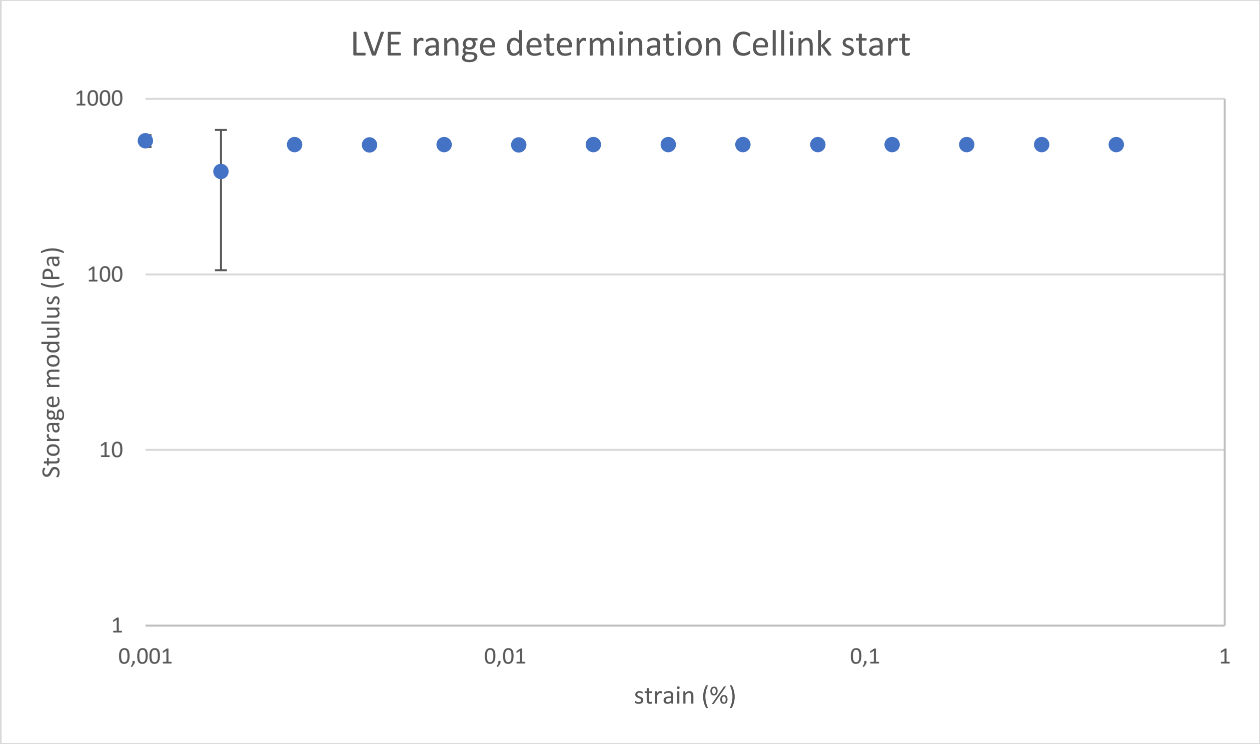

Figure 6.7-32 LVE ***Cellink start*** **(two runs)**

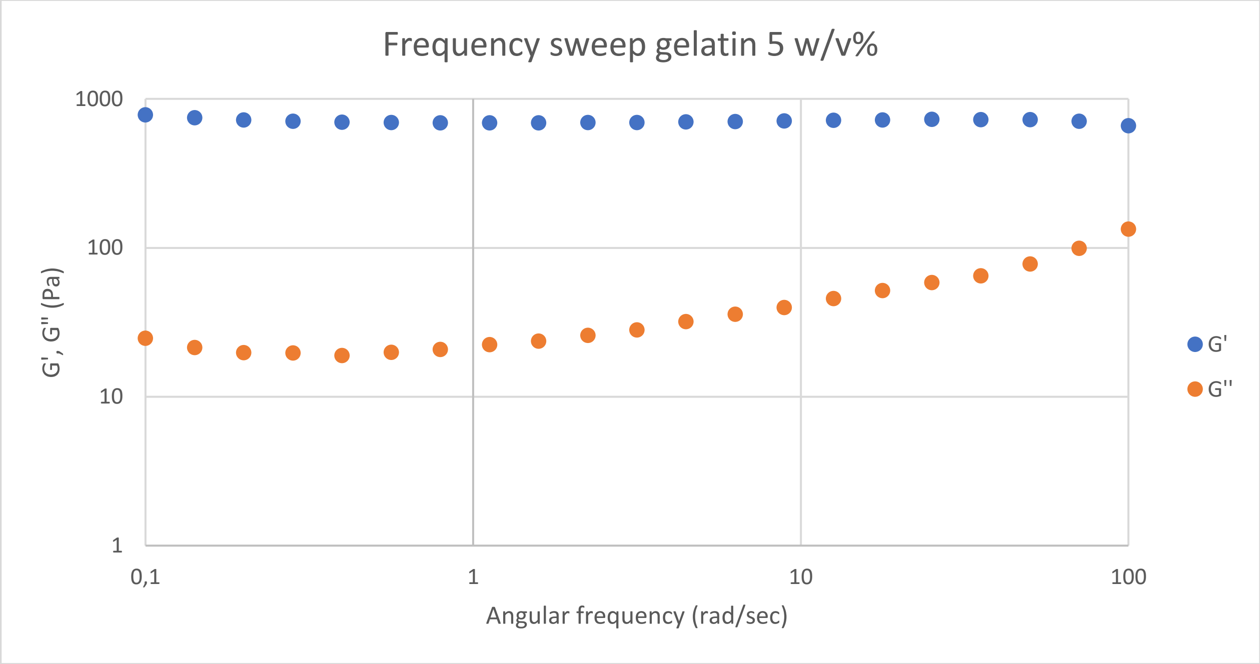

Figure 6.7-33 G’, G” as a function of the angular frequency 5 w/v% gelatin (one run)

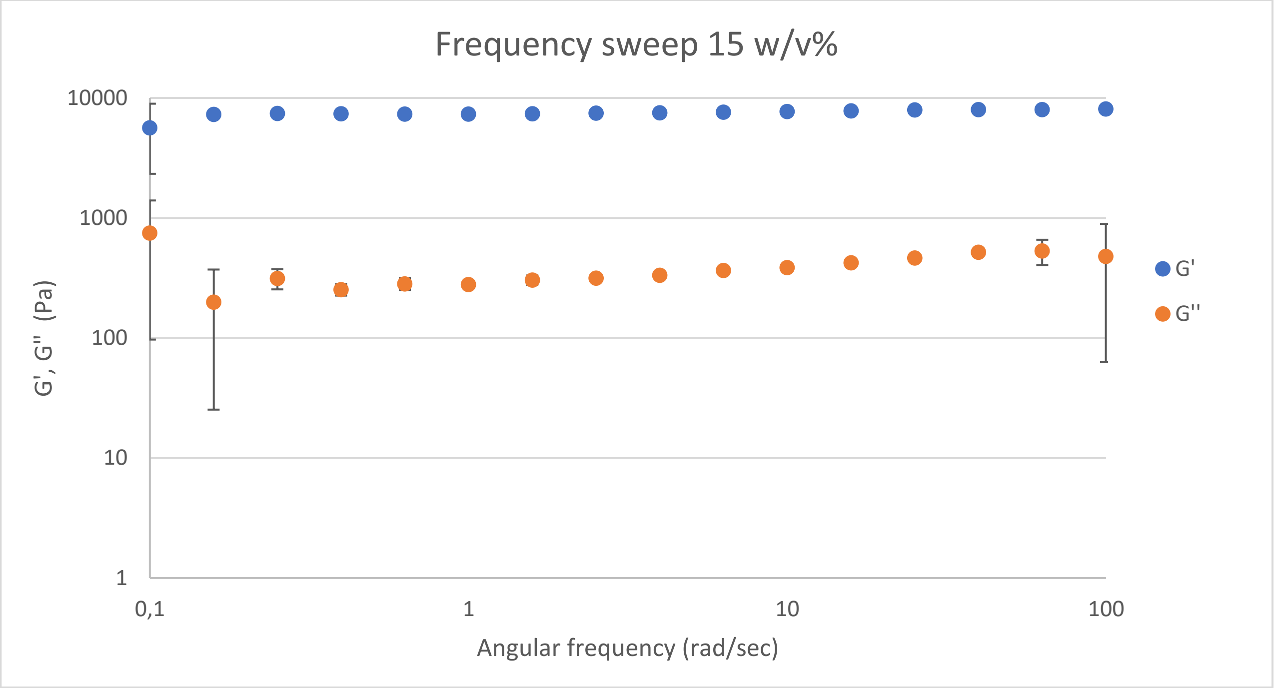

Figure 6.7-34 G', G" as a function of the angular frequency 5 w/v% gelatin (three runs)

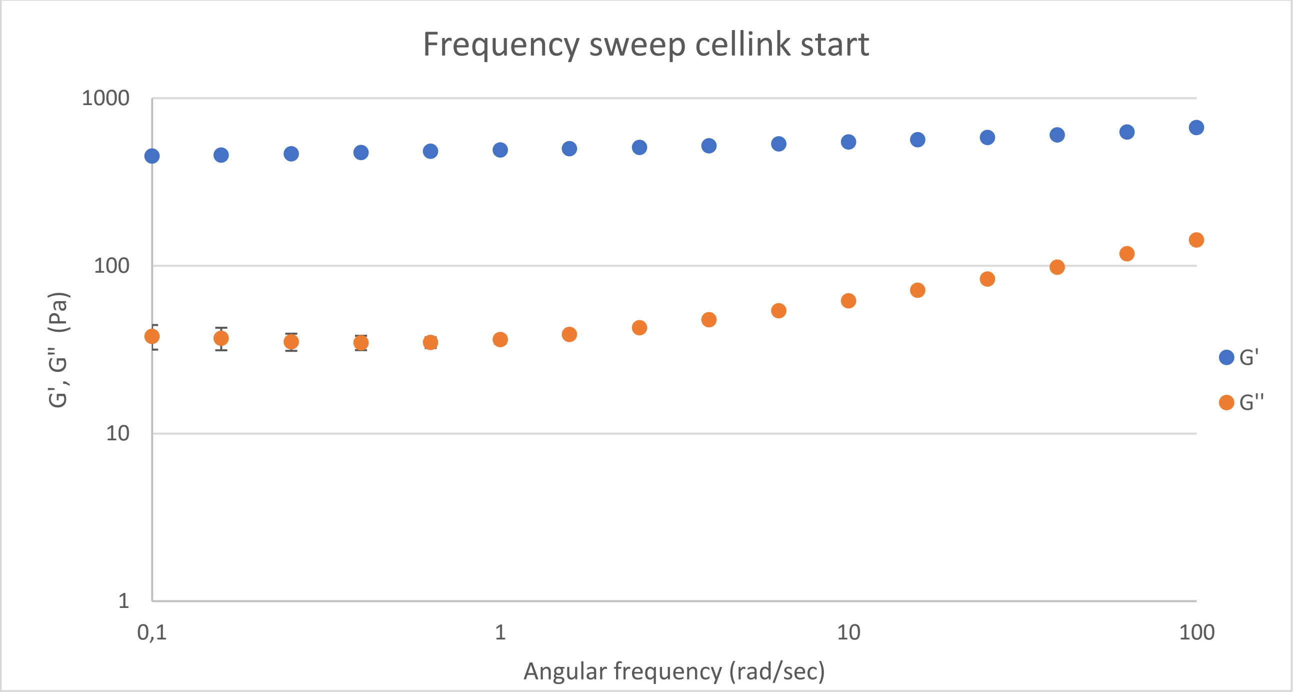

Figure 7- G', G" as a function of the angular frequency *Cellink start* (three runs)

Appendix C PROCESS ANALYZING AND DEVELOPMENT

C.1 Comparing cellink and B.Braun syringes: measured line width

B. Braun	60 kPa						
	Sample 1			Sample 2			average (mm)
feedrate (mm/s)	track 1	track 2	track 3	track 1	track 2	track 3	
10	676.06	800.31	812.95	669.74	893	899.31	0.81
	751.95	821.44	798.25	762.41	899.3	882.46	
	766.64	817.2	846.71	796.12	884.6	882.47	
15	604.46	642.39	648.69	631.83	659.2	661.36	0.65
	629.75	673.95	657.18	640.25	657.1	659.21	
	644.55	655.05	657.15	633.96	661.31	646.57	
20	562.34	591.81	583.45	534.95	583.42	564.49	0.57
	574.96	589.84	621.35	532.86	570.78	547.62	
	566.54	589.74	589.72	528.63	560.25	547.62	

Cellink	60 kPa			
		Sample 1		Average (mm)
feedrate (mm/s)	track 1	track 2	track 3	
10	1878.66	1777.64	1834.43	1.78
	1876.54	1714.35	1813.75	
	1731.28	1607.03	1769.12	
15	1600.63	1762.8	1663.81	1.65
	1617.61	1741.73	1596.41	
	1573.24	1686.98	1587.99	
20	1345.79	1316.3	1192.05	1.3
	1322.66	1345.81	1276.33	
	1272.19	1309.98	1341.6	

C.2 Design and manufacturing cooling system

C.2.1 Thermal calculations Peltier element

Properties aluminum plate

Dimensions plate:	8 cm x 8 cm x 0.3 cm
Density:	$\rho = 2712$ kg/m^3
Volume:	V = 0,0000192 m^3

Specific heat capacity:	C_P = 0,91 kJ/(kg*K)
Thermal conductivity of pure aluminum:	k = 204 W/mK (pure aluminum)

C.2.2 Transient analyses [62]

Assuming the temperature of the surrounding is 25°C and the temperature at the cold side of the Peltier element 10°C, makes for a temperature difference of 15°C. 25 °C is taken as a safety margin, in reality the element is expected to cool from room temperature (21 °C)

Starting from an aluminum plate at 25 °C an analyses must be made to estimate the heat that needs to be dissipated from the plate, Q_C (W). The plate can be perceived as a lump object, this means that the temperature distribution is theoretically uniform, so the temperature is a function of the time only. For this to be valid, the Biot number (Bi) has to be under (or equal to) 0.1, this number is the ratio of heat conduction to the heat convection. the Biot number is defined as followed:

$$L_c = \frac{V}{A_s} = \frac{\text{Volume}}{\text{convection surface}} = \frac{0.0000192\ \text{m3}}{0.0064\text{m2}} = 0.003\ \text{m}$$

$$B_i = \frac{L_C h}{k}$$

With:

k : thermal conductivity 204 W/(m*K)

h : convection coefficient (W/m^{2}K)

The convection coefficient is calculated as followed.

Table 6.7-2 Thermal properties of air at 20°C [63]

Density ρ (kg/m^3)	Specific heat c_p (KJ/kgK)	Thermal Conductivity k (W/(mK)	Kinematic viscosity v.10-^{6} (m^2/s)	Expansion Coefficient b .10^{-3}	Prandtl's Number Pr
1.205	1.005	0.0257	15.11	3.43	0.713

Characteristic length:

$$L = \frac{A}{P} = \frac{0.0064\ \text{m2}}{0.32\text{m}} = 0.02\ \text{m}$$

With: A: the area of the aluminum plate (m^2)

P: the perimeter of the aluminum plate (m)

Grashof number:

$$Gr = \frac{L^3 gb(T_W - T_\infty)}{v^2} = 14148$$

With: Gr: Grashof number

g: gravitational force (9,81 m.s^2)

L: characteristic lengt (0.02 m)

b: expansion coefficient (3.43*10^{-3})

v: kinematic viscosity (15.11*10^{-6} m^2/s)

T_w : surface temperature (°C)

T_∞ : bulk temperature (°C)

Rayleigh number:

Ra = Gr . Pr = 10088

With: Ra: Rayleigh number

Pr: Prandtl number

Upper surface of heated plate or lower surface of cooled plate:

$$\overline{\mathrm{Nu}} = 0.54 \cdot R_a^{1/4} = 5.4$$

With: Nu: Nusselt number

$$\overline{N_U} = \frac{\bar{h} \cdot L}{k}$$

The convection coefficient, h, can be calculated from this formula and is 7 W/m^{2}K.

The biot number is now as followed.

$$B_i = \frac{L_C h}{k} = \frac{= 0.003\ \mathrm{m}*7\ (\mathrm{W/m2K})}{204\ \mathrm{W/(m*K)}} = 0.00010$$

The number is small enough thanks to the small dimensions and the thermal conductivity of aluminum.

The heat transfer from the body (cooling) during an amount of time Δt is equal to the energy decrease inside the body during that amount of time.

$$Q * \Delta t = \rho * V * c_P.\ \Delta T$$

With: $Q.\Delta t$ is the heat transfer during a time of Δt (J)

$\rho \cdot V \cdot c_P$ is the thermal mass of the plate, the joules required to increase (or decrease in this case) the temperature of the object by 1°C.

Thus:

$$Q * \Delta t = 2712\ \mathrm{kg/m^3} * 0{,}0000192\ \mathrm{m^3} * 0{,}91.10^3\ \mathrm{J/kgK} * 15\ \mathrm{K} = 710{,}76\ \mathrm{J}$$

$$\rightarrow Q = 710{,}76\ \mathrm{J} / \Delta t$$

Depending on how fast you want the aluminum plate to reach 10°C, the heat that needs to be pumped will differ (Q), some examples:

5min: $Q =$ 710,76 J /300s = 2,4 W

2min: $Q =$ 710,76 J /120s = 5.9 W

1min: $Q =$ 710,76 J /60s = 11.8 W

Throughout the cooling process of the plate, convection does take place. The convection is going to be at its maximum point when the plate is at 10°C ($\Delta T = 15\ °C$). The heat transfer by convection formula:

$$Q_{\text{Convection}} = h * A * \Delta T$$

The convection coefficient was 7 W/m^{2}K as calculated, the affected surface is 0,0064 m^2.

$Q_{Convection}$ = 7 W/m^{2}K. 0,0064m^2 . 15 K = 0,67 W

This gives a Q_{total} with an extra **safety margin of 20%** added of:

5min: Q_{total} = 3,7 W

2min: Q_{total} = 7.9 W

1min: Q_{total} = 14,9 W

Q_{total} is the heat that needs to be pumped by the Peltier element, it is the value found in the data sheets.

C.2.3 List electric components

- NPN Darlington transistor	TIP142
- 560Ω resistor	MRS25 560R
- 0.22 Ω resistor	AC05 0R22
- NPN bipolar transistor	BC547C
- Components heatsink for Darlington transistor:	IM-56378 HS SK409/50STS M3*10 PAN ZN M3 NUT ZN IM-IB6

C.2.4 Arduino program cooling system

```
#include <PID_v1.h>

double temp, output;

#define temp_pin 5

#define output_pin 9

double setpoint = 12;
```

```
#include <LiquidCrystal.h>
LiquidCrystal lcd(12,11,5,4,3,2);
int val;

PID myPID(&temp,&output,&setpoint,440,0,0, REVERSE);

void setup() {
  // put your setup code here, to run once:
  Serial.begin (9600);
  myPID.SetMode(AUTOMATIC);
  myPID.SetOutputLimits(0, 200);
   lcd.begin (16,2);

}

void loop() {
  // put your main code here, to run repeatedly:
  temp  = (5.0 * analogRead(temp_pin)*100.0)/1024.0;
  Serial.println (temp,DEC);
  myPID.Compute(); //call every loop, updates automatically at certain time interval
  analogWrite(output_pin, output);
  Serial.println(output);
  //delay (100);

  val = analogRead(temp_pin);
  float mv = (val/1024.0)*5000;
  float cel = (5.0 * val *100.0)/1024.0;

  lcd.print("TEMPERATURE IS ");
  lcd.setCursor(0, 1);
  lcd.print(cel);
  lcd.setCursor(5, 1);
```

```
  lcd.print(" CELCIUS");
  delay (1000);
  lcd.clear();

}
```

C.3 Peltier element CP30238 specifications

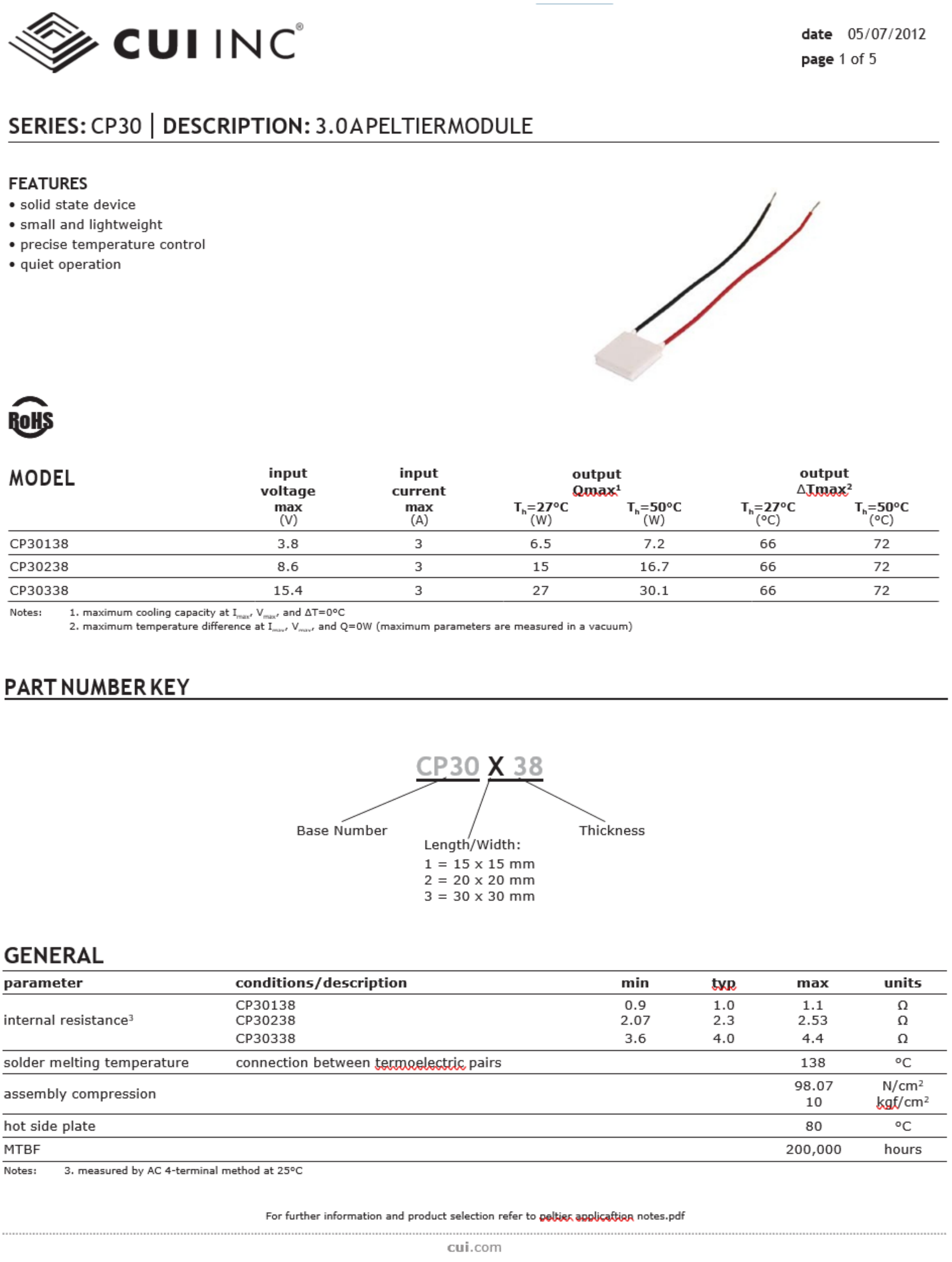

CUI INC

date 05/07/2012
page 1 of 5

SERIES: CP30 | DESCRIPTION: 3.0 A PELTIER MODULE

FEATURES

- solid state device
- small and lightweight
- precise temperature control
- quiet operation

RoHS

MODEL	input voltage max (V)	input current max (A)	output Qmax[1] T_h=27°C (W)	output Qmax[1] T_h=50°C (W)	output ΔTmax[2] T_h=27°C (°C)	output ΔTmax[2] T_h=50°C (°C)
CP30138	3.8	3	6.5	7.2	66	72
CP30238	8.6	3	15	16.7	66	72
CP30338	15.4	3	27	30.1	66	72

Notes: 1. maximum cooling capacity at I_{max}, V_{max}, and ΔT=0°C
2. maximum temperature difference at I_{max}, V_{max}, and Q=0W (maximum parameters are measured in a vacuum)

PART NUMBER KEY

CP30 X 38

Base Number

Length/Width:
1 = 15 x 15 mm
2 = 20 x 20 mm
3 = 30 x 30 mm

Thickness

GENERAL

parameter	conditions/description	min	typ	max	units
internal resistance[3]	CP30138 CP30238 CP30338	0.9 2.07 3.6	1.0 2.3 4.0	1.1 2.53 4.4	Ω Ω Ω
solder melting temperature	connection between termoelectric pairs			138	°C
assembly compression				98.07 10	N/cm² kgf/cm²
hot side plate				80	°C
MTBF				200,000	hours

Notes: 3. measured by AC 4-terminal method at 25°C

For further information and product selection refer to peltier applicaftion notes.pdf

cui.com

CP30238 PERFORMANCE (Th=50°C)

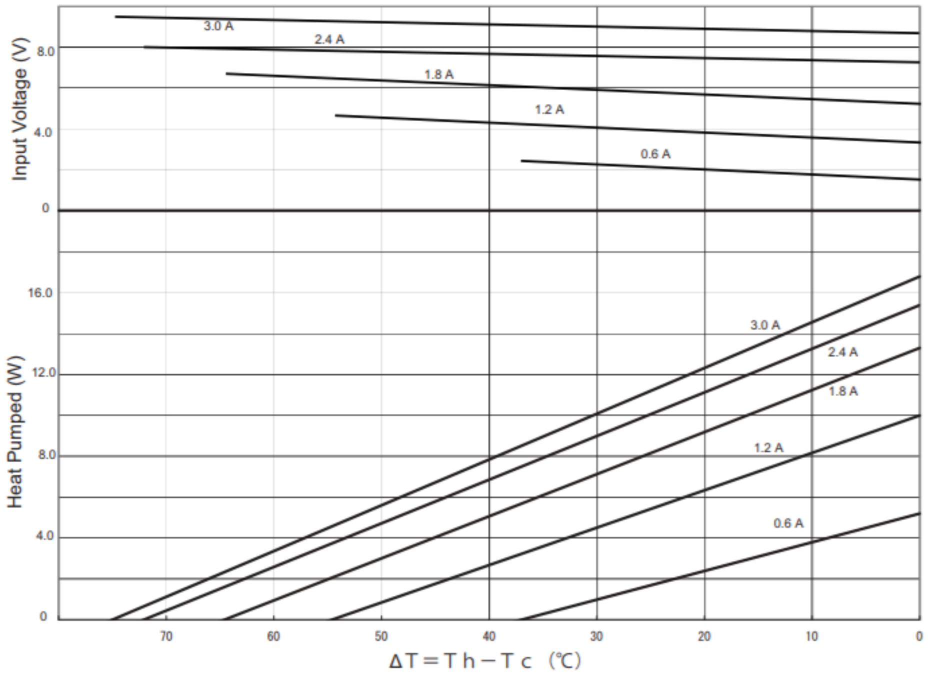

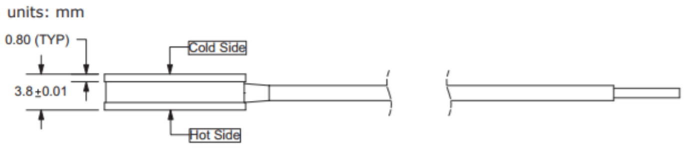

	MATERIAL	PLATING
ceramic plate	Al_2O_3 (Alumina)	
sealer	silicon rubber RTV	
lead wire	UL1430 (22AWG)	tin
joint cover	silicon rubber RTV	

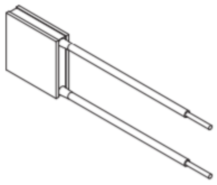

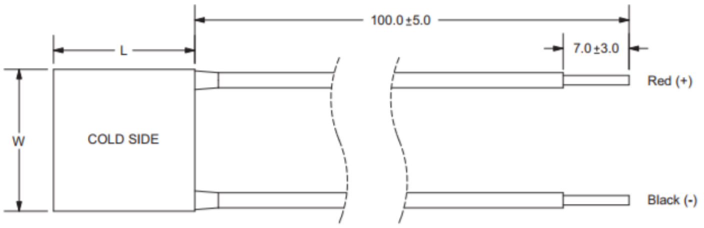

MODEL	LENGTH x WIDTH (mm)
CP30138	15 x 15 ±0.3
CP30238	20 x 20 ±0.3
CP30338	30 x 30 ±0.3

C.4 technical drawing case cooling system

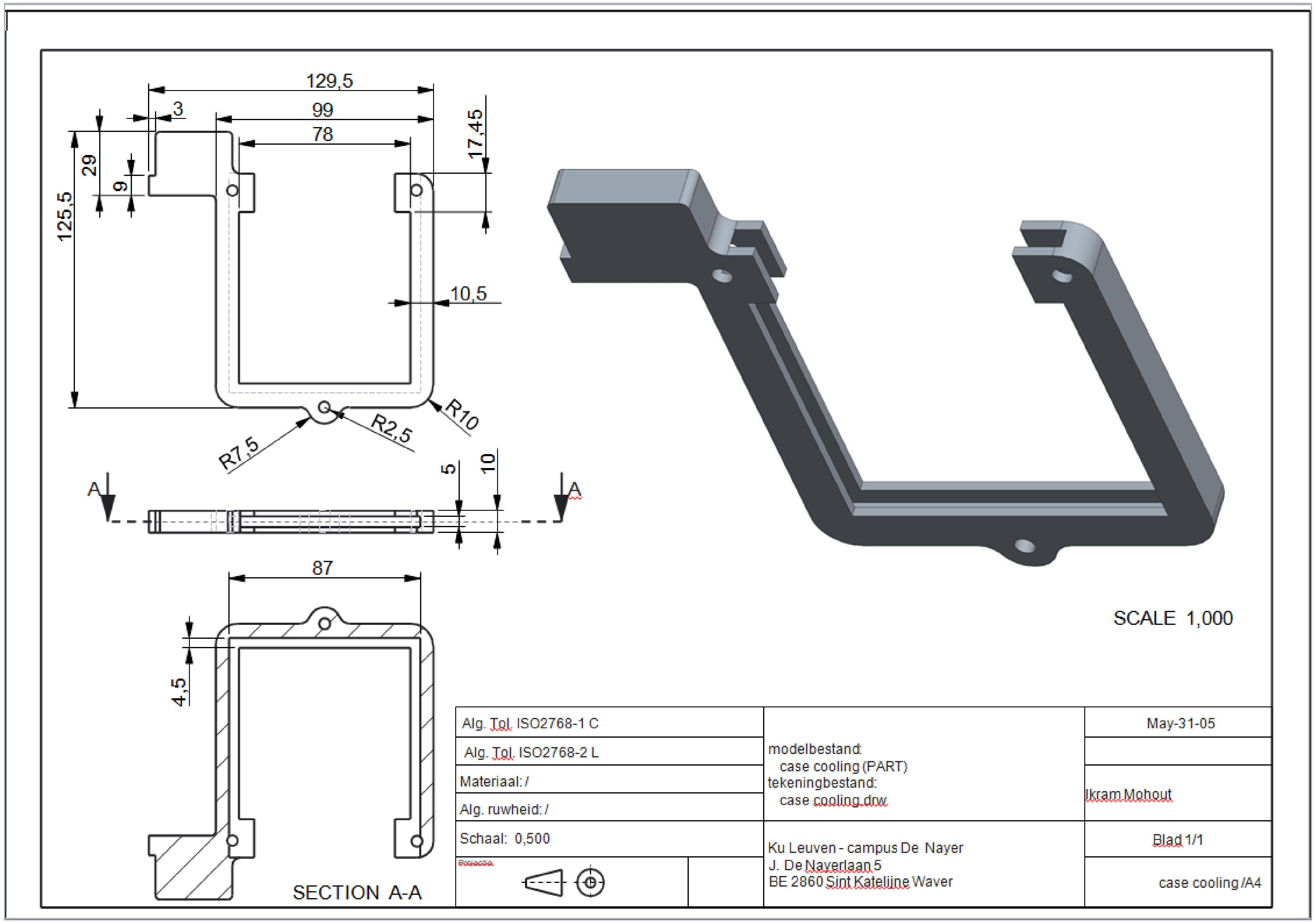

Alg. Tol. ISO2768-1 C	modelbestand: case cooling (PART) tekeningbestand: case cooling.drw	May-31-05
Alg. Tol. ISO2768-2 L		
Materiaal: /		Ikram Mohout
Alg. ruwheid: /		
Schaal: 0,500	Ku Leuven - campus De Nayer J. De Nayerlaan 5 BE 2860 Sint Katelijne Waver	Blad 1/1
Projectie		case cooling /A4

Appendix D MATERIAL PRINTING EXPERIMENTS

D.1 G-codes for printing

D.1.1 G-code: printing three tracks

```
M753 ; kop naar boven
M107
M751
G1 Z5 F5000 ; lift nozzle

; Filament gcode


G21 ; set units to millimeters
G90 ; use absolute coordinates
M82 ; use absolute distances for extrusion
;G92 E0
G1 Z0.400 F7800.000
G1 E-2.00000 F2400.00000
;G92 E0
G1 X0 Y0 F7800.000
G1 E2.00000 F2400.00000
M760
G1 F600 ; mm/min

G1 X0. Y20 E2.41108
G1 X5. Y20. E2.51027
G1 X5. Y0. E2.92135
G1 X10. Y0. E3.02054
G1 X10. Y20. E3.43161
M761
G1 X20. Y0. F2400
```

```
M760
G1 F600 ; mm/min

G1 X20. Y20. E2.41108
G1 X25. Y20. E2.51027
G1 X25. Y0. E2.92135
G1 X30. Y0. E3.02054
G1 X30. Y20. E3.43161
M761
G1 X40. Y0 F2400
M760
G1 F600 ; mm/min

G1 X40. Y20. E2.41108
G1 X45. Y20. E2.51027
G1 X45. Y0. E2.92135
G1 X50. Y0. E3.02054
G1 X50. Y20. E3.43161
M761
G1 Z0.800 F7800.000

G1 E0.97378 F2400.00000
G92 E0
M753 ; printkop naar boven
M107
; Filament-specific end gcode
;END gcode for filament

M104 S0 ; turn off temperature
G28 X0  ; home X axis
M84     ; disable motors
```

D.1.2 G-code: printing one track

```
M753 ; kop naar boven
```

```
G1 Z5 F5000 ; lift nozzle
M104 s30

; Filament gcode


G21 ; set units to millimeters
G90 ; use absolute coordinates
M82 ; use absolute distances for extrusion
;G92 E0
G1 Z0.400 F7800.000
G1 E-2.00000 F2400.00000
;G92 E0
G1 X0 Y0 F7800.000
G1 E2.00000 F1200.00000
M760
G1 F2400 ;snelheid mm/min

G1 X0. y0. E2.41108
G1 x20. y0.
G1 X20. Y20. E2.51027
G1 X25. Y20. E2.92135
G1 X25. Y0. E3.02054
G1 X30. Y0. E3.43161
G1 x30. y20.
M761 ;druk af
G1 X40. Y20. F2400

G1 Z0.800 F7800.000
```

```
G1 E0.97378 F2400.00000
G92 E0
M753 ; printkop naar boven

M104 s30
```

D.1.3 G-code: lattice structure 40% infill

```
753 ; kop naar boven
M107
M751

G1 Z5 F5000 ; lift nozzle

; Filament gcode

G21 ; set units to millimeters
G90 ; use absolute coordinates
M82 ; use absolute distances for extrusion
G92 E0
M760
G1 Z0.250 F7800.000
G1 E-2.00000 F2400.00000
G92 E0
G1 X2.190 Y0.528 F7800.000
G1 E2.00000 F2400.00000
G1 F900
G1 X2.190 Y20.420 E2.31402
G1 X4.153 Y20.420 E2.34502
G1 X4.153 Y0.528 E2.65904
G1 X6.117 Y0.528 E2.69004
G1 X6.117 Y20.420 E3.00407
G1 X8.080 Y20.420 E3.03506
```

```
G1 X8.080 Y0.528 E3.34909
G1 X10.044 Y0.528 E3.38008
G1 X10.044 Y20.420 E3.69411
G1 X12.007 Y20.420 E3.72510
G1 X12.007 Y0.528 E4.03913
G1 X13.971 Y0.528 E4.07012
G1 X13.971 Y20.420 E4.38415
G1 X15.934 Y20.420 E4.41514
G1 X15.934 Y0.528 E4.72917
G1 X17.898 Y0.528 E4.76016
G1 X17.898 Y20.420 E5.07419
G1 Z0.500 F7800.000
G1 E3.07419 F2400.00000
G92 E0
G1 X20.083 Y2.620 F7800.000
G1 E2.00000 F2400.00000
G1 F900
G1 X0.004 Y2.620 E2.55774
G1 X0.004 Y4.584 E2.61228
G1 X20.083 Y4.584 E3.17002
G1 X20.083 Y6.547 E3.22456
G1 X0.004 Y6.547 E3.78230
G1 X0.004 Y8.511 E3.83684
G1 X20.083 Y8.511 E4.39458
G1 X20.083 Y10.474 E4.44912
G1 X0.004 Y10.474 E5.00685
G1 X0.004 Y12.438 E5.06140
G1 X20.083 Y12.438 E5.61913
G1 X20.083 Y14.401 E5.67368
G1 X0.004 Y14.401 E6.23141
G1 X0.004 Y16.365 E6.28595
G1 X20.083 Y16.365 E6.84369
```

```
G1 X20.083 Y18.328 E6.89823
G1 X0.004 Y18.328 E7.45597
M761
G1 E2.10955 F2400.00000
G92 E0
M753
M107

; Filament-specific end gcode
;END gcode for filament



G28 X0  ; home X axis
M84     ; disable motors
```

D.2 Cellink start

D.2.1 DOE

D.2.1.1 25 G conical nozzle

		Printing pressure							
		60 kPa				80 kPa			
		Sample 1 (µm)			average	Sample 1 (µm)			average
feed rate (A)	Measurements	track 1	track 2	track 3		track 1	track 2	track 3	
10 mm/s	measurement 1	676,06	800	813		1489	1323	1577	
	measurement 2	751,95	821	798		1489	1379	1571	
	measurement 3	766,64	817	847	0.79	1478	1398	1609	1.48
15 mm/s	measurement 1	604,46	642	649		1259	1222	1226	
	measurement 2	629,75	674	657		1358	1255	1201	

	measurement 3	644,55	655	657	0.64	1344	1257	1238	1.26
20 mm/s	measurement 1	562,34	592	583		801	975	922	
	measurement 2	574,96	590	621		1024	1017	969	
	measurement 3	566,54	590	590	0.59	1025	1011	1018	0.97

		Sample 2	(µm)			Sample 2 (µm)			
feed rate (A)	measuremente n	track 1	track 2	track 3		track 1	track 2	track 3	
10 mm/s	measurement 1	670	893	899		1754	1552	1544	
	measurement 2	762	899	882		1771	1567	1556	
	measurement 3	796	885	882	0.84	1746	1596	1559	1.63
15 mm/s	measurement 1	632	659	661		1217	1365	1346	
	measurement 2	640	657	659		1278	1319	1314	
	measurement 3	634	661	647	0.65	1281	1329	1207	1.30
20 mm/s	measurement 1	535	583	564		952	1070	1068	
	measurement 2	533	571	548		1070	1104	1072	
	measurement 3	529	560	548	0.55	1062	1070	1087	1.08

80 kPa (+)

		Sample 1	(µm)		Sample 2	(µm)		average
feed rate	measuremente n	track 1	track 2	track 3	track 1	track 2	track 3	
10 mm/s	measurement 1	1489	1323	1577	1754	1552	1544	1.55
	measurement 2	1489	1379	1571	1771	1567	1556	
	measurement 3	1478	1398	1609	1746	1596	1559	
15 mm/s	measurement 1	1259	1222	1226	1217	1365	1346	1.28
	measurement2	1358	1255	1201	1278	1319	1314	
	measurement3	1344	1257	1238	1281	1329	1207	
20 mm/s	measurement 1	801	975	922	952	1070	1068	1.02

measurement 2	1024	1017	969	1070	1104	1072
measurement 3	1025	1011	1018	1062	1070	1087

D.2.1.2 *20 G blunt nozzle*

	pressure (kPa)	feed rate (mm/s)	measurement 1	measurement 2	measurement 3	average respons (mm)
Replica 1	90	5	2159	2060	2048	2.09
Replica 2			2184	1999	1999	2.06
Replica 3			2201	2121	2129	2.15
Replica 1	90	10	1756	1660	1769	1.73
Replica 2			1756	1611	1735	1.70
Replica 3			1771	1685	1704	1.72
Replica 1	90	15	1569	1579	1459	1.54
Replica 2			1531	1536	1447	1.50
Replica 3			1599	1512	1567	1.56
Replica 1	110	5	2380	2508	2571	2.49
Replica 2			2703	2604	2626	2.64
Replica 3			2704	2592	2907	2.73
Replica 1	110	10	2117	2056	2064	2.08
Replica 2			2222	2121	2077	2.14
Replica 3			2201	2218	2104	2.17
Replica 1	110	15	1938	1763	1858	1.85
Replica 2			1948	1881	1845	1.89
Replica 3			1973	1866	1834	1.89

D.2.2 Results DOE ANOVA

D.2.2.1 25G conical nozzle

Design Summary

Factors:	2	Replicates:	2
Base runs:	6	Total runs:	12
Base blocks:	1	Total blocks:	1

Number of levels: 2; 3

Factor Information

Factor	Levels	Values
Pressure (kPa)	2	60; 80
Feed rate (mm/s)	3	10; 15; 20

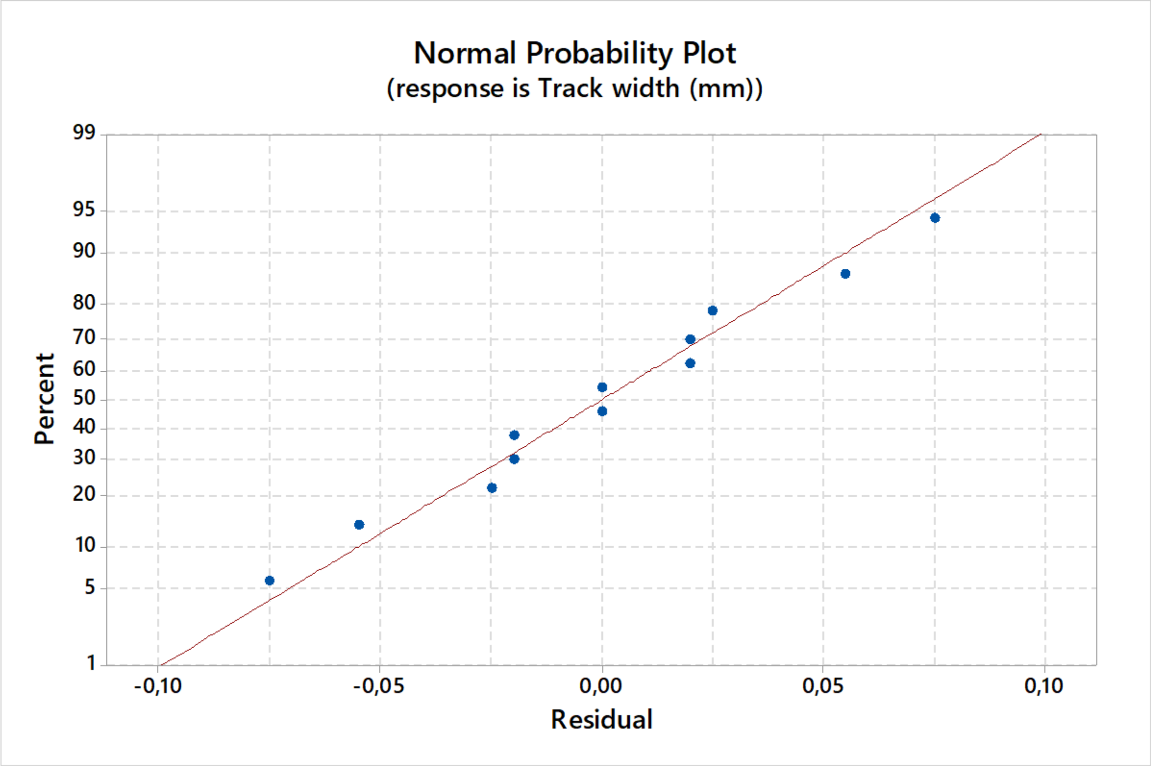

D.2.2.2 20G blunt nozzle

Design Summary

Factors:	2	Replicates:	3
Base runs:	6	Total runs:	18

Base blocks: 1 Total blocks: 1

Number of levels: 2; 3

Factor Information

Factor	Levels	Values
Pressure (kPa)	2	90; 110
Feed rate (mm/s)	3	5; 10; 15

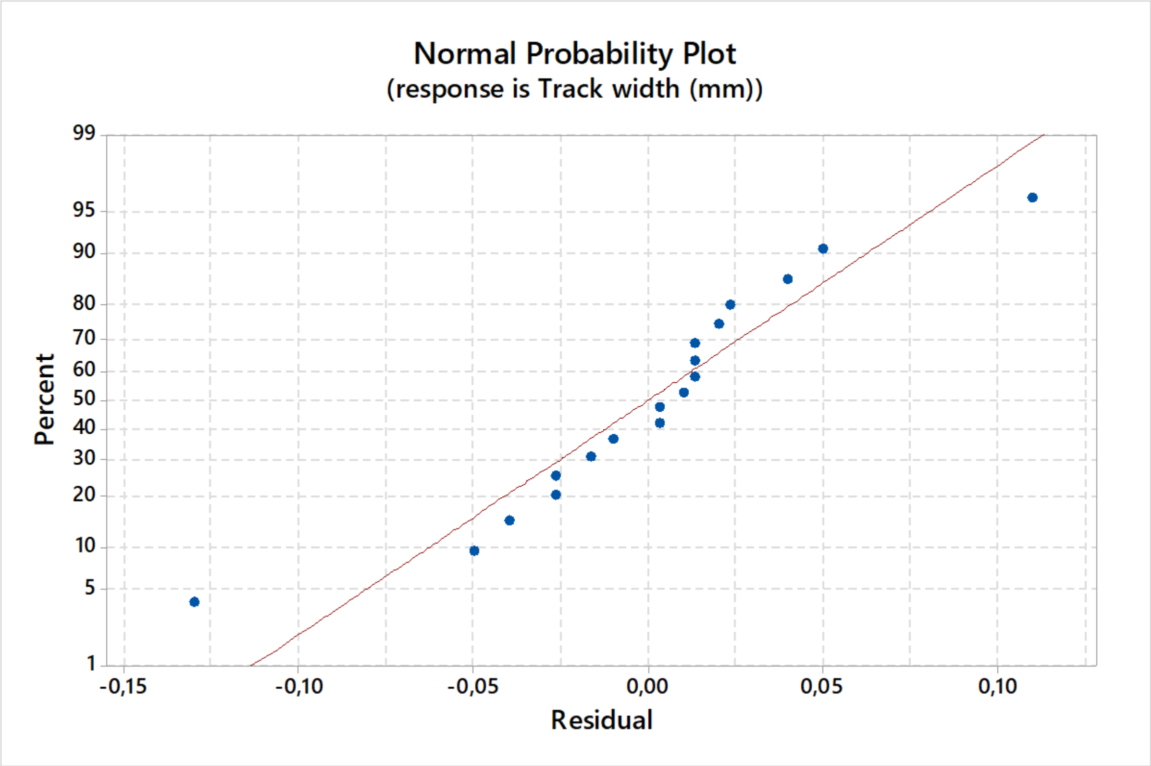

D.2.3 Data lattice structures

20G blunt nozzle

	Theoretical			experimental						
Infill (%)	D (mm)	W (mm)	Ath (mm2)	Height cavity (mm)	width cavity (mm)	Ae (mm2)	average Art (mm2)	Diffusion rate (%)	deviation (mm2)	deviation (%)
0.2	3.93	0.61	11.0224	2.76026	2.9973	8.27322	8.40943816	23.706	0.138502	2%
				2.85826	2.9914	8.55011				
				2.81043	2.9906	8.40498				

0.4	1.96	0.61	1.8225	0.64628	0.4697	0.30356	0.315204589	82.705	0.049564	3%
				0.44238	0.616	0.2725				
				0.53286	0.6935	0.36955				

25 G conical nozzle

			Theoretical			experimental				
Infill (%)	D (mm)	W (mm)	Ath (mm2)	Height cavity (mm)	width cavity (mm)	Ae (mm2)	average Art (mm2)	Diffusion rate (%)	deviation (mm2)	deviation (%)
20	3.927	0.25	13.52033	3.35	3.6	12.06	12.1	11		
40	1.963	0.25	2.934369	1.1	1	1.1	1.12	62	0.02887	1%
				1.15	1	1.15				
				1.1	1	1.1				
50	1.57	0.25	1.7424	0.9	0.7	0.63	0.7	60	0.06506	4%
				0.95	0.8	0.76				
				1	0.7	0.7				
60	1.309	0.25	1.121481	0.7	0.5	0.35	0.34	69	0.01702	1%
				0.65	0.5	0.325				
				0.65	0.55	0.3575				
70	1.122	0.25	0.760384	0.55	0.35	0.1925	0.19	76	0.05779	8%
				0.6	0.4	0.24				
				0.5	0.25	0.125				

D.3 Gelatin Data DOE

	Ambient temperature	Gelatin # days old	Pressure (kPa)	Printing speed (mm/s)	Nozzle	Measurement 1	Measurement 2	measurement 3	Average respnse (mm)
replica 1	25°C	4	50	20	25 G	758.2	783.51	821.55	0.79

replica 2	24°C	5				585.55	595.35	883.15	0.69
replica 3	22°C	10				2692.02	2323.66	2415.68	2.48
replica 1	25°C	4	70	20	25G	728.72	568.66	566.54	0.62
replica 2	24°C	5				1124.67	1021.45	1069.96	1.07
replica 3	29°C	3				4138.43	4200.37	3951.09	4.1
replica 1	25°C	4	90	20	25G	850.88	794.02	615.03	0.75
replica 2	24°C	5				2101.87	2017.63	1845.16	1.99
replica 3	22°C	10				2813.81	2834.79	3201.29	2.95
replica 1	25°C	4	50	40	25G	642.36	534.96	655.01	0.61
replica 2	24°C	5				608.66	663.43	747.77	0.67
replica 3	22°C	10				1065.68	1034.14	1076.24	1.06
replica 1	25°C	4	70	40	25G	753.98	779.3	930.91	0.82
replica 2	24°C	5				684.48	846.74	764.52	0.77
replica 3	22°C	10				1050.94	758.3	642.36	0.82
replica 1	25°C	4	90	40	25G	1029.88	1135.18	1063.57	1.08
replica 2	24°C	5				1421.63	1337.38	1415.3	1.39
replica 3	29°C	3				3066.56	3150.84	2906.5	3.04
replica 1	25°C	4	50	20	27G	2078.72	1821.77	1666.02	1.86
replica 2	24°C	5				1375.28	730.89	842.43	0.98
replica 3	22°C	10				1882.96	1691.32	1826.05	1.8
replica 1	25°C	4	70	20	27G	3205.64	1665.92	1771.22	2.21
replica 2	24°C	5				1649.07	1265.84	1147.82	1.35
replica 3	22°C	10				751.92	812.95	716.07	0.76
replica 1	25°C	4	90	20	27G	1809.13	1556.43	1903.96	1.76
replica 2	24°C	5				1655.39	1385.84	1505.18	1.52
replica 3	22°C	10				1609.12	3020.15	3597.21	2.74

replica 1	25°C	4	50	40	27 G	1623.79	1560.61	1326.83	1.5
replica 2	24°C	5				446.49	596.26	583.39	0.45
replica 3	22°C	10				505.46	436.04	636.16	0.536
replica 1	25°C	4	70	40	27 G	1588	1322.66	1337.36	1.42
replica 2	24°C	5				789.79	817.16	1105.7	0.904
replica 3	22°C	10				4374.97	3869.4	2413.09	3.55
replica 1	25°C	4	90	40	27 G	2175.81	1916.55	1906.12	2.0
replica 2	24°C	5				829.8	779.28	798.22	0.8
replica 3	22°C	10				4440.86	4139.97	4356.69	4.31

D.3.1 Results DOE ANOVE

Design summary

Factors:	3	Replicates:	3
Base runs:	12	Total runs:	36
Base blocks:	1	Total blocks:	1

Number of levels: 2; 3; 2

Factor information

Factor	Levels	Values
Nozzle (G)	2	25; 27
Pressure (kPa)	3	50; 70; 90
speed (mm/s)	2	20; 40

Analysis of variance

Source	DF	Adj SS	Adj MS	F-Value	P-Value
Model	4	15373521	3843380	2,02	0,116
Linear	4	15373521	3843380	2,02	0,116
Nozzle (G)	1	229441	229441	0,12	0,731
Pressure (kPa)	2	13712867	6856433	3,60	0,039
speed (mm/s)	1	1431213	1431213	0,75	0,393

Error	31	59061679	1905215		
Lack-of-Fit	7	3230788	461541	0,20	0,983
Pure Error	24	55830891	2326287		
Total	35	74435201			

Model summary

S	R-sq	R-sq(adj)	R-sq(pred)
1380,30	20,65%	10,42%	0,00%

FACULTY OF ENGINEERING TECHNOLOGY
DE NAYER (SINT-KATELIJNE-WAVER) CAMPUS
Jan De Nayerlaan 5
2860 SINT-KATELIJNE-WAVER, België
tel. + 32 16 30 10 30
fet.denayer@kuleuven.be
www.fet.kuleuven.be